THESIS FOR THE DEGREE OF DOCTOR OF PHILOSOPHY

Design and analysis of a fault-tolerant fractional slot PMSM for a vehicle application

CHRISTIAN DU-BAR

Division of Electric Power Engineering
Department of Energy and Environment
CHALMERS UNIVERSITY OF TECHNOLOGY
Göteborg, Sweden 2016

Design and analysis of a fault-tolerant fractional slot PMSM
for a vehicle application
CHRISTIAN DU-BAR
ISBN 978-91-7597-467-5

Doktorsavhandlingar vid Chalmers tekniska högskola
Ny serie nr 4148
ISSN 0346-718X

Department of Energy and Environment
Division of Electric Power Engineering
CHALMERS UNIVERSITY OF TECHNOLOGY
SE-412 96 Göteborg
Sweden
Telephone + 46 (0)31 772 00 00

Chalmers Bibliotek, Reproservice
Göteborg, Sweden 2016

Abstract

The permanent magnet synchronous motor (PMSM) is an interesting alternative for an electric motor drive system in automotive applications, due to to the high efficiency requirement; as only a limited amount of energy can be stored in the relatively expensive battery. Another advantage is the high torque and power density a PMSM can achieve since it is very important to save especially space but also weight in vehicle applications. As the battery technology develops, pure electric cars are expected to become a more and more interesting alternative. It is then natural that the requirement of reliability on the electric drive system becomes an aspect of utmost importance as the electric drive is the only driving force.

In this thesis, a fault-tolerant fractional slot PMSM is designed and its capability to operate even after a fault occurs is investigated. The faults investigated are phase open circuit and phase short circuit, and it is shown that the thesis machine design can be operated during both circumstances. The fault-tolerant thesis machine design is compared with two reference machines; one existing PMSM design of the same size and a smaller prototyped PMSM, also including measurements for the later. All three machines are evaluated both during normal and during phase open circuit operation, using a method where the remaining two phase currents are rearranged in order to get constant currents in the rotating dq reference frame. It is found that the maximum torque is reduced to approximately $1/\sqrt{3}\approx 58\%$ and the maximum speed to roughly $1/2$, in relation to what is achievable for each machine during normal operation. The thermal limits are investigated and shown to follow the electrical limits for the thesis design and for the prototyped IPM machine. However, when this method is used, it is noticed that the torque quality might be reduced significantly.

A semi-analytical machine modeling approach is introduced and used to model the individual saturation levels of the phases. The same model is used to calculate new current wave forms in order to reduce the torque ripple during the unbalanced conditions associated with the operation during fault. Consequently, for the thesis design with reduced torque ripple, the maximum torque is reduced to approximately 50 % and the maximum speed is reduced to roughly

1/3 or 1/4 of the maximum speed in case of a phase open circuit fault or a phase short circuit fault respectively.

Keywords

Permanent magnet synchronous machine (PMSM), Fractional slot, Concentrated windings, Fault-tolerance, Unbalanced operation, Saturation, Efficiency.

Acknowledgements

The financial support from the Swedish innovation agency Vinnova via the former xEVCO project including Volvo Cars and SP, which this PhD project was a part of, is gratefully appreciated.

I would like to thank my main supervisor and examiner Torbjörn Thiringer for his great support and always very quick response with input and feedback. I would of course also like to address special thanks to my supervisors Sonja Lundmark and Mikael Alatalo for their support and valuable input and comments.

I spent a lot of time with the experimental setup down in the lab, where I also got help and companionship. Special thanks to Johan Åström for collaboration around the experimental IPM machine. I would like to thank Andreas Nilsson at SP, who developed the measurement program on the lab-PC and also solved urgent problems remotely while he was out traveling.

I would also like to thank all my colleagues, room-mates and friends at the Division of Electric Power Engineering for creating such a nice and fun environment to work in. Thanks also to the people one stair down at the Division of High Voltage Engineering, they also contribute to the appreciated working environment.

Finally, I would like to thank my family including my wonderful fiancée Gabriela for endless love and support over the years.

Christian Du-Bar
Göteborg, Septermber 2016

Contents

Introduction

Background

Permanent magnet synchronous machines (PMSM) of different sizes are used in a great number of applications. They are often competitive in the low power region due to high efficiency, and in the medium power region due to high torque and power density. At higher power levels, PMSM are sometimes used as wind power generators, also offering the possibility to remove the gear box and operate in a direct-drive configuration. The PMSM are often categorized depending on the permanent magnet (PM) and rotor configuration as well as the flux path and air-gap arrangement. The PM can be surface-mounted or interior-mounted and the same stator can be used for both types of machines. Further, the PMSM can be divided into radial flux machines where the magnetic flux is crossing the air-gap in the radial direction and axial flux machines where the magnetic flux crosses the air-gap in the axial direction. Again, it is often possible to utilize the same pole, slot and winding configuration. A third group is the transverse flux machines, that benefit from the involvement of a more complicated magnetic circuit in favor of a simpler electrical circuit.

In automotive applications, the PMSM is an interesting alternative due to the high efficiency requirement; as only a limited amount of energy can be stored in the relatively expensive battery. Another advantage is the high torque and power density since it is very important to save especially space but also weight in vehicle applications. The introduction of electric drives into vehicles may improve the fuel economy and reduce the environmental emissions but allows also for new features such as increased safety and passenger comfort. The extensive research in fault-tolerant PMSMs, initially triggered by the safety-critical area of aerospace applications, has also gained a lot of interest within the automotive field [1]. Without continuous monitoring of the power train of an electric vehicle (EV), faults might cause permanent damage or even accidents, depending on the severity of a fault [2]. In addition to insure the immediate risks of hazards, such as disturbances of safety critical functions and vehicle stability, it is also desirable to have some post-fault capacity i.e. a "limping home" functionality [3]. It is natural that the requirement of reliability on the electric drive

system becomes an important aspect, especially in case of pure electric vehicles when the electric power train is the only driving source. According to [4], the trend towards autonomous control systems increases the interest of fault-tolerant capability in automotive applications. It is therefore of interest to combine the advantages of high efficiency, torque and power density associated with the PMSM and the ability of operation during isolated failures in the machine or the converter. In [5], it is stated that the introduction of fault-tolerance into the permanent magnet machine design is related with only a modest reduction of the torque capability.

Fault-tolerant electric machines

There are two possible meanings of fault-tolerant electric drive systems [6]:

- a system designed to reduce the number of fault occurrences.
- a system that is able to operate even after a fault occurs, on short-term or continuously.

  where the second group can be divided into two subgroups

  - a PM motor drive configuration with independent phases, that may operate independently. In case of a fault in one phase, the other phases can still be operated.
  - a redundant system, where the number of one or more components is extended. During healthy operation, the redundant components are totally or partially excluded.

From a practical point of view, it is not that straightforward to distinguish between a system or a machine that is designed to reduce the number of fault occurrences or is designed to be able to operate even after a fault occurs. In the case of a machine design with independent phases in order to better operate after a fault occurs, a low mutual coupling is suggested in [5] and [6]. However, the electrical insulation between phases may be increased as a consequence. An increased electrical phase separation is also mentioned in [6], both to limit the probability of fault occurrence, and as well to mitigate a fault propagation to other motor parts. Multiphase systems (a phase number greater than three) is a common approach when designing fault tolerant drive systems, considered in [5] and [7] for instance. The relative torque or power loss when one phase is lost, is in this way of course decreased, but to the cost of an increased complexity of the system. A fault-tolerant multiphase system could beneficially be designed with independent phases to be able to operate when a fault occurs, but can also be considered as a redundant system as the number of components (the phases) is increased.

From a machine design point of view, the fractional slot type of PMSM with concentrated windings has been considered as a promising alternative to achieve an independence between phases and to allow for operation during failures in a single phase. In [8], a summary of the opportunities and challenges of the fractional slot concentrated winding PMSM can be found; some of the advantages that are mentioned are high power density, efficiency and fault-tolerance. One of the key challenges that are raised is the reduction of rotor losses since these tend to be high in fractional slot machines. Methods to reduce the rotor losses are investigated by the authors of [9], and in [10] substantial reductions of both rotor iron and permanent magnet losses are shown. The concept of fractional slot PMSM with concentrated windings are used when designing fault-tolerant multiphase machines in both [6] and [11]. The basic design rules of fault-tolerant PMSMs have been presented in [5], one of the key properties of the fault-tolerant design, also according to [6] and [12], is the inductance. The inductance in a single phase should be high enough, in order to limit the short circuit current to adequate levels. The requirement of high phase inductance may indicate cost in terms of a lowered power factor, but in case of an automotive application which is to be operated high up in the field weakening region, it is possibly already fulfilled. The mutual inductance among the phases should be low or null, in order to maintain control over the remaining healthy phases in case of a fault [13].

The unbalanced conditions, associated with the operation during fault, impose additional requirements on both the controller and the converter. A number of fault-tolerant three phase AC drive topologies are compared based on their features and cost in [14], where an approach based on dq-axis limits are used to find potential limits of each of the topologies to operate during asymmetric conditions. The control of electric machines, particularly during phase open circuit fault, has been investigated extensively in the literature. In [15] and [16], similar control methods utilizing resonant controllers are proposed but different converter topologies are considered. Two alternative control methods are suggested in [17], where feed forward terms have been used to compensate for the unbalanced condition. In addition, a number of faults that occur in a PMSM drive system under field weakening operation are investigated in [18].

However, most studies are focused on the control perspective and rather simple machine models are used, often supposing a magnetic linearity. In fact, the asymmetric saturation might be substantial during the unbalanced operation during a fault, which is also pointed out in [19]. This might especially be true in an automotive application, where the size of the machine is already squeezed to a minimum for a high torque density and non-linearity is present even during normal operation. A likely consequence of the individual saturation levels in the different phases, which is not well described in the literature, is a considerable increase of the torque ripple. Moreover, it may also have a strong influence on

the voltage and current limitations which has not been considered in [14] for instance. The unbalanced operation will also cause an unbalanced temperature distribution inside the machine. This could in turn both restrict and expand the possibility to operate the machine during a fault, and also in this case descriptions are missing in literature.

Purpose and main contribution of the thesis

The aim of this thesis is to design a three phase fractional slot PMSM and evaluate the possibility to operate and to deliver an acceptable quality of performance even after a fault occurs. Another part is to compare the fault-tolerant design with a commercially available design, where fault-tolerance was not considered in the design. The machine is to be designed fault-tolerant with a low mutual coupling between the phases and the electrical faults that are to be considered are phase open circuit fault and phase short circuit fault. Some theory and methods that are used throughout the work will finally be evaluated in the lab by utilizing an experimental interior permanent magnet (IPM) machine. This thesis is focused on the machine design perspective, not supposing a magnetic linearity, and the control and converter topologies are treated briefly only.

Some contributions by this work are

- Development and demonstration of a machine design procedure where the relation between machine performance and material cost is considered.
- Design of a fault-tolerant fractional slot PMSM and quantification of its torque speed characteristics and efficiency when it is operated during a single phase open circuit fault or a single phase short circuit fault.
- Introduction of a machine modeling technique that utilizes the weak magnetic coupling between the phases of a fault-tolerant PMSM, in order to model the unbalanced saturation associated with operation during fault more accurately.
- Comparative analysis of the fault-tolerant fractional slot PMSM and two reference PMSM characteristics under normal and single phase open circuit operation.
- Implementation and experimental demonstration of a simplified current controller that handles the single phase open circuit fault operation in the rotating dq-reference frame well.
- An experimentally verified thermal analysis of a PMSM operated during normal conditions and during single phase open circuit fault.

List of publications

1. Du-Bar, C.; Thiringer, T.; Lundmark, S.; Alatalo, M.; , "An electric machine design procedure that includes multiple cost scenarios" presented during the EPE 2016 ECCE Europe Conference, 5-9 September 2016, Karlsruhe, Germany.

2. Du-Bar, C.; Thiringer, T.; Lundmark, S.; Alatalo, M.; , "Modeling of a fault-tolerant PMSM for a vehicle application including asymmetric saturation and torque ripple elimination" Submitted to IEEE Transactions on Energy Conversion.

3. Du-Bar, C.; Åstöm, J.; Thiringer, T.; Lundmark, S.; Alatalo, M.; , "Design of an online temperature monitoring system for an experimental IPM" presented during the XXIIth International Conference on Electrical Machines (ICEM'2016), 4-7 September 2016, Lausanne, Switzerland.

Chapter 1

Machine Design Modeling

This chapter provides some basic machine modeling theory from a machine design perspective. The theory is described on the basis that it is a three phase fractional slot PMSM, a non-integer number of slots per pole per phase, with surface mounted permanent magnets and concentrated double-layer windings that is to be designed. However, it is possible to adapt most of the modeling techniques presented in this chapter to design of other types of machines as well.

1.1 Electric and magnetic loading

In a PMSM with surface mounted permanent magnets, where the inductance is independent of the rotor position, the torque is determined by the flux from the permanent magnets, Ψ_m, and the flux induced by the stator, $\Psi_{ind} = Li$, illustrated in Figure 1.1.

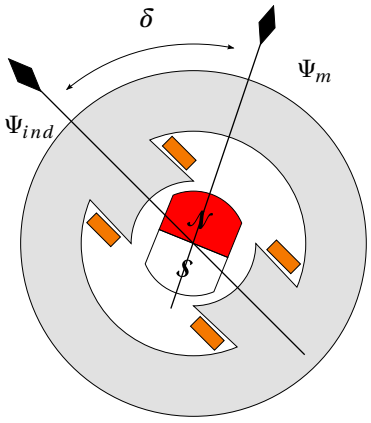

Figure 1.1: Illustration of how torque is produced between two magnetic fields.

The torque production is calculated as the cross-product of two magnetic flux vectors and it can be expressed as,

$$T = \Psi_{ind} \Psi_m sin(\delta) \tag{1.1}$$

where δ is the angle between the vectors. In this case, the electric loading is represented by Ψ_{ind} while the magnetic loading is represented by Ψ_m. In Figure 1.2, different flux waveforms are shown together with a single tooth covering 150^o electrical degrees. Figure 1.2a represents the square shaped flux density in an air-gap with surface mounted permanent magnets that covers 120 electrical degrees or 2/3 of the pole pitch. Since the tooth covers 150 electrical degrees, the permanent magnet flux that links the tooth, ψ_m, can be calculated as

$$\psi_m(\theta) = \int_{\theta-75^\circ}^{\theta+75^\circ} B_m(\theta) d\theta \tag{1.2}$$

which is shown in Figure 1.2b. A tooth that covers 150^o may for example be used in a fractional slot machine with 12 slots and $2p = 10$ poles, more about pole and slot combinations in Section 1.4. One can observe the low harmonic content in the flux that links a single tooth or coil.

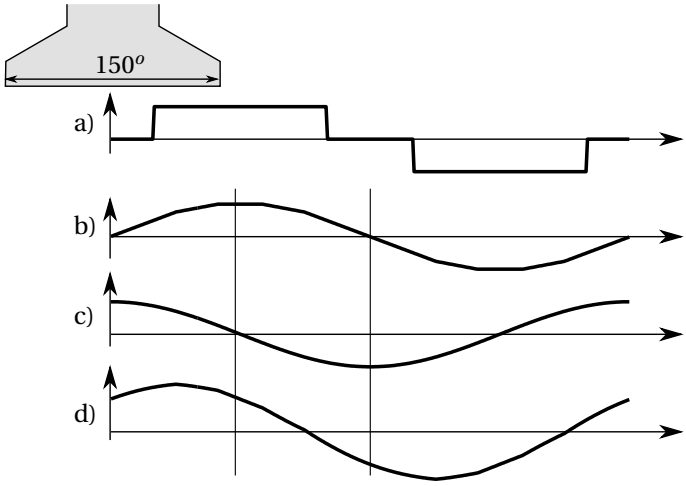

Figure 1.2: Flux wave forms; a) PM air-gap flux density. b) PM flux linked by a single coil or tooth. c) Induced flux in a single coil or tooth for maximum torque. d) Combination of PM and induced flux in a single coil or tooth

In order to maximize the torque in (1.1), the angle, δ, between the induced flux,

Ψ_{ind}, and the permanent magnet flux, Ψ_m, should be 90^o. The induced flux, leading the permanent magnet flux by 90^o, is illustrated in Figure 1.2c. The total flux in the tooth is the sum of the permanent magnet flux and the induced flux,

$$\psi_{tooth}(\theta) = \psi_{ind}(\theta) + \psi_m(\theta) = Li(\theta) + \psi_m(\theta) \tag{1.3}$$

which is shown in Figure1.2d. It should be noticed that the tooth carries a mix of permanent magnet flux and induced flux, although the angle between the permanent magnet flux and the current is 90^o. By studying Figure 1.2 b and c, one can observe that the tooth carries a mix of the two fluxes at all angles except when one of the fluxes is crossing zero. As only one tooth is studied at the moment, one flux has its peak when the other one is zero. This is not true when the coils of several teeth are connected together and if the distribution factor is not ideal, $k_d \neq 1$. The distribution factor will be introduced later in section 1.5. From a design point of view, this implies that flux paths must be designed with respect to the combination of permanent magnet and induced flux levels. Despite the fact that the flux vectors Ψ_{ind} and Ψ_m are orthogonal, they are not independent as they share the same non-linear iron flux paths.

1.2 Permanent magnet flux

As a simple approach, the magnetic flux distribution from a surface mounted permanent magnet can be considered as square shaped with an amplitude B_m, illustrated in Figure 1.3.

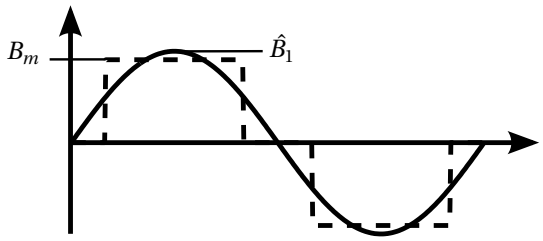

Figure 1.3: Permanent magnet air-gap flux density waveforms.

If the permanent magnets covers 120 electrical degrees or 2/3 of the pole pitch, the peak value of the fundamental, $\hat{B}_1$, can be calculated as,

$$\hat{B}_1 = \frac{4\sqrt{3}}{2\pi} B_m \tag{1.4}$$

A permanent magnet that covers 2/3 of the pole pitch is often considered a suitable choice, due to the utilization of the permanent magnet flux and to achieve a low cogging torque. If the reluctance of the iron paths and the leakage flux are neglected, the required length of the permanent magnets, l_{pm}, is expressed as

$$l_{pm} = \frac{\mu l_g}{\frac{B_r}{B_m} - 1} \tag{1.5}$$

where l_g is the air-gap length, μ the relative permability of the permanent magnets and B_r is the residual flux density of the permanent magnets.

1.3 Core loss and core geometry

Accurate computation of the iron or core losses is a complicated task. The iron losses are often separated into three parts:

- Hysteresis losses
- Eddy current losses
- Excess losses

A number of iron loss models for electrical machines are presented and compared in [20]. One approach is to formulate an expression with three terms, one for each loss part,

$$P_{core} = c_{hyst} f \hat{B}^2 + c_{ec} f^2 \hat{B}^2 + c_{exc} f^{1.5} \hat{B}^{1.5} \tag{1.6}$$

where P_{core} is the core loss volume density and the coefficients are empirical factors. If only considering the hysteresis and eddy current losses at a single frequency,

$$P_{Fe} \propto B^2 V \tag{1.7}$$

where P_{Fe} is the total loss in the volume, V, and B is the flux density. If flux is floating a distance, X_0, from the left to the right in the geometry illustrated in Figure 1.4 and the flux is assumed to be uniformed distributed along a vertical segment,

$$B = \frac{\phi}{A} \tag{1.8}$$

where ϕ is the total flux that crosses each segment and A is the one-dimensional area of a segment in vertical direction.

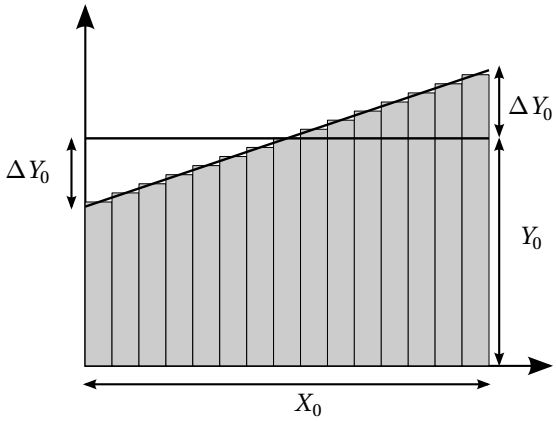

Figure 1.4: Illustration of a segmented flux path volume.

The volume of a single element, V, is the horizontal thickness of a segment, l, multiplied by the one-dimensional area, A. Then, (1.7) and (1.8) together gives,

$$P_{Fe} \propto \frac{1}{A^2} l A = \frac{l}{A} \tag{1.9}$$

which implies that the reluctance, $\mathfrak{R}$, of the path X_0, when carrying the total flux ϕ, should be minimized in order to minimize the core loss since,

$$\mathfrak{R} = \frac{l}{\mu A} \tag{1.10}$$

For a flux path of the length X_0 and the constant core volume $V = X_0 \cdot Y_0$, the variable ΔY_0 is used to vary the shape of the geometry. The reluctance, when dividing the flux path into k segments, can be expressed as

$$\mathfrak{R} = \frac{1}{\mu} \sum_{n=1}^{k} \frac{X_0}{k(Y_0 - \Delta Y_0) + 2\Delta Y_0 n} \tag{1.11}$$

The reluctance in (1.11) has a minimum for $\Delta Y_0 = 0$, corresponding to a constant cross-sectional area along the flux path and evenly distributed flux.
The reasoning in this section together with knowledge about how the flux is divided between different paths can be applied when dimensioning the flux paths. It is beneficial to aim for constant flux densities along flux paths.

1.4 Pole and slot combinations

For a three phase machine, $m = 3$, the total number of poles, $2p$, should be as close as possible to the number of slots, Q_s, in order to maximize the magnetic flux linkage. Equal numbers or a pole pitch of one, $\tau = \frac{Q_s}{2p} = 1$, can't be used if the motor is to be able to produce torque in all rotor positions. The feasible pole and slot combinations are usually described by

$$Q_s = 2p \pm 1 \; or \; 2p \pm 2 \tag{1.12}$$

where Q_s must be a multiple of 3 for a three phase machine. Furthermore, for a three phase machine, the mechanical displacement of the phases must result in an electrical displacement of 120 degrees of the phases, which gives that

$$\frac{360p}{3} = \pm 360k + 120 \qquad k = 0, 1, 2, .. \tag{1.13}$$

All feasible combinations, up to p =14, derived from (1.12) and (1.13) are listed in Table 1.1. It can be noted in Table 1.1 that no combinations where p is a multiple of 3 exist, which is a consequence of (1.12). Further, there is only one combination for p=1 as Q_s must be a multiple of 3 for a three phase machine. Q_s and p for a given combination of Q_s/p can be multiplied by a positive integer to get a new feasible combination.

Table 1.1: Feasible pole and slot combinations for a 3-phase machine.

p	$\mathbf{Q_s = 2p \pm 1}$	$\mathbf{Q_s = 2p \pm 2}$
1	3	-
2	3	6
4	9	6
5	9	12
7	15	12
8	15	18
10	21	18
11	21	24
13	27	24
14	27	30

Using a $Q_s = 2p \pm 1$ combination results in an odd number of coils per phase for a concentrated double-layer wound machine, which will limit the number of possible series and parallel connection of the coils. A $Q_s = 2p \pm 1$ combination

gives also lower number of slots and thereby larger windings for a given pole number.

1.5 Winding factor

The winding factor describes how well flux of a specific harmonic from the rotor side links a phase winding and is determined by the Q_s/p combination and the winding configuration. It is defined as the pitch factor multiplied by the distribution factor [21] which can be seen in (1.14).

$$k_{wn} = k_{pn} k_{dn} \tag{1.14}$$

where the pitch factor, k_{pn}, describes how well flux from a given harmonic links a single coil or tooth. The pitch factor for any Q_s/p combination can be expressed according to

$$k_{pn} = sin(\frac{n\pi p}{Q_s}) \tag{1.15}$$

where $n = 1$ corresponds to the fundamental of each combination [22]. The distribution factor, k_{dn}, is used to include the phase shift between the flux linkage in each coil when summing up the contribution for a given harmonic in a phase. Hence, the formulation of distribution factor is determined by both the Q_s/p combination and the winding configuration. For concentrated double-layer windings k_{dn} can be expressed as [22]

$$k_{dn} = \frac{sin(\frac{n\pi}{2m})}{zsin(\frac{n\pi}{2mz})} \tag{1.16}$$

where n is the harmonic number, m is the number of phases and z is the number of coils in a group. The number of coils in a group can be calculated as,

$$z = \frac{Q_s}{mF} \tag{1.17}$$

where F is the greatest common divisor (GCD) of the number of poles, $2p$, and the number of slots, Q_s.

$$F = GCD(2p, Q_s) \tag{1.18}$$

Winding factors for feasible $Q_s = 2p \pm 2$ combinations up to $p = 13$ are shown in Table 1.2.

Table 1.2: Winding factors for the 1st to the 13th harmonic for feasible $Q_s = 2p \pm 2$ combinations up to $p = 13$.

Q_s/p	**Harmonic number**												
	1	**2**	**3**	**4**	**5**	**6**	**7**	**8**	**9**	**10**	**11**	**12**	**13**
6/2	0.87	0.87	0	-0.87	-0.87	0	0.87	0.87	0	-0.87	-0.87	0	0.87
6/4	0.87	-0.87	0	0.87	-0.87	0	0.87	-0.87	0	0.87	-0.87	0	0.87
12/5	0.93	0.43	-0.50	-0.43	0.07	0	-0.07	0.43	0.50	-0.43	-0.93	0	0.93
12/7	0.93	-0.43	-0.50	0.43	0.07	0	-0.07	-0.43	0.50	0.43	-0.93	0	0.93
18/8	0.95	0.29	-0.58	-0.29	0.14	0	0.06	0.29	0	-0.29	-0.06	0	-0.14
18/10	0.95	-0.29	-0.58	0.29	0.14	0	0.06	-0.29	0	0.29	-0.06	0	-0.14
24/11	0.95	0.22	-0.60	-0.22	0.16	0	0.10	0.22	-0.10	-0.22	0.02	0	-0.02
24/13	0.95	-0.22	-0.60	-0.22	0.16	0	0.10	-0.22	-0.10	0.22	0.02	0	-0.02

1.6 MMF time and space harmonics

Rotor losses caused by the induced magneto motive force (MMF) wave is mentioned as one of the key challenges for fractional slot machines with concentrated windings in [8]. As a first step the rotor losses can be lowered if the source is minimized by a careful choice of pole slot combinations to achieve a favorable MMF wave in the air-gap, why the calculation of time and space harmonics is of great importance. For a given pole/slot combination, the impact of the harmonics in the MMF wave can be affected by geometry and material properties. It is possible to increase the air-gap length and introduce segmentation of the rotor parts in order to prevent the induction of eddy currents on the rotor side. The correlation between pole/slot combinations and rotor losses using different air-gap lengths and rotor surface materials are investigated extensively in [9]. The basic theory of how to analytically calculate the theoretical induced MMF harmonics is very well described in [23] for example. In this section a conceptual explanation follows, based on an example of the $Q_s = 12$ machine.

The MMF wave that is induced in the air-gap when the stator is excited by current can be described by means of MMF time and space harmonics,

$$F(t,\theta) = \sum_n \sum_m F_{nm} sin(m\omega t \pm n\theta + \beta_{mn}) \tag{1.19}$$

where F_{nm} is time m:th order and space n:th order MMF magnitude. The stator together with its winding configuration is illustrated in the bottom of Figure 1.5. Just above the stator, the ideal square wave MMF-wave is plotted together with the dotted MMF-wave built up by the first seven non-zero components of space harmonics. The space harmonic order is defined so that the fundamental period is 2π in mechanical angle. The first seven non-zero components (1, 5, 7, 11, 13, 17, 19) are shown with their respective magnitude and phase above the full MMF-wave. It can be seen that the 5th and the 7th harmonics are of the greatest amplitude, verifying that $Q_s = 12$ stator is suitable for $p = 5$ and $p = 7$, previously shown in Table 1.1.

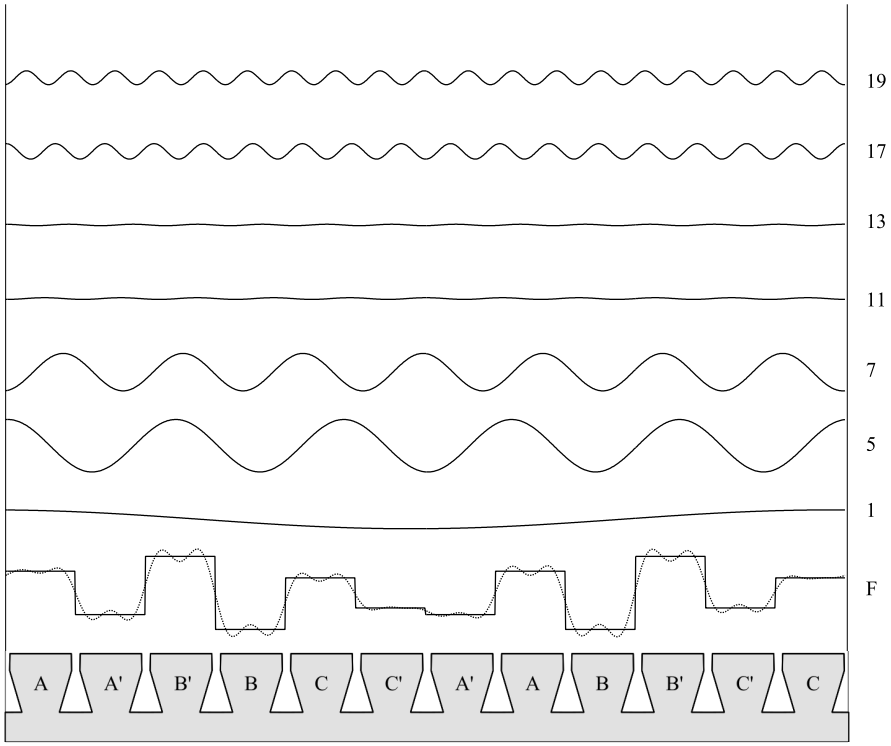

Figure 1.5: MMF-wave and its harmonic content in the air-gap of a $Q_s = 12$ machine.

The MMF harmonics rotate in the air-gap with different speeds, as all harmonics travel one wave-length during one period, the mechanical speed of the n:th MMF harmonic in the stator reference frame can be calculated as [9]

$$\omega_{ns} = \frac{\omega}{sign \cdot n} \tag{1.20}$$

where sign is either $+1$ or -1 depending on travel-direction of the n:th harmonic.The sign-function is defined as two series of harmonics that travel in the opposite direction [9]

$$n = 1 + 3k \qquad k = 0, 1, 2, ... \tag{1.21}$$

and

$$n = 2 + 3k \qquad k = 0, 1, 2, \ldots \tag{1.22}$$

A positive sign is conventionally assigned to the series containing the main harmonic ($n = p$). The harmonic content of the MMF-wave in a $p = 5$ and $p = 7$ machine respectively are shown in Figure 1.6. The amplitudes are expressed in relation to the fundamentals which corresponds to the red bar. Positive values indicate that the harmonics are traveling in the same direction as the fundamental and negative values in the opposite direction.

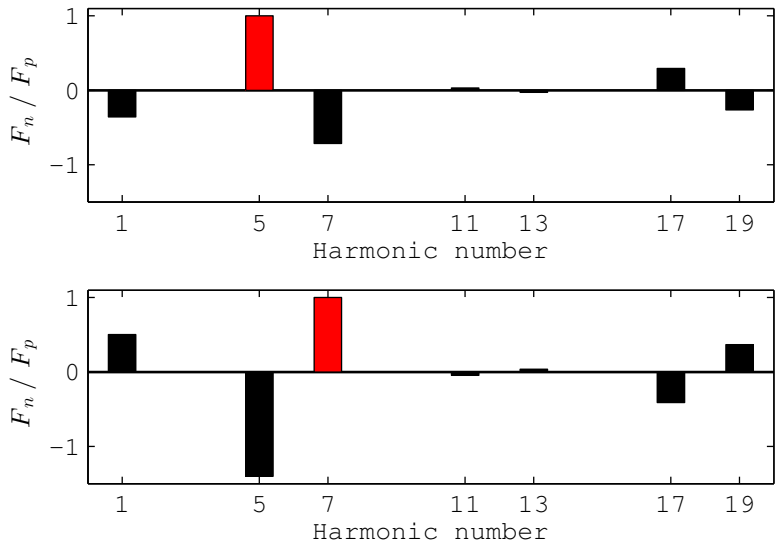

Figure 1.6: Harmonic content in the air-gap for the $p = 5$ and $p = 7$ machine respectively, the amplitudes are related to the fundamentals which corresponds to the red bars.

When it comes to the losses on the rotor side due to the MMF harmonics in the air-gap, it is the traveling speed of the n:th harmonic relative to the fundamental, $n = p$, that is of interest. Ideally, the fundamental will travel with the same speed as the rotor and only induce a constant magnetic flux seen from the rotor. The rest of the harmonics will travel with a speed that is not the same as the rotor and hence introduce an alternating magnetic flux that may cause losses on the rotor side. As consequence, the rotors of the $p = 5$ and the $p = 7$ machines will experience different harmonics when using the same stator, $Q_s = 12$. The frequency of the MMF seen from the rotor side can be expressed as

$$f_{rn} = f\left|sign - \frac{n}{p}\right| \tag{1.23}$$

Figure 1.7 shows the relative frequency of the MMF harmonics on the rotor side. It can be noticed that some MMF harmonics have the same relative frequency on the rotor side, the 1st and the 11th for the p=5 for instance. This since the 1st rotate in the opposite direction related to the fundamental (5-(-1)=6) while the 11th rotate in the same direction as the fundamental (11-5=6).

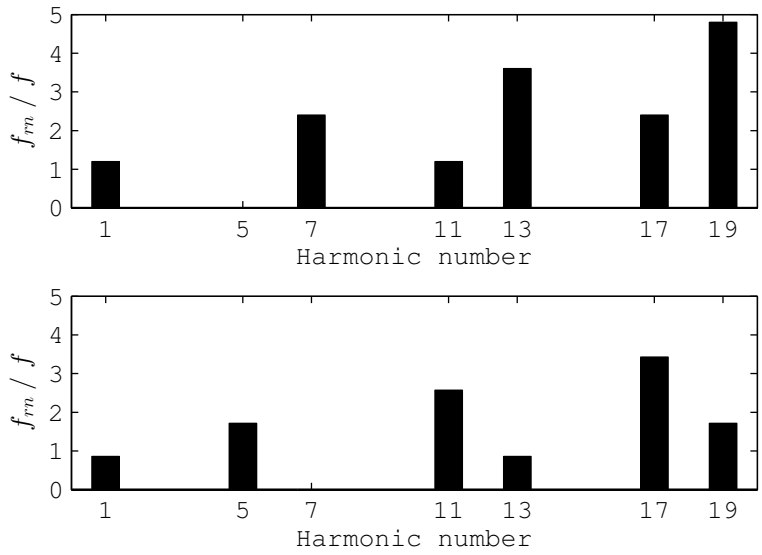

Figure 1.7: Relative frequency of the MMF harmonics on the rotor side. The frequency of the fundamental $n = p = 5$ and $n = p = 7$ equals zero for both configurations.

The rotor losses caused by the MMF harmonics for different pole slot combinations are determined by the presence of harmonics, the amplitude of the harmonics, the relative frequency of the MMF harmonics on the rotor side together with the harmonic number (physical wave length in relation to the rotor geometry). Subharmonics, $n < p$, especially $n = 1$ which is present for both the machines in Figure 1.6 might be considered as extra critical as a wave length covers the whole air-gap. An MMF harmonic covering the whole air-gap means a flux path across the whole rotor and potentially deep flux penetration of the rotor structure. A strategy to reduce the flux produced by an undesirable harmonic, and thereby the losses, is to increase the reluctance of the flux path used by that specific harmonic without affecting the flux path of the fundamental.

Introduction of different flux barriers to prevent flux caused by subharmonics are presented in [24] and [10].

1.7 Inductance calculation

One way of analytically calculating the flux and the inductance of an electric machine is to create a reluctance circuit; a reluctance circuit of a 12 slot machine is shown in Figure 1.8. Different paths of the magnetic circuit of the machine are lumped together into their corresponding reluctance elements. Each reluctance element is determined by the geometric properties of the machine parts together with its material properties. The reluctance circuit is then excited by magneto motive forces (MMFs) corresponding to the product of the current and the number of turns in the coils.

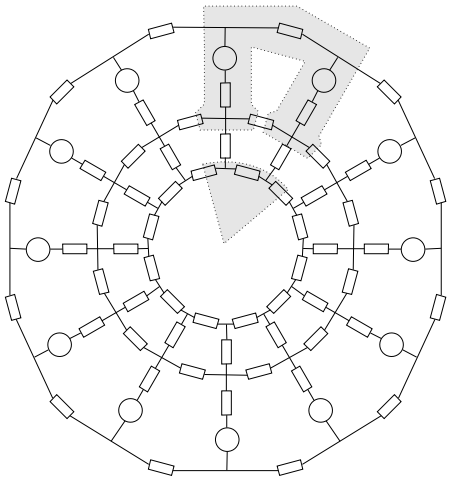

Figure 1.8: A reluctance circuit that represents a complete 12 slot machine.

A column vector, $\mathbf{\Phi}$, that consists of the magnetic flux in the loops of the reluctance circuit can be calculated as

$$\mathbf{\Phi} = \mathfrak{R}^{-1} \boldsymbol{MMF} \tag{1.24}$$

where $\mathfrak{R}$ is a matrix that describes the reluctance circuit and $\boldsymbol{MMF}$ is a vector that corresponds to the MMF-sources in each flux loop in Figure 1.9. The flux in each tooth can then be calculated as the difference between the fluxes in the two loops on each side of the tooth. In Figure 1.9, the reluctance circuit is built up by

five different reluctance elements. A similar reluctance circuit and analytically expressions for the reluctance element are presented in [25].

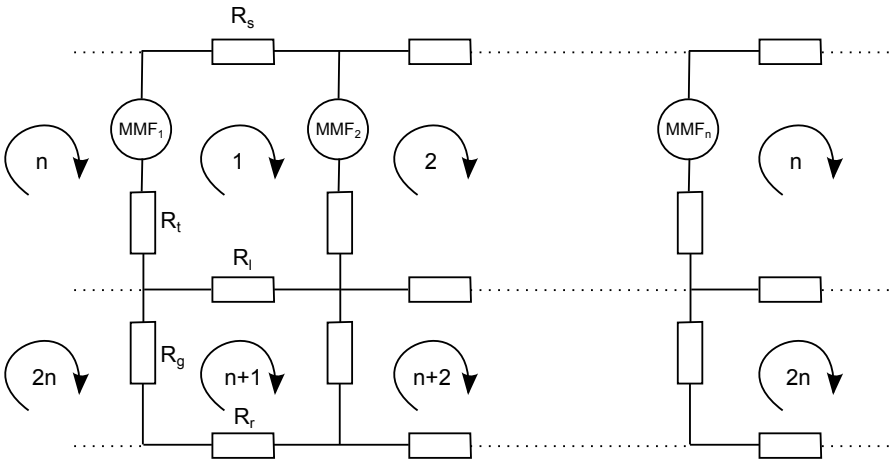

Figure 1.9: Schematic representation of a reluctance circuit for a machine with an arbitrary number of slots, $Q_s = n$.

The reluctance matrix can be expressed as

$$\mathfrak{R} = \begin{bmatrix} (\sum_{k=1}^{2n} R_{1,k}) & -R_{1,2} & -R_{1,3} & \cdots & -R_{1,2n} \\ -R_{2,1} & (\sum_{k=1}^{2n} R_{2,k}) & -R_{2,3} & \cdots & -R_{1,2} \\ \vdots & \vdots & \vdots & & \vdots \\ -R_{2n,1} & -R_{2n,2} & -R_{2n,3} & \cdots & (\sum_{k=1}^{2n} R_{2n,k}) \end{bmatrix} \tag{1.25}$$

where $R_{k,l}$ is the reluctance element that serves as a path for the flux both for the flux in loop k and loop l. Therefore, $R_{1,2} = R_t$, since the element R_t is a path in both loop 1 and loop 2, as seen in Figure 1.9. As a second example; $\sum_{k=1}^{2n} R_{1,k} = R_s + R_t + R_l + R_t$.

The n first elements in the MMF column vector can then be written as

$$\boldsymbol{MMF}(1:n) = \begin{bmatrix} MMF_1 - MMF_2 \\ MMF_2 - MMF_3 \\ \vdots \\ MMF_{n-1} - MMF_n \\ MMF_n - MMF_1 \end{bmatrix} \tag{1.26}$$

where the winding direction or the coil configuration of each coil with respect to the direction of the flux loop must be taken into account. The rest of the MMF column vector is zero, $\boldsymbol{MMF}(n+1:2n)=0$, as there are no coils or current excitation on the rotor side.

The calculated flux in each tooth can now be summed up for each phase to calculate the flux linkage in the corresponding phases. The self-inductance of phase a relates the flux of phase a, linking the coils of phase a and the current in phase a as follows

$$L_{aa} = \frac{\psi_{aa}}{i_a} \tag{1.27}$$

The mutual inductance between phase a and b relates the flux from phase a, linking the coils of phase b and the current in phase a

$$L_{ab} = \frac{\psi_{ab}}{i_a} \tag{1.28}$$

1.8 Heat transfer modeling

The three modes of heat transfer, conduction, convection and radiation are often translated into a simplified model, where equivalent conduction heat transfer coefficients are calculated for the later two. I that way, a thermal heat conduction problem is created, which can easily be solved using FEA. The problem can be simplified further, by lumping parts of the domain together in order to create a lumped parameter thermal model, which can be solved as an equivalent electric circuit. The heat transfer rate, q, between two nodes connected by the thermal resistance, R_{th}, can be calculated as

$$q = \frac{\Delta T}{R_{th}} \tag{1.29}$$

where ΔT corresponds to the temperature difference between the two nodes. The thermal resistance, R_{th}, is inversely proportional to the thermal conductance, G,

$$R_{th} = \frac{1}{G} = \frac{l}{\lambda A} \tag{1.30}$$

which can be calculated based on the length, l, the cross-sectional area, A, and the thermal conductivity, λ, of the segment or the sub-domain. In order to model the thermal transient behavior, the energy storage in the domain must be taken into account. In the equivalent electric circuit of a lumped parameter thermal model, this can be modeled as a capacitor

$$C_{th} = \rho V c_p \tag{1.31}$$

where ρ is the density of the material, V is the volume represented by the node and c_p is the specific heat of the material.

For most of the solid parts of the machine structure, it is possible to apply (1.30) and (1.31) more or less directly, even if the material properties vary with temperature and the cross-sectional area, A, varies along the length, l, of a segment. However, even if the end effects inside the machine are not taken into account there are still some regions or parts that are less straightforward, the composition of materials in the slots and the strongly speed dependent heat convection across the air gap. The modeling of these regions are described in more detail in the following sections.

1.8.1 Thermal conductivity of the winding mix

When modeling the thermal characteristics of the windings, the copper conductors and the impregnation material between the conductors are often treated as a mix material with an equivalent thermal conductivity. As the thermal conductivity of copper is much higher than for the impregnation material, (1:1833) in [26], both the conductivity of the impregnation material and the distribution of the copper wires are of great importance when determining an equivalent thermal conductivity of the material mix. Conductors of the same size placed in a hexagon pattern and a square pattern with the same fill-factor are illustrated in Figure 1.10. The hexagon pattern gives a longer shortest path between the conductors which results in a lower equivalent thermal conductivity compared to the square pattern distribution, when the same fill-factor is considered.

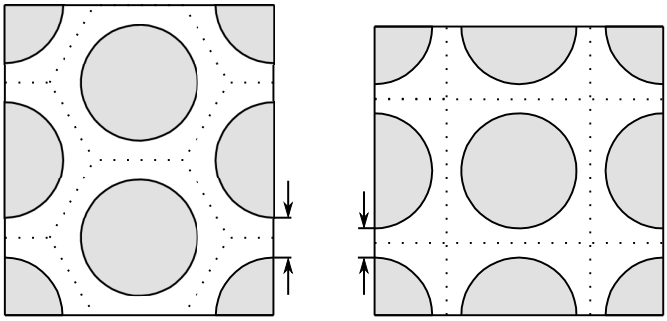

Figure 1.10: Hexagon and square pattern distribution of conductors, the conductors have the same size and the same fill-factors are used.

Using FEA, equivalent thermal conductivity that are calculated for hexagon[1] and square pattern distributions as function of the copper fill-factor are presented in Figure 1.11 and Figure 1.12, for two different values of thermal conductivity of the impregnation material. It can be seen that the equivalent thermal conductivities increase dramatically when the fill-factors are approaching the theoretical maximal fill-factors, $\frac{\pi}{4} \approx 0.79$ and $\frac{\pi}{2\sqrt{3}} \approx 0.91$, for square and hexagon distribution respectively. The figures show clearly the impact of the conductor distribution and the thermal conductivity of the impregnation material for all combinations. The impact of the fill-factor on the relative increase of the equivalent thermal conductivity is significant at already very high fill-factors. From a strictly thermal perspective it's therefore beneficial to aim for even a slight increase of an already very high fill-factor.

Interesting improvements of the performance at the thermal limit for two segmented PMSMs using wound windings (fill-factor of 61%) and using pre-pressed windings (fill-factor of 78%) are presented in [27]. In [28], thermal properties for a mix of Litz wire and impregnation material, using two impregnation techniques, are derived experimentally. The first sample, that was varnish dipped, shows an equivalent thermal conductivity of 1.2-1.6 W/(m·K) while the second sample, that was epoxi impregnated using a vacuum chamber, shows an equivalent thermal conductivity of 2.9-7.4 W/(m·K).

[1] The thermal conductivity of the hexagon pattern distribution is anisotropic and the equivalent thermal conductivity is calculated corresponding to heat flux in the horizontal direction in Figure 1.10.

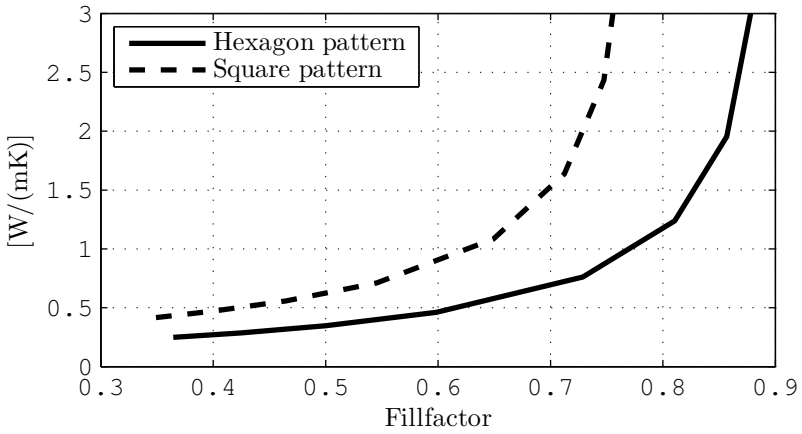

Figure 1.11: Equivalent thermal conductivity for winding mix for an impregnation conductivity of 0.2 W/(m·K).

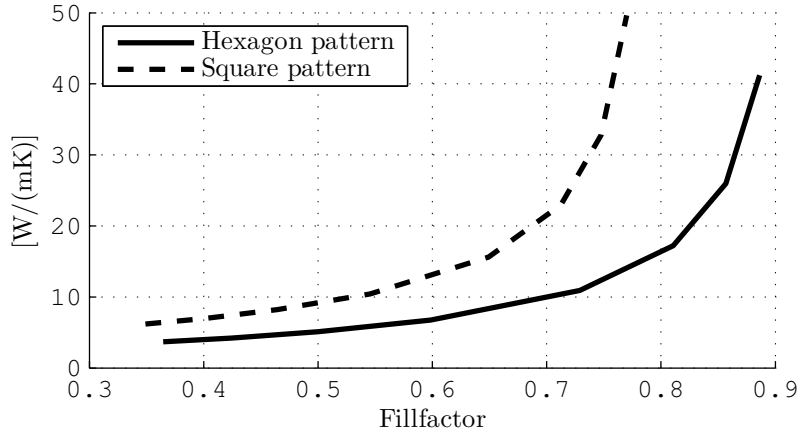

Figure 1.12: Equivalent thermal conductivity for winding mix for a impregnation conductivity of 3 W/(m·K).

1.8.2 Thermal conductivity in the air gap

In the literature, a number of similar methods to calculate the air gap heat transfer coefficient, based on the measurements in [29] and [30], is presented. The major differences of the models is the critical levels for the Taylor number which determines which air flow types that occur in the air gap, and the approximation of the Nusselt number. Here follows a brief description of the method used

in this thesis, which is based on [31].

The thermal resistance across the air gap can be calulated as

$$R_{th,g} = \frac{1}{h_g A_g} \tag{1.32}$$

where h_g is the air gap heat transfer coefficient and A_g is the cylindrical area in the middle of the air gap. The heat transfer coefficient can be expressed as

$$h_g = \frac{Nu\,\lambda_{air}}{2 l_g} \tag{1.33}$$

where Nu is the Nusselt number, λ_{air} is the thermal conductivity of air and l_g is the air gap length. The Nusselt number can be calculated from the modified Taylor number Ta_m as

$$\begin{array}{lll} Nu = 2 & (Ta_m < 1700) & \text{laminar flow} \\ Nu = 0.128\,{Ta_m}^{0.367} & (1700 < Ta_m < 10^4) & \text{transitional flow} \\ Nu = 0.409\,{Ta_m}^{0.241} & (10^4 < Ta_m < 10^7) & \text{fully turbulent flow} \end{array} \tag{1.34}$$

The modified Taylor number, Ta_m, can be found from the Taylor number, Ta, and the geometrical factor, F_g, as

$$Ta_m = \frac{Ta}{F_g} \tag{1.35}$$

where the Taylor number can be calculated as

$$Ta = \frac{\rho_{air}^2 \Omega^2 r_g l_g^3}{\mu_{air}^2} \tag{1.36}$$

while ρ_{air} is the mass density of air, Ω is the mechanical angular speed of the rotor, r_g is the average air gap radius and μ_{air} is the dynamic viscosity of air. Finally, the geometrical factor can be found as

$$F_g = \frac{\pi^4\left(\frac{2r_g - 2.304l_g}{2r_g - l_g}\right)}{1697\left(0.0056 + 0.0571\left(\frac{2r_g - 2.304l_g}{2r_g - l_g}\right)^2\right)\left(1 - \frac{l_g}{2r_g}\right)} \tag{1.37}$$

1.8.3 Temperature impact on copper resistivity

The copper resistivity as function of temperature can be calculated according to

$$\rho_{Cu}(T) = \rho_{Cu,20}\big(1 + \alpha(T - 20)\big) \tag{1.38}$$

where the resistivity at 20°C, $\rho_{Cu,20}$, is put to $1.68 \cdot 10^{-8}\Omega$m and the temperature coefficient, α, is put to 0.39 %/K. When modeling the winding temperature for a given phase current, it becomes rather sensitive due to the positive feedback when using (1.38). A higher temperature increases the copper losses which in turn increases the temperature and so on. The same phenomena, with a risk for thermal runaway is of course present in reality as well. It can potentially lead to a strong reduction of the possible overloading time of a machine.

Chapter 2

Dynamic Modeling of PMSMs

This chapter deals with the the dynamic modeling of PMSMs under balanced and unbalanced or faulty conditions, the unbalanced conditions impose additional requirements of the controller and the converter. Some controllers and converter topologies that can handle the unbalanced operation are therefore presented. The reader is expected to be familiar with general machine modeling and the transformations between the different reference frames that are associated with both machine modeling and control, which are well described in [32] for example.

2.1 Basic 3ph-model

The electrical equations, expressing the phase voltages of a three phase PMSM can be written on matrix form as

$$\begin{bmatrix} v_a \\ v_b \\ v_c \end{bmatrix} = \begin{bmatrix} L_{sa} & L_{sab} & L_{sac} \\ L_{sab} & L_{sb} & L_{sbc} \\ L_{sac} & L_{sbc} & L_{sc} \end{bmatrix} \frac{d}{dt} \begin{bmatrix} i_a \\ i_b \\ i_c \end{bmatrix} + \begin{bmatrix} R_s & 0 & 0 \\ 0 & R_s & 0 \\ 0 & 0 & R_s \end{bmatrix} \begin{bmatrix} i_a \\ i_b \\ i_c \end{bmatrix} + \begin{bmatrix} e_a \\ e_b \\ e_c \end{bmatrix} \tag{2.1}$$

where e_a, e_b and e_c are the back EMF terms of each phase [33]. If the flux from the permanent magnets are considered to be sinusoidal and symmetrically placed towards each other, the back EMF terms can be formulated as

$$\begin{bmatrix} e_a \\ e_b \\ e_c \end{bmatrix} = \omega \Psi_m \begin{bmatrix} cos(\theta) \\ cos(\theta - \frac{2\pi}{3}) \\ cos(\theta - \frac{4\pi}{3}) \end{bmatrix} \tag{2.2}$$

where ω is the electric angular frequency and Ψ_m is the magnitude of the flux linkage in a phase. Further, the self inductance of the phases are equal and they can be denoted

$$L_{sa} = L_{sb} = L_{sc} = L \tag{2.3}$$

Also the mutual coupling between all phases are the same and it can be denoted

$$L_{sab} = L_{sac} = L_{sbc} = M \tag{2.4}$$

For a balanced three phase system where $i_a + i_b + i_c = 0$ and utilizing $L_s = L - M$, (2.1) can be rewritten as

$$\begin{bmatrix} v_a \\ v_b \\ v_c \end{bmatrix} = \begin{bmatrix} L_s & 0 & 0 \\ 0 & L_s & 0 \\ 0 & 0 & L_s \end{bmatrix} \frac{d}{dt} \begin{bmatrix} i_a \\ i_b \\ i_c \end{bmatrix} + \begin{bmatrix} R_s & 0 & 0 \\ 0 & R_s & 0 \\ 0 & 0 & R_s \end{bmatrix} \begin{bmatrix} i_a \\ i_b \\ i_c \end{bmatrix} + \begin{bmatrix} e_a \\ e_b \\ e_c \end{bmatrix} \tag{2.5}$$

For a machine without rotor saliency, the inductance is not dependent on the rotor position and no reluctance torque can be created. Hence, the electrodynamic torque can be expressed as

$$T_e = \frac{i_a e_a}{\Omega} + \frac{i_b e_b}{\Omega} + \frac{i_c e_c}{\Omega} \tag{2.6}$$

where Ω represents the mechanical angular frequency.

2.2 Flux model in the rotating dq-reference frame

In the rotating dq reference frame, the stator voltage of a PMSM can be expressed as

$$u_d = R_s i_d + L_d \frac{d i_d}{d t} - \omega L_q i_q \tag{2.7}$$

$$u_q = R_s i_q + L_q \frac{d i_q}{d t} + \omega L_d i_d + \omega \Psi_m \tag{2.8}$$

where only the fundamental frequency component is considered and the permanent magnet flux is oriented in the direct axis. The electrodynamic torque can be written as

$$T_e = \psi_d i_q - \psi_q i_d \tag{2.9}$$

If the flux components are expressed as $\psi_d = \Psi_m + L_d i_d$ and $\psi_q = L_q i_q$, the torque equation (2.9) can be rewritten as

$$T_e = \Psi_m i_q + (L_d - L_q) i_d i_q \tag{2.10}$$

which is a widely used expression. Using this model for a non-linear machine, it is problematic to divide the direct axis flux, ψ_d, into its PM flux component, Ψ_m and its induced flux component, $L_d i_d$. Both Ψ_m and $L_d i_d$ share the same non-linear flux paths, as previously shown in Figure 1.2 in Section 1.1. Consequently, both Ψ_m and L_d are functions of the currents, i_d and i_q, and it is thereby possible to divide ψ_d in an infinite number of combinations of Ψ_m and $L_d i_d$ if no further assumptions are introduced.

Another possibility is to model the PMSM based on the flux including all harmonics without dividing the direct axis flux into PM and induced flux. The flux in the direct and quadrature axes are both functions of the currents and the rotor position

$$\psi_d = \psi_d(i_d, i_q, \theta) \tag{2.11}$$

$$\psi_q = \psi_q(i_d, i_q, \theta) \tag{2.12}$$

where the rotor angle, θ, must be varied within an interval determined by the pole/slot combination and winding configuration. Equation (2.11) and (2.12) are rather impractical since the fluxes vary in three dimensions. If only considering the fundamental frequency and a steady-state operating point, (2.7) and (2.8) can be rewritten as

$$u_d = R_s i_d - \omega \Psi_q \tag{2.13}$$

$$u_q = R_s i_q + \omega \Psi_d \tag{2.14}$$

where both Ψ_d and Ψ_q represent the amplitudes of the fundamental component of the flux linkage in the direct and quadrature axis respectively. A set of Ψ_d and Ψ_q as function of i_d and i_q can be calculated by means of FEA, using (2.13) and (2.14). Thus, the fundamental phase voltage at a steady-state operating point can be found accurately.

2.3 Basic modeling of chosen faults

The three phase model presented in (2.1) can be written on the general state space form

$$\dot{x} = Ax + Bu \tag{2.15}$$

$$y = Cx + Du \tag{2.16}$$

In the state space model of the machine, the currents represent the states, the current derivatives the state derivatives, while the input voltage is used as input and it becomes

$$\frac{d\boldsymbol{i}}{dt} = -inv(\boldsymbol{L})\boldsymbol{R}\boldsymbol{i} + inv(\boldsymbol{L})\boldsymbol{v} - inv(\boldsymbol{L})\boldsymbol{e} \tag{2.17}$$

The corresponding $\boldsymbol{A}$ and $\boldsymbol{B}$ matrices can then be expressed as

$$\boldsymbol{A} = -inv(\boldsymbol{L})\boldsymbol{R} \tag{2.18}$$

$$\boldsymbol{B} = inv(\boldsymbol{L}) \tag{2.19}$$

The three phase model can then be implemented as follows

$$\frac{d}{dt}\begin{bmatrix} i_a \\ i_b \\ i_c \end{bmatrix} = \boldsymbol{A}\begin{bmatrix} i_a \\ i_b \\ i_c \end{bmatrix} + \boldsymbol{B}\begin{bmatrix} v_a \\ v_b \\ v_c \end{bmatrix} - \boldsymbol{B}\begin{bmatrix} e_a \\ e_b \\ e_c \end{bmatrix} \tag{2.20}$$

where

$$\boldsymbol{A} = \begin{bmatrix} A_{11} & A_{12} & A_{13} \\ A_{21} & A_{22} & A_{23} \\ A_{31} & A_{32} & A_{33} \end{bmatrix} \tag{2.21}$$

and

$$\boldsymbol{B} = \begin{bmatrix} B_{11} & B_{12} & B_{13} \\ B_{21} & B_{22} & B_{23} \\ B_{31} & B_{32} & B_{33} \end{bmatrix} \tag{2.22}$$

which is referred to in the following sections, where it has been manipulated to include phase open and phase short circuit faults.

2.3.1 Phase short circuit

The suggested phase short circuit fault manipulation of (2.20) is probably the most straightforward. The terminal phase voltage of the faulty phase, v_i, is simply put to zero. Characteristics of the short circuit connection might be added by manipulation of the R and L matrices if desired.

2.3.2 Phase open circuit

Two different ways of phase open circuit manipulation are presented. The first changes instantaneously from normal operation to phase open circuit operation while the second takes the transition into account.

State and energy removed

In the most simple approach, the simulation stops when a fault occurs. The states in the machine model (and possible other states such as values in the integrator parts of controllers) are saved. The model is then changed, the state that represents the faulty phase is removed. The saved states are then used as initial conditions when starting the simulation of the new model that represents the characteristics after the fault occurred. As a consequence, energy is removed when the state corresponding to current in the faulty phase is removed.

State and energy conserved

As a second approach , the state corresponding to the current in the faulty phase is controlled to zero; instead of just put the current in the faulty phase to zero and thereby removing the energy instantaneously. From a simulation perspective it is beneficial to control the current to interrupt like a first order system, see Figure 2.1. The voltage that has to build up over the phase winding is calculated and used as input signal to the state space model, where all states still are remaining.

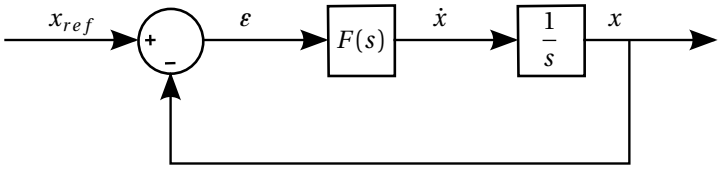

Figure 2.1: Illustration of how the derivative of the state can be controlled.

To get the behavior of a first order system, from the state reference, x_{ref}, to the state value, x, it can be shown that $F(s) = \alpha$, where α is the bandwidth of the first order system. The state derivative, representing the faulty phase, in the state space model can then be expressed as

$$\dot{x} = \alpha(x_{ref} - x) \tag{2.23}$$

when a fault occurs. The voltage that must build up over the phase winding (phase c is used in this case) is calculated as

$$v_c = \frac{\alpha(0 - i_c) - A(3,1:3)i(1:3) - B(3,1:2)u(1:2) + B(3,1:3)e(1:3)}{b(3,3)} \tag{2.24}$$

2.4 Converter limitations

Using the ordinary three leg converter that is shown in Figure 2.2a, it is not possible to control the phase currents individually in case of a phase open circuit or a phase short circuit. The current into one of the remaining phases must equal the current that goes out from the second healthy phase. Three alternative converter topologies are therefore described briefly.

The converter topology illustrated in Figure 2.2b is equipped with a fourth leg that is connected to the star of the Y-connected phases. Thanks to the fourth leg, it is possible to control the remaining phases individually if one phase is lost. A second example of connecting the star point is shown in Figure 2.2c, where it is made possible to connect the star point to the middle of the DC-link by an additional switch or relay. This configuration saves one switch and the control of the fourth phase leg compared to the solution in Figure 2.2b, as the switch is constantly closed in case of a fault. This configuration has been utilized in [16].

The last example is the six leg converter that can be seen in Figure 2.2d, where each phase winding is connected to its own H-bridge. The six leg converter is considered in [15] for instance. The six leg converter offers the greatest degree of freedom, but the number of switches and phase cables are doubled compared to the ordinary three phase converter. For the same power level, the product of the number of switches and the rating of each switch ($V \cdot I$) is increased by a factor $2/\sqrt{3} \approx 1.15$ for the six leg inverter compared with an ordinary three leg converter [6]. In the same manner as in [6], it can be shown that total cross-sectional area of the copper in the six cables of a six leg converter is also increased by a factor $2/\sqrt{3} \approx 1.15$ compared to the three cables of an ordinary three leg converter, when the same DC-link voltage level and current density are considered. An advantage among other, is that a phase can be completely short circuited to limit the short circuit current in case of a turn to turn short circuit fault, while it is still possible to control the two remaining phases.

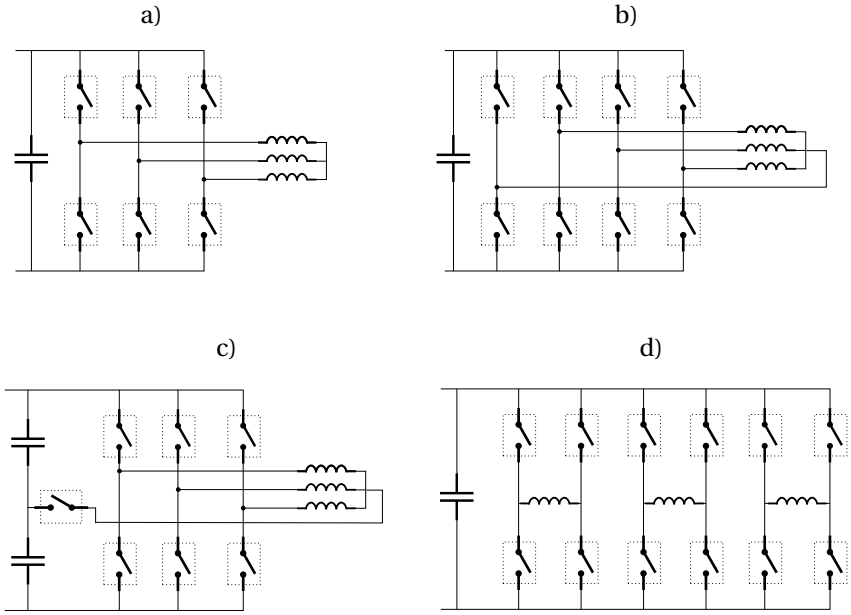

Figure 2.2: Four different converter topologies.

The three colored vectors on the left hand side in Figure 2.3 represent the physical arrangement of the windings in a three phase machine, distributed 120 electrical degrees apart. If they are denoted $\bar{\mathbf{x}}_\mathbf{i}$, the orientation of each phase can be expressed as

$$\bar{\mathbf{x}}_\mathbf{a} = e^{j0} \tag{2.25}$$

$$\bar{\mathbf{x}}_\mathbf{b} = e^{j2\pi/3} \tag{2.26}$$

$$\bar{\mathbf{x}}_\mathbf{c} = e^{-j2\pi/3} \tag{2.27}$$

The three phase currents that are sinusoidal and 120 electrical degrees apart can be written as

$$I_a = \hat{I} sin(\omega t) \tag{2.28}$$

$$I_b = \hat{I} sin(\omega t - 2\pi/3) \tag{2.29}$$

$$I_c = \hat{I} sin(\omega t + 2\pi/3) \tag{2.30}$$

and they are shown in the right hand side of Figure 2.3. Using the physical arrangement of the windings and the current waveforms together, the induced flux from the stator can be expressed as

$$\overline{\boldsymbol{\Psi}}_{\boldsymbol{s}} = L(\overline{\mathbf{x}}_{\mathbf{a}} I_a + \overline{\mathbf{x}}_{\mathbf{b}} I_b + \overline{\mathbf{x}}_{\mathbf{c}} I_c) \tag{2.31}$$

where L is the phase inductance and there is no mutual inductance between the phases. $\overline{\boldsymbol{\Psi}}_{\boldsymbol{s}}$ is a vector, with constant magnitude, that rotates with the electric frequency and follows the dotted circle shown in Figure 2.3.

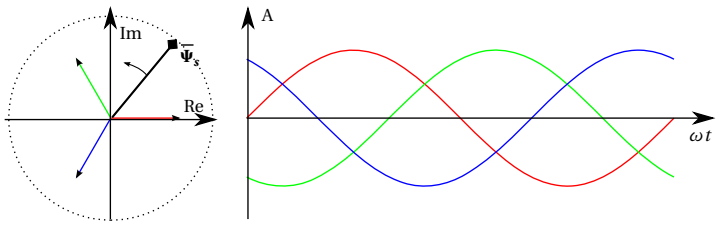

Figure 2.3: Normal operation, phase shift of 120 electrical degrees between the phase currents.

If one phase is lost, phase C, and the two remaining currents are left unaltered, the induced flux, $\overline{\boldsymbol{\Psi}}_{\boldsymbol{s}}$, will rotate with the electric frequency and a time varying amplitude as illustrate in Figure 2.4. If considering the physical arrangement of the windings in Figure 2.4, it can be seen directly that there is only one phase, phase B, that can induce flux in the direction of the imaginary axis.

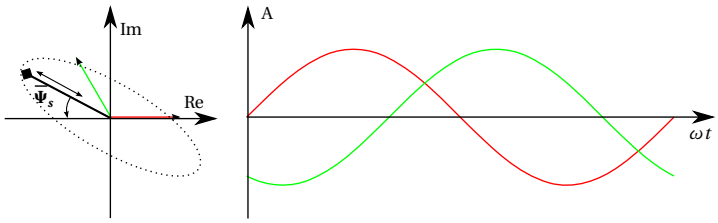

Figure 2.4: One phase lost, phase shift of 120 electrical degrees between the two remaining phase currents.

The maximum flux that can be induced in the direction of the imaginary axis is therefore $imag(\overline{\mathbf{x}}_{\mathbf{b}} I_b L) = \hat{I} \cdot cos(\pi/6) \cdot L$. It can easily be shown that the balanced three phase system gives a constant flux magnitude of $1.5 \cdot \hat{I} \cdot L$, previously represented by the dotted circle in Figure 2.3. In order to maintain a constant

magnitude of the flux vector, the two remaining currents must be phase shifted, which is shown in Figure 2.5. The flux is reduced to $cos(\pi/6)/1.5 = 1/\sqrt{3} \approx 0.58$ of the balanced case.

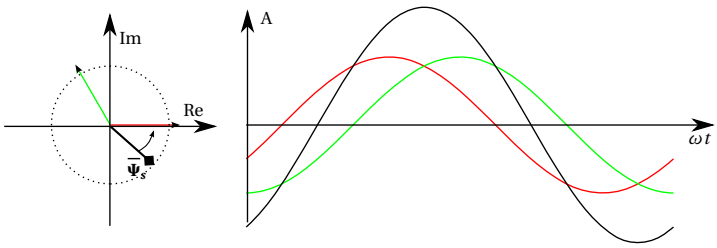

Figure 2.5: One phase lost, phase shift of 60 electrical degrees between the two remaining phase currents.

The black curve in Figure 2.5, represents the sum of I_a and I_b which is the current that must be conducted through the the fourth phase leg or the switch to the middle of the DC-link in Figure 2.2. The current from the star point is $2\hat{I}cos(\pi/6) = \hat{I}\sqrt{3}$, as the angle between the two phase currents are 60 electrical degrees. As a consequence, it is therefore necessary to rate the fourth leg or the switch $\sqrt{3}$ times higher than the ordinary phase legs to be able to keep the same amplitude of the two remaining phase currents.

2.5 Control

This section presents the two controllers that are used when the machines are operated during single phase open circuit fault and single phase short circuit fault. The ordinary PI controller, that is suitable for balanced three phase control is not explained in detail as it is very well established within electric machine control. Adding a resonant controller in parallel with an existing PI controller is the first proposal for operation of the machines under faulty and unsymmetrical conditions. The second suggestion, that has also been tested in the lab, is to modify the ordinary PI controller with additional angle transformations in order to be used during single phase open circuit faults as well.

2.5.1 Ordinary PI controller

When the ordinary PI controller is used in the dq0 reference frame, the rotating three phase quantities are transformed to stationary quantities in the rotating dq0 reference frame via the stationary $\alpha\beta 0$ reference frame. In case of a balanced three phase system in steady-state, all the dq0-components will appear as DC-values which the PI controller is well adapted for. The PI controller is represented as the lower part in the combined resonant and PI controller in Figure 2.6 in section 2.5.2.

2.5.2 Resonant and PI controller

In case of an unbalanced three phase system, as will appear under a phase open circuit and short circuit fault condition, the transformed direct, quadrature and zero sequence components of the three phase quantities will not all be constant values at the same time. As a result, one or several of the dq0-components will be oscillating. Therefore, the ordinary PI controller, that greatly can handle the transformed DC-values under normal conditions, is not a good choice to control the machine currents under faulty conditions. One method, suggested by [15], is to add a resonant controller in parallel with the ordinary PI-controller, which is shown in Figure 2.6.

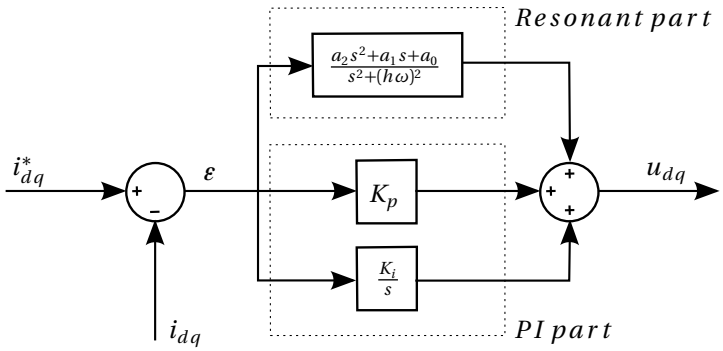

Figure 2.6: Combined resonant and PI controller.

In case of a machine with surface mounted permanent magnets and no rotor saliency, no reluctance torque is expected as $L_d = L_q$, and it is only necessary to keep the torque producing q-component of the current constant. On the other hand, for a machine with a difference between the direct and quadrature axis inductance it is also necessary to hold the d-component of the current constant. The proposed current controller will force both the q and the d components of the current to constant values, while the zero sequence component that does not produce torque is left oscillating.

2.5.3 PI controller with additional angle transformations

In this section, the controller that is used during the single phase open circuit measurements in Chapter 10 is introduced. An ordinary PI controller with feed forward of the back-EMF term and the cross coupling term in the rotating dq reference system is utilized and modified in order to work during a single phase open circuit fault. As a consequence, the zero sequence component of the current will be oscillating, as with the resonant controller. This simplified controller, which is inspired by the work presented in [17], is fully mathematically valid for a machine without rotor saliency ($L_d = L_q$) and with zero mutual coupling between the phases only. Despite that, it is successfully implemented and

used together with the experimental IPM machine in the lab.

Starting from (2.7) and (2.8), and considering $L_s = L_d = L_q$, the voltage in the dq reference frame can be described as

$$u_{dq} = R_s i_{dq} + L_s \frac{d i_{dq}}{d t} + j\omega L_s i_{dq} + j\omega \Psi_m \tag{2.32}$$

by adding feed forward compensation of the back-EMF term, $j\omega\Psi_m$, and the cross coupling term, $j\omega L_s i_{dq}$, the relation between voltage and current can be rewritten as

$$u'_{dq} = R_s i_{dq} + L_s \frac{d i_{dq}}{d t} \tag{2.33}$$

which gives the following Laplace transfer function of the machine

$$\frac{i_{dq}}{u'_{dq}} = \frac{1}{R_s + sL_s} \tag{2.34}$$

that in turn is the system to be controlled by the PI controller in Figure 2.7, if perfect feed forward compensations are assumed.

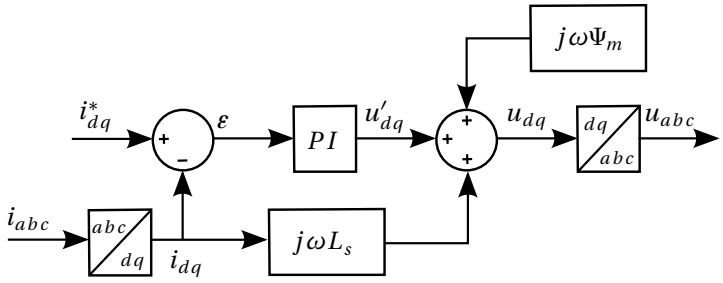

Figure 2.7: Ordinary PI controller implementation with feed forward of the back-EMF term and the cross coupling term in the rotating dq-reference system.

The target of the ordinary PI controller in Figure 2.7 is obviously to control the phase currents in order to get a current in the dq-plane, i_{dq}, according to its reference, i^*_{dq}. In order to better explain how the same thing can be accomplished when operating during a single phase open circuit fault, it is actually meaningful to visualize the individual phase currents in the dq-plane. The orientation

of each phase current is then shown with respect to its own back-EMF vector, or PM flux linkage vector $\boldsymbol{\Psi_m}$.

During normal operation and with current in the direction of the q-axis only, they are oriented as in Figure 2.8, where all the phase currents vectors are pointing in the direction of the positive q-axis (in phase with their respective back-EMF). For amplitude invariant scaling, the resulting $\boldsymbol{i_{dq}}$ current vector can be expressed as

$$\begin{aligned} \boldsymbol{i_{dq}} &= \boldsymbol{i_{adq}} = \boldsymbol{i_{bdq}} = \boldsymbol{i_{cdq}} = \\ &= (\boldsymbol{i_{adq}} + \boldsymbol{i_{bdq}} + \boldsymbol{i_{cdq}})/3 = j i_{adq} \end{aligned} \tag{2.35}$$

During phase open circuit fault operation, the current in the faulty phase, phase C, is interrupted while the currents in the two remaining phases are rearranged, as is illustrated by the current vectors in the dq-plane in Figure 2.9. These vectors correspond also to the currents that were presented in Figure 2.5 previously. The resulting $\boldsymbol{i_{dq}}$ current vector can be expressed as

$$\begin{aligned} \boldsymbol{i_{dq}} &= (\boldsymbol{i_{adq}} + \boldsymbol{i_{bdq}} + \boldsymbol{i_{cdq}})/3 = \\ &= (i_{ad} + j i_{aq} + i_{bd} + j i_{bq})/3 = \\ &= \frac{j 2 sin(\pi/3) i_{adq}}{3} = \frac{j i_{adq}}{\sqrt{3}} \end{aligned} \tag{2.36}$$

which is the same vector as in (2.35), but reduced by a factor $1/\sqrt{3}$ as mentioned earlier. However, the two dq phase current vectors, $\boldsymbol{i_{adq}}$ and $\boldsymbol{i_{bdq}}$, are not the same as the "global" dq current vector, $\boldsymbol{i_{dq}}$, and this must be compensated for in the controller. This is why the global dq current vector is multiplied by a factor $\sqrt{3}$ and shifted $+\pi/6$ or $-\pi/6$ for the two feed forward terms of the cross couplings in the new controller in Figure 2.10. The angle of the back-EMF term is not determined by the current angle, see (2.32), and it corresponds to the voltage that has to be applied to the machine terminals for zero current. The feed forward of the back-EMF term is therefore added directly to the two phase voltages, u_{adq} and u_{bdq}. In case of perfect feed forward compensations, the PI controller is controlling the current in an RL-circuit, (2.34), as was pointed out previously. In order to shift the currents in the two phase RL-circuits according to the vectors in Figure 2.9, the voltage from the PI controller, u'_{dq}, is shifted $+\pi/6$ or $-\pi/6$ for the two phase voltages.

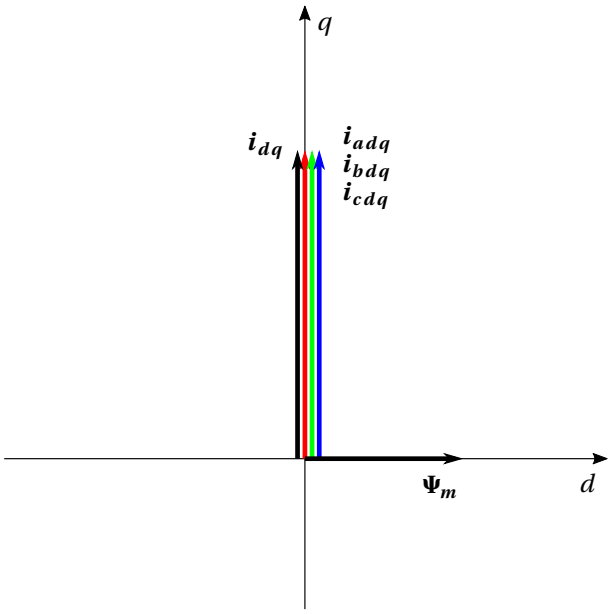

Figure 2.8: Vector representation of normal operation in the dq-plane.

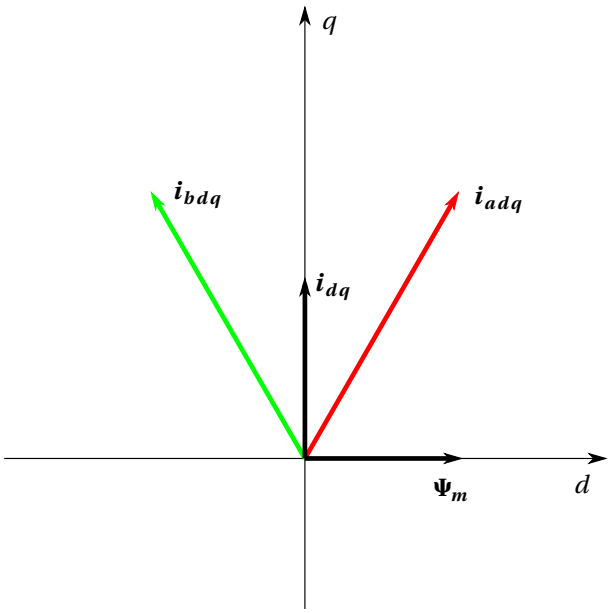

Figure 2.9: Vector representation of phase open circuit operation in the dq-plane.

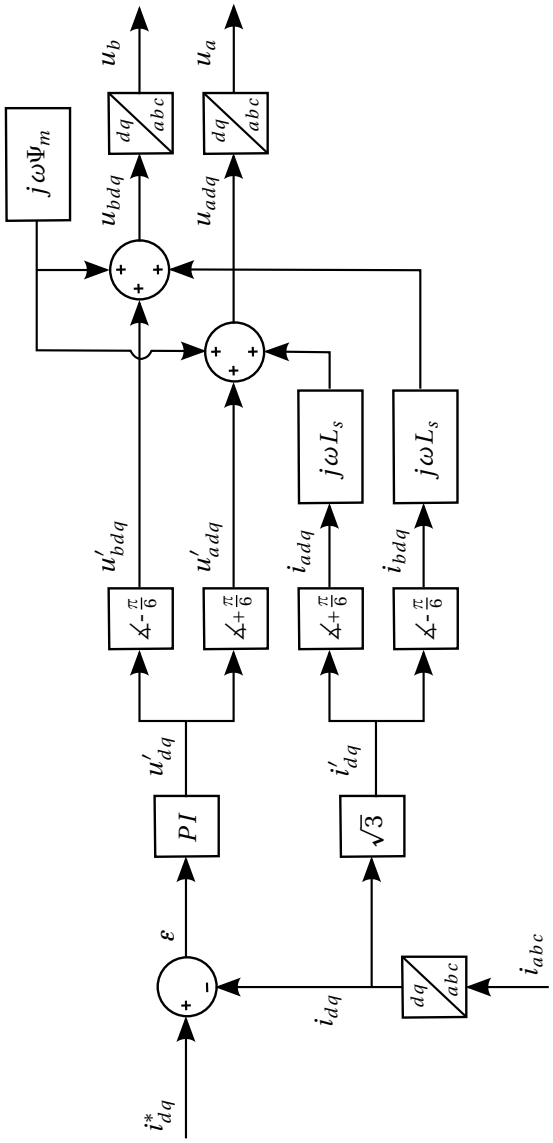

Figure 2.10: PI controller with additional angle transformations in the rotating dq reference frame.

Chapter 3

Per phase flux machine model

This chapter presents an alternative approach to model the PMSM during unbalanced conditions. The relatively low mutual coupling between the phases are simply neglected, it is thereby made relatively easy to take the individual saturation levels of the different phases into account. The difference between the flux levels of the phases might be remarkable when one phase is operated so that its flux is enhanced while another phase is operated so that the flux is weakened. A numerical method to calculate operating points when taking the individual saturation levels, during unbalanced conditions, into account are presented in the end of the chapter.

3.1 Flux representation in a single phase

The idea of the per phase flux machine model is to utilize the fact that the fault-tolerant machine is designed to get a very low or null mutual coupling between the phases. If the coupling between the phases is neglected, the flux in one phase is just a function of the rotor position and the current in the phase itself. If the flux and the torque in one phase is calculated as a function of the rotor position and the current, it is possible to utilize the same 2-dimensional flux and torque maps for all the three phases by including a phase shift of the rotor position. In the stationary reference frame, the phase voltage can be expressed as

$$v_{ph} = R_s i_{ph} + \frac{d\psi_{ph}}{dt} \tag{3.1}$$

where the phase flux derivative can be divided into two parts, one that is related to the phase current and one that is related to the rotor position

$$\frac{d\psi_{ph}}{dt} = \frac{\partial \psi_i}{\partial t} + \frac{\partial \psi_\theta}{\partial t} \tag{3.2}$$

or linearized and expressed by quantities that are to be found in the flux map

$$\frac{d\psi_{ph}}{dt} = \frac{\Delta \psi_i}{\Delta i}\frac{\partial i}{\partial t} + \frac{\Delta \psi_\theta}{\Delta \theta}\omega \tag{3.3}$$

The electrical equations, expressing the phase voltages of the three phase PMSM can be written on the same form as in (2.1), previously presented in Section 2.1. For a low or null mutual inductance three phase machine, the inductance matrix can be rewritten as

$$\boldsymbol{L} = \begin{bmatrix} \frac{\Delta \psi_i}{\Delta i}(i_a, \theta) & 0 & 0 \\ 0 & \frac{\Delta \psi_i}{\Delta i}(i_b, \theta - \frac{2\pi}{3}) & 0 \\ 0 & 0 & \frac{\Delta \psi_i}{\Delta i}(i_c, \theta + \frac{2\pi}{3}) \end{bmatrix} \tag{3.4}$$

where the mutual coupling between the phases are put to zero. The back EMF terms in (2.2) are reformulated as

$$\begin{bmatrix} e_a \\ e_b \\ e_c \end{bmatrix} = \begin{bmatrix} \frac{\Delta \psi_\theta}{\Delta \theta}(i_a, \theta) \\ \frac{\Delta \psi_\theta}{\Delta \theta}(i_b, \theta - \frac{2\pi}{3}) \\ \frac{\Delta \psi_\theta}{\Delta \theta}(i_c, \theta + \frac{2\pi}{3}) \end{bmatrix} \omega \tag{3.5}$$

where the individual saturation levels of the three phases during unbalanced operation will be taken into account. The instantaneous electrodynamic torque that is produced by the three phases can be calculated as

$$T_e = T(i_a, \theta) + T(i_b, \theta - \frac{2\pi}{3}) + T(i_c, \theta + \frac{2\pi}{3}) \tag{3.6}$$

where the same 2-dimensional torque map is utilized for all the three phases.

3.1.1 Per phase flux and torque maps

A great number of magnetostatic simulations were carried out, where phase A was excited in the range -360 A to +360 A while the rotor was rotated one full electrical period. In this section, the rotor angle refer to the electrical angle of phase A and zero degrees corresponds to the angle of the positive peak of the flux linkage of the PMs in phase A (positive d-axis).

The total flux-linkage, both the induced and due to the PMs, in phase A as function of rotor position and current excitation can be seen in Figure 3.1. One can observe that the current excitation is quite generous as the flux is relatively flat along the whole period of rotor positions at the highest current levels.

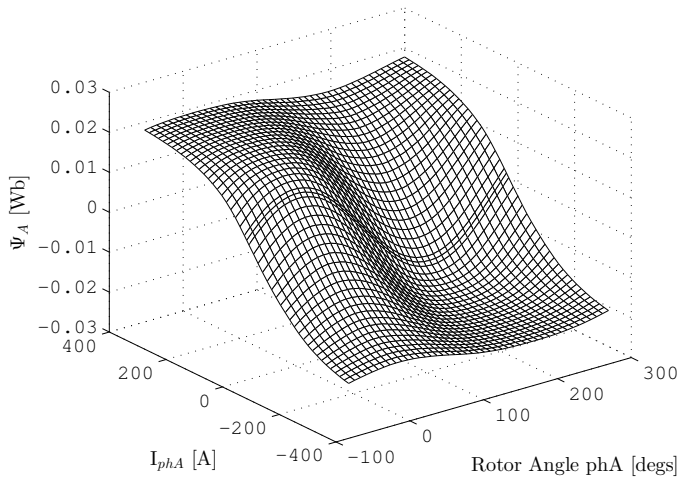

Figure 3.1: Flux-linkage in phase A as function of rotor position and phase current.

The total flux-linkage in phase C, due to the PMs and the current in phase A, is shown in the same manner in Figure 3.2. It is hard to note any difference in flux-linkage along the excitation axis, which confirms that the magnetic coupling between the phases are low.

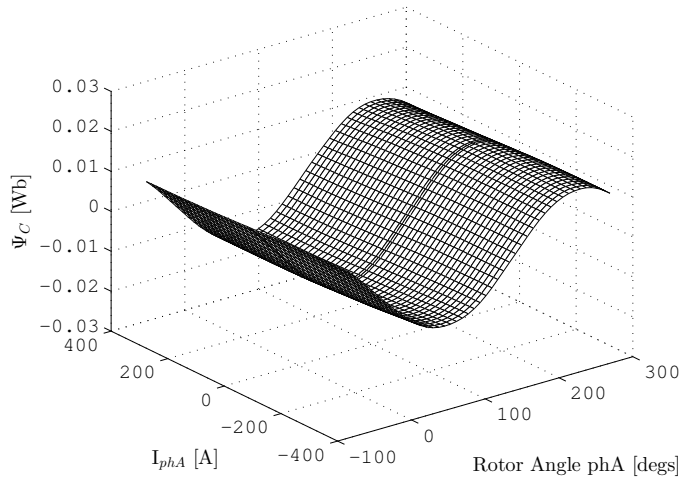

Figure 3.2: Flux-linkage in phase C as function of rotor position of phase A and current in phase A.

Figure 3.3 shows the flux-linkage in phase A when the flux-linkage at zero current is subtracted. When studying the change in flux-linkage it is clear that it is a function of rotor position and that it's not a linear function of the current. The linear region can be seen as a band that is phase shifted 180 degrees with respect to the flux-linkage of the PMs. At zero degrees, where the PM flux is at its peak, the linear band is at its minimum along the rotor angle axis.

In Figure 3.4, the flux-linkage in phase C at zero current is subtracted at each excitation level to show how much the flux-linkage in phase C is affected by the excitation of phase A. The flux-linkage is shown in the same scale as in the previous figures. When comparing Figure 3.4 and Figure 3.3, it can be observed that the change of flux linkage in the neighboring phases, B or C, due to the excitation of phase A is relatively low.

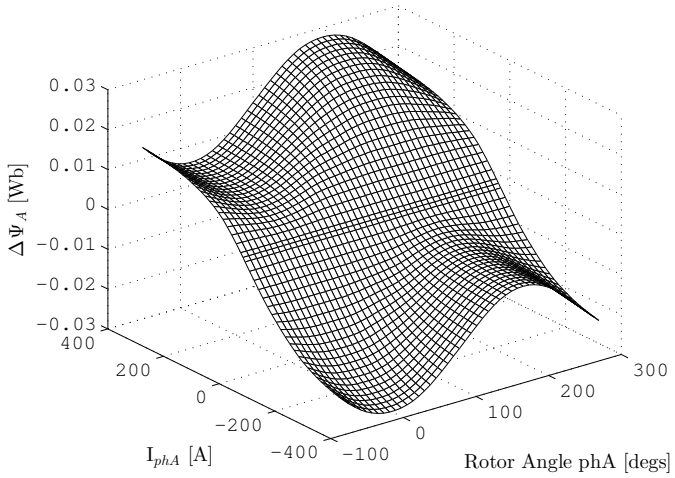

Figure 3.3: The change of flux-linkage in phase A due to the current in phase A.

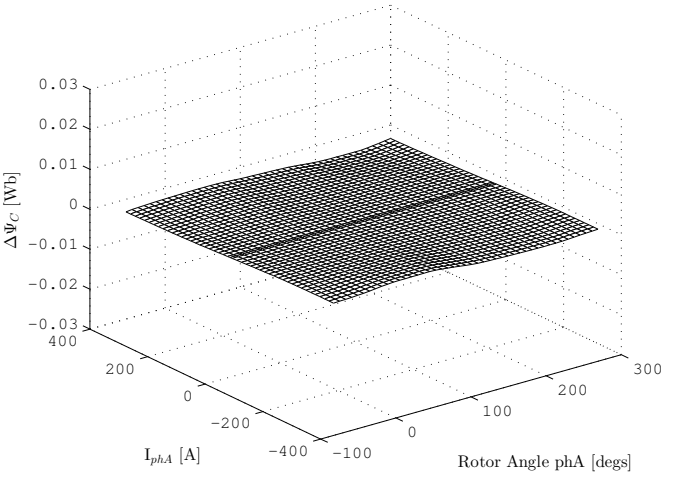

Figure 3.4: The change of flux-linkage in phase C due to the current in phase A.

Figure 3.5 shows the ratio between the change of flux-linkage in phase C and the change of flux-linkage in phase A, $|\Delta\Psi_C/\Delta\Psi_A|$ in percent, due to the current in phase A. If the the change in flux-linkage in phase A is assumed to be the total induced flux, between 2.8% and 8.6% of the total induced flux in phase A links the neighboring phases when they are unexcited. The average over the whole map, excluding the points of zero excitation, is 4.6%.

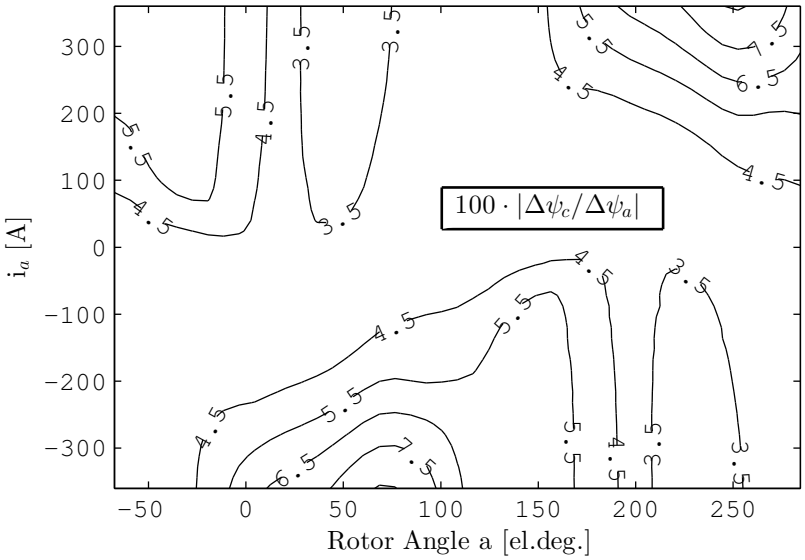

Figure 3.5: The ratio between the change in flux-linkage in phase C and the change in flux-linkage in phase A, $|\Delta\Psi_C/\Delta\Psi_A|$ in percent.

In Figure 3.6, the torque produced by a single phase as a function of its rotor position and current is shown. Excluding the highest current levels, the peak torque occur at exactly 90 electrical degrees, thus when the current is in the q-direction.

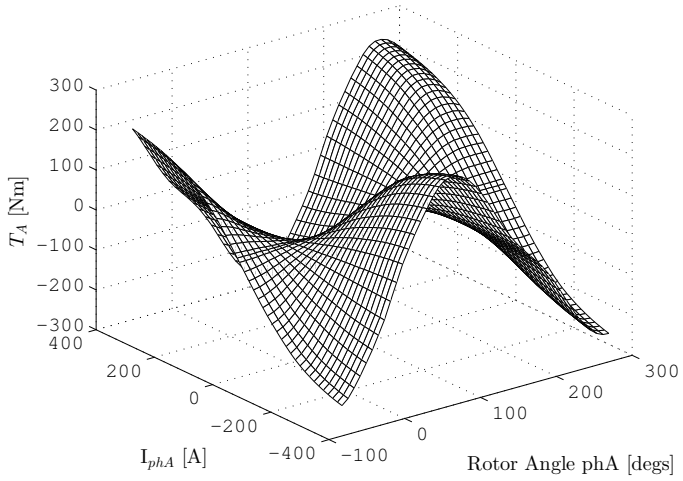

Figure 3.6: Torque production as function of rotor angle and current in phase A.

3.2 Numerical solution of 2-phase MTPA operation

In this section, it is shown that the machine model easily can be used to adjust the phase currents in order to compensate for the torque ripple introduced by the asymmetric saturation. This can be done in a manner, similar to the maximum torque per ampere (MTPA) in the dq-reference frame, where the torque reference is used to find a set of i_d and i_q combinations and the combination that minimizes $\sqrt{i_d^2 + i_q^2}$ is chosen [34]. From (3.6) it is possible to find a set of i_a and i_b combinations at each rotor position, θ, based on the torque reference. At each rotor position, the combination that minimizes $\sqrt{i_a^2 + i_b^2}$ is chosen to cover a full electrical period.

The implemented numerical method that is used to find solutions of the 2-phase MTPA operating points is illustrated in flow chart form in Figure 3.7. The Torque reference, T^*, is just a DC-value in case of a phase open circuit fault, as the open circuited phase doesn't produce any torque. In case of a short circuit fault, an oscillating torque reference that compensates for the torque production of the short circuited phase can be used.

The first block sorts out the combinations of phase currents, i_a and i_b, that fulfills the torque reference, $T^* \pm \Delta T^*$, according to the torque map. The combinations that minimizes $\sqrt{i_a^2 + i_b^2}$ is chosen over an electrical period. The i_a and i_b waveforms are low pass filtered using discrete Fourier transform (DFT) in order to remove unrealistically high current harmonics. The RMS values of the

filtered currents are calculated and compared with the maximum RMS current. If the RMS values of the calculated currents are too high, the torque reference is reduced until the current limitation criteria is fulfilled.

The phase voltages are calculated using the flux map and the currents. Another DFT is applied to the voltages to remove the higher order harmonics introduced by the discretized flux map. The peak-values of the phase voltages are compared with the maximum phase voltage. If the phase voltages are to high, the torque reference is reduced until both the current limitation criteria and the voltage limitation criteria are fulfilled.

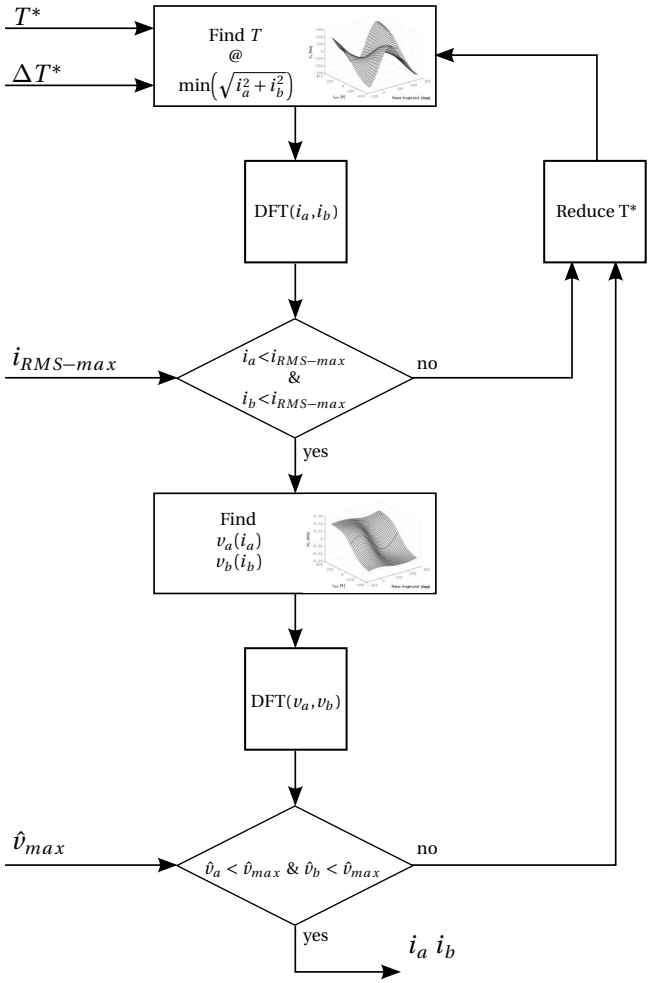

Figure 3.7: Illustration of the process that has been used find the numerical solution to the 2-phase MTPA operating point.

Chapter 4

Design of fault-tolerant fractional slot machines

Chapter 4 describes how the theory in Chapter 1 has been implemented when the factional slot machines are designed. The chapter starts with an introduction of the design specification, that is based on the Toyota Prius Machine from 2004. A choice of pole/slot configurations is presented, while the final analysis of the designs are made in Chapter 5.

4.1 Design specification

The design specification has been chosen based on the physical dimensions of the Toyota Prius Machine from 2004, in order to design a fractional slot machine of similar physical size including the active parts. The Prius 2004 machine has been used as a reference as it has been investigated intensively and a lot of reference material is currently available. The end-windings are expected to be shorter for a fractional slot machine with concentrated windings compared to a machine with distributed windings. It has been assumed that the stator stack length can be extended by approximately 30%. In fact, the protrusion of the end-windings varies depending on many things; slot geometry, copper wires, manufacturing process etc. An interesting study, where the size of the end-windings are compared when the same stator is wound with; distributed windings, one-layer concentrated winding and two-layer concentrated winding is presented by [35]. More about estimation of the end-windings of the final designs can be found in Section 5.2.1. Some key parameters of the 2004 Prius are presented together with the design specification of the thesis design in Table 4.1.

Table 4.1: 2004 Prius [36] and Thesis design characteristics.

	Prius 2004	**Thesis design**
Outer stator diameter [mm]	269	269
Stator stack length [mm]	84	108 [1]
Rotor diameter [mm]	160.5	-
Cu [kg]	6.8	-
PM [kg]	1.232	-
Peak power [kW]	50	-
Peak torque [Nm]	400	-
Max speed [rpm]	6000	6000

4.1.1 Rating of the reference machine

The rating of an electric machine itself due to its own physical limitations, without taking inverter rating and the DC-link voltage etc. into account, are often determined by a thermal limit together with limitations of the mechanical structure and the electrical insulation. The different types of limitations are not independent as material properties varies with temperature and insulation material might be sensitive to both high temperatures and vibrations. If the electrical machine is used in a vehicle, it is likely that the machine is just one component among others that utilize the same cooling system. If that is the case, not even the thermal limit of the electric machine is a strictly independent property of the machine itself. Therefore, it is impossible to to make a meaningful comparison between two electric machines without introducing boundaries or restrictions.

In this thesis, the boundaries are based on the Toyota Prius 2004 "similar" drive system, which is tried to emulate the real drive system of the Toyota Prius 2004 as good as possible with the available data that is found. A model of the Prius 2004 machine following [37] (using the same geometry and material data) has been used and the result from the FEA is compared with the measurement results in [38]. It is worth mentioning, that tests that are presented in [39] show that the thermal limited continuous power ratings of the machine are approximately 21kW with $35^o C$ coolant and 15kW with $105^o C$ coolant, while the manufacturer specifies the continuous power rating of the machine to 30kW.

According to [38], a phase current of 250 A_{RMS} is needed to reach the specified peak-torque of 400Nm. The DC-link voltage can be boosted up to 500V. From that it follows that the maximum phase voltage is $500\sqrt{2}/\pi = 225 V_{RMS}$ in three phase square wave modulation mode, which is one of the modulation techniques that is used in the 2004 Prius drive system [38]. This means that the

[1] Based on the assumption that the expected shorter end-windings will allow for an increased active length of 30%.

inverter must be rated at least to $3 \cdot 250 \cdot 225 = 169$kVA. The FEA result given for the kVA limitation is shown in Figure 4.1. The machine is operated at the MTPA point that fulfills the kVA limit at each speed. The output torque at 250 A_{RMS} from the FEA is 374 Nm which is about 6.5% lower than the reported torque for the same current. One can observe that the voltage limit is reached at about 2250 rpm, while the peak torque of the electrical machine is achieved up to 1200 rpm in the Prius 2004 drive system [38]. It is clear that the torque is limited before the voltage limit is reached, also discussed in [38].

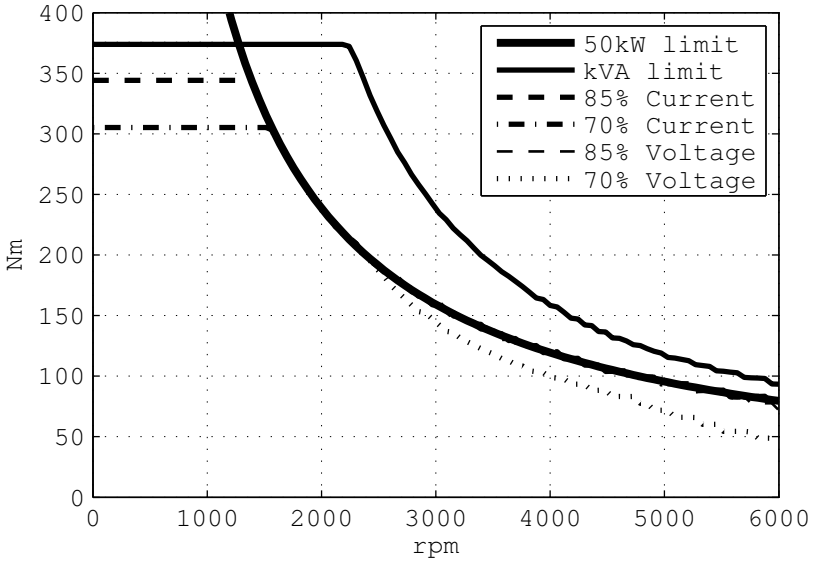

Figure 4.1: Torque speed characteristics of the Toyota Prius 2004 machine that is used as a reference.

Another limit is the supply of active power to the DC-link, which can be fed from the battery via the DC/DC-converter ($\approx 20kW$) and from the generator via the generator converter ($\approx 30kW$). In total, the active power is then limited to about 50kW, which is also plotted in Figure 4.1. Considering the power limitation and the FEA torque, the peak torque is achieved up to 1270 rpm which is 5.8% higher than specified in [38]. The torque as function of speed is estimated based on approximate data provided by the Toyota Motor Company and presented in [38]. The overall picture is very similar to the power limit curve in Figure 4.1. According to [38], the torque at 6000 rpm is estimated to 60-70 Nm and the FEA model shows about 75 Nm at the same speed.

In addition to the active power and kVA limit of the converter found, the sensitivity of the relatively high kVA limit was studied and presented in Figure 4.1. The voltage and current limits of the converter were reduced in two steps respectively (to 85% and to 70%). The effect of the current reduction (voltage at 100%) can be seen in the low speed region only, the torque is reduced and the speed limit of the peak torque is increased as a direct consequence of the power limit. The torque output is not affected when the current is put back to 100% and the voltage reduced to 85%, as the torque is still limited by the active power and not the voltage. If the voltage is reduced to 70%, the torque is voltage limited from approximately 2500 rpm, while it is power limited in the range 1270-2500 rpm and current limited in the range 0-1270 rpm.

It should be noted that a set of i_d and i_q combinations exists for each speed and torque level, where the shortest current vector corresponds to the MTPA operating point. When the voltage was reduced to 85%, it is still possible that a subset of i_d and i_q combinations including the original MTPA operating point is disqualified due to voltage limitation and a new MTPA operating point that fulfills the voltage limitation is found. This can not be seen in the torque speed diagram in Figure 4.1, as the same torque level is maintained. This is an interesting aspect when it comes to turn selections of the machines. It might be possible to choose a high number of turns without limitation of the torque at higher speeds as it is limited by active power rather than voltage. On the other hand, it is possible that a higher number of turns will results in an increased transfer of reactive power between the converter and the machine as the power factor is affected.

4.2 Selection of pole and slot combination

Some feasible pole and slot combinations were previously shown in Table 1.1, where both $Q_s = 2p \pm 1$ and $Q_s = 2p \pm 2$ combinations were presented. The $Q_s = 2p \pm 1$ combinations results in an odd number of slots and teeth per phase which is not regarded as a suitable choice for a fault tolerant machine, as the sum of the induced flux per phase cannot be zero. For all the $Q_s = 2p \pm 1$ combinations, the flux from one phase must link to another phase and it will result in a considerable mutual inductance between the phases.

Remaining are the $Q_s = 2p \pm 2$ combinations, which result in an even number of teeth per phase and possibly a very low mutual coupling between phases depending on the winding configuration. Back-EMF phasor diagrams for $Q_s = 2p \pm 2$ combinations from $p = 5$ to $p = 13$ are shown in Table 4.2. It can be seen that machines with the same number of slots, Q_s, will result in the same winding configuration as the phasor diagrams are just mirrored.

Table 4.2: Back-EMF phasor diagrams.

12/5 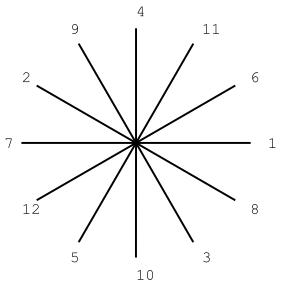	12/7 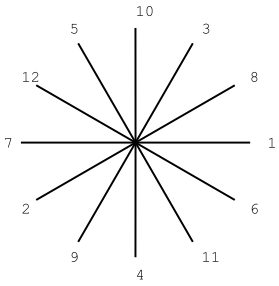
18/8 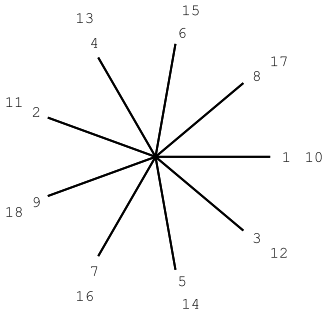	18/10 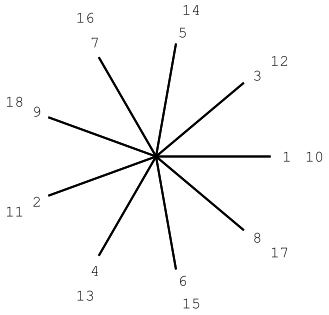
24/11 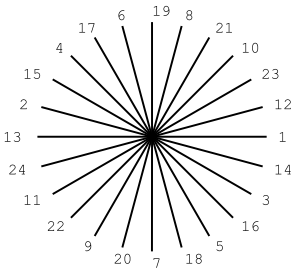	24/13 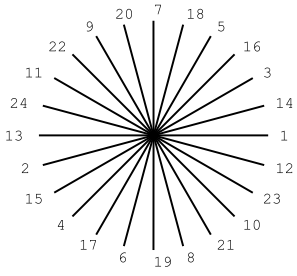

Models of the resulting three stator configurations that might be of interest are created in FEA models and are shown in Figure 4.2. No permanent magnets are introduced, the rotors are just solid iron cores, and the stators are excited according to their respective winding configuration. The grey or shadowed areas

represents the teeth of one phase in each stator configuration. It can be seen that groups of an even number of teeth, 2 and 4, appear for the 12/5 and 24/11 configurations while the 18/8 configuration shows groups of an odd number, 3. One can conclude that the phases of the 18/8 configuration are harder magnetically coupled than for the other two configurations. The local sum of the flux from an odd group of teeth cannot be zero, thus more flux lines from the grey teeth link the neighboring teeth, see Figure 4.2. Therefore, only the $Q_s = 12$ and $Q_s = 24$ are finally regarded as interesting choices.

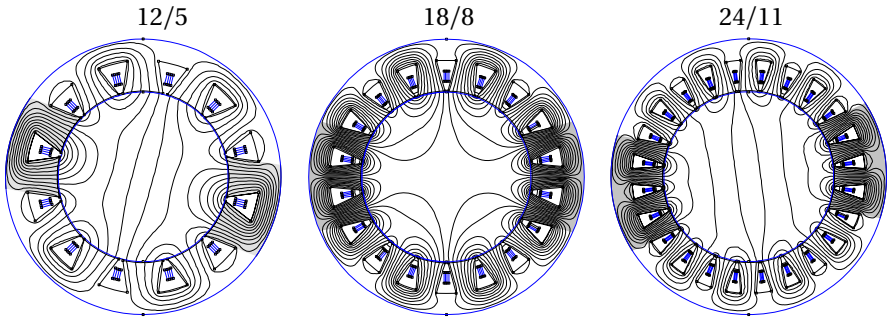

Figure 4.2: Flux lines representing induced flux for three different pole slot combinations.

Both the $Q_s = 12$ and $Q_s = 24$ give slot and pole combinations that fulfill the two "null mutual inductance requirements"

$$2p = Q \pm 2t \tag{4.1}$$

and

$$Q/(2t) \text{ even} \tag{4.2}$$

pointed out in [40], where design considerations on fractional-slot fault-tolerant synchronous motors are presented. The requirement (4.2) is not fulfilled for $Q_s = 18$ due to the groups of an odd number of teeth, see [40].

Another interesting aspect when studying Figure 4.2, is that the lowest possible MMF subharmonic with a wave length that equals 2π mechanical rad can be seen. It causes the flux lines that crosses straight through the rotor and is present in the $Q_s = 12$ and $Q_s = 24$ but not in the $Q_s = 18$ stator configuration.

The MMF harmonics of the 12/5 and 12/7 configurations have already been used as an example in section 1.6 and are presented in Figure 1.6. It is clear that the 12/5 arrangement provides a more advantageous MMF harmonics pattern in relation to the fundamental. The two pole configurations are compared when used in an axial flux machine configuration in [41]. In that case the rotor

losses for the $p = 7$ is about twice compared to the $p = 5$. Their winding factors are the same and $p = 5$ is therefore considered for the $Q_s = 12$ configuration.

When it comes to the 24/11 and 24/13 configurations, it can be seen in Figure 4.3 that the 24/11 arrangements gives a somewhat lower harmonic content in the MMF wave.

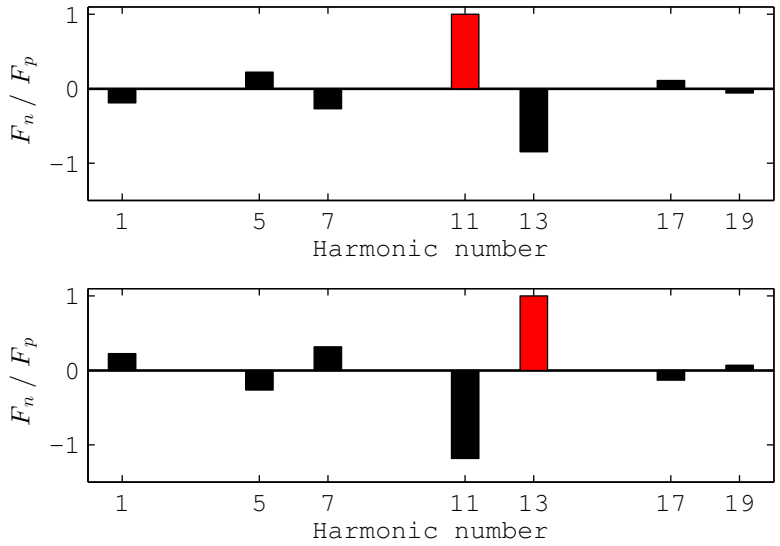

Figure 4.3: Harmonic content in the air-gap for the $p = 11$ and $p = 13$ machine respectively. The amplitudes are related to the fundamentals which corresponds to the red bars.

The relative frequency of the MMF harmonics on the rotor side are shown in Figure 4.4. It can be seen that the relative frequency of the fundamental component is zero in both configurations and that the relative frequency of the 5th and 7th harmonics is shifted somehow, in a similar way as the 17th and 19th. As the winding factors are the same for both pole numbers but the pole numbers are relatively high, the $p = 11$ is considered for the $Q_s = 24$ configuration.

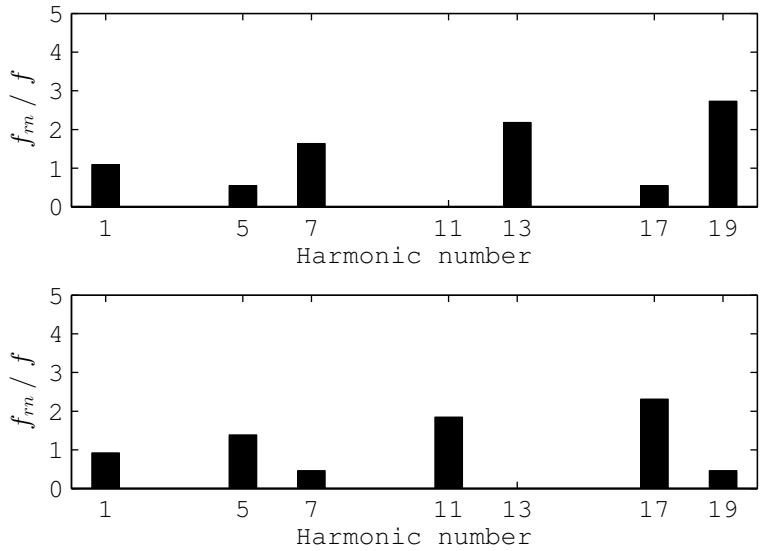

Figure 4.4: Relative frequency of the MMF harmonics on the rotor side. The frequency of the fundamental $n = p = 11$ and $n = p = 13$ equals zero for both configurations.

It is difficult to motivate a choice of just one of the remaining configurations. One could argue that the number of poles $p = 11$ is too high and thereby limit the electrical/mechanical frequency and as a consequence also the output power. On the other hand, the 24/11 offers both lower MMF harmonic content and a slightly higher winding factor. Lowered MMF harmonic content is expected to reduce the rotor and PM losses. If the frequency of the 12/5 configuration is limited by the losses caused by MMF wave harmonics rather than the frequency of the fundamental, the 24/11 might be a better choice. Another aspect is that the stator yoke becomes rather bulky when the rotor diameter, hence the total magnetic flux from a permanent magnet, is increased later shown in (4.5) in Section 4.4.3. It is therefore possible that a higher pole number suits the decided design specification better. In the end, it is the combined weight of torque and speed characteristics of the two machines that can motivate a final choice. The 24/11 is expected to give a higher torque output than the 12/5 at lower frequencies, but it is not obvious that the 12/5 can operate at higher frequencies than the 24/11 due to the complex nature of the losses caused by the MMF harmonics.

4.3 FEA and material data

This section presents how the FEA is carried out and the material data that is used during the design of the fault-tolerant machines and when modeling the Prius 2004 reference machine. The same methodology but different material data are used for the experimental machine that is introduced in Chapter 7.

4.3.1 Finite Element Analysis

The electromagnetic part of the finite element analysis has been carried out in ANSYS Maxwell, while the thermal part of the finite element analysis has been carried out in femm. Except for Figure 4.2 that is produced for illustrative purpose only, in femm. All models are created based on 2D geometries, where the electromagnetic part is carried out in static as well as in transient modeling mode. The thermal modeling is made only in static mode and rather simplified models has been used.

4.3.2 Material data

Copper

In the FEA, the current is modeled to be uniform through the 2D winding object. The current density in the winding object has been scaled according to the fill-factor and the slot area. The fill-factor is defined as the ratio between the total cross-sectional area of the copper that occupies the slot area and the slot area itself, the insulation is not included. The definition that has been used for slot area, A_{slot}, can be seen in Figure 4.5. A copper fill-factor of 0.5 has been assumed for all the fractional slot machine designs. The electric copper resistivity is put to $2.39 \cdot 10^{-8} \Omega m$ corresponding to a temperature of 120^oC. The thermal conductivity of copper has been put to 400 $W/(m \cdot K)$ but an equivalent thermal conductivity for copper and impregnation material, called winding mix, are used when modeling slots. The thermal conductivity of the winding mix has been varied and the values that are used are presented together with the results.

Iron

A non-linear model of the lamination material as presented in [37], have been used for all the machine designs. A thermal conductivity of 28 $W/(m \cdot K)$ has been used along the lamination sheets.

Permanent magnets

A model based on the residual flux density, B_r, the relative permeability, μ_r, and the electric conductivity, σ, of the PMs has been used in the FEA. Data for two different permanent magnets, PM1 and PM2, are specified in Table 4.3. PM2 is

used in the FEA of the Prius 2004 reference machine and the data are given in [37]. PM1 was chosen for the thesis designs due to its lower electric conductivity and the expected eddy current loss in the PMs of a fractional slot machine. There are actually several PM material with the lower conductivity and similar characteristics available at [42], but the choice was made to reflect N30AHZ due to its high maximum recommended working temperature of $220^o C$.

Table 4.3: Material properties of the two different permanent magnet materials that are used.

Parameter	**PM1**	**PM2**
$B_r[T]$	1.1	1.19
μ_r	1.04	1.03
$\sigma[S/m]$	$5.56 \cdot 10^5$	$6.25 \cdot 10^5$

4.4 Design strategy

The design strategy is to vary a number of parameters for both the selected configurations, Q_s=12/p=5 and Q_s=24/p=11. Then, to use FEA to evaluate the designs and to find the most promising candidates of each configuration, within the interval of the chosen parameters. About ten variables here called "geometry parameters", excluding information about the windings, are needed to geometrically define the machine designs and they are presented in Section 4.4.3. Instead of just sweeping all the geometry variables, four "design variables" were defined. The aim of introducing the four design variables is to reduce the number of design combinations and thereby limit the computational time, but also to use a limited set of variables that simplify the interpretation of the results.

4.4.1 Design variables

In this section a short explanation follows of the ideas behind the four design variables. The ranges within each design variable, are also presented.

Rotor diameter, D_r

The rotor diameter is considered as one of the most important variables. For a fixed active length, it determines the cross-sectional area of the air-gap as well as at which radius the air-gap is located. Both these properties of the air-gap are extremely important for the torque production which takes place in the air-gap. For a fixed outer stator diameter, it defines also the ratio between the stator and the rotor volume. From that perspective, it determines also the possible proportions between electric and magnetic loading for a PMSM to some extent. The rotor diameter is chosen to be varied in 10 mm steps between 150 mm and 200 mm.

Air-gap length, l_g

Another important variable is the air-gap length, which determines the magnetic coupling between the stator and the rotor. A shorter air-gap length lowers the reluctance of the gap and increases the flux for a fixed permanent magnet length or induced MMF-wave. This may imply that the amount of permanent magnets and copper can be reduced. On the other hand, apart from possible mechanical issues associated with narrow air-gaps, it gives also a more non-linear machine. The total reluctance of the magnetic circuit will be more sensitive to the non-linear reluctance of the iron path, which is relatively more significant when compared to a low air-gap reluctance. Air-gap lengths of 0.8 mm and 1.2 mm have been used.

Stator flux density, B_{max}

The flux density level is an important aspect, why a stator flux density variable, B_{max}, is defined. B_{max} is the maximal average permanent magnet flux density over the cross-sectional area along a flux path. The aim is to design a stator structure with a constant flux density along the flux path following the philosophy presented in Section 1.3. Parts where the flux path is well defined, such as the yoke, can be calculated easily while parts where the flux path is not well defined, such as the shoe of the teeth, is not that straightforward. One lighter and one heavier stator structure is designed, corresponding to stator flux levels of 1.5 T and 1.3 T respectively. As two flux levels for the same magnetic loading is used, the combination of PM and induced flux is altered which was discussed in Section 1.1.

Air-gap flux density, $\hat{B}_1$

Air-gap flux density, $\hat{B}_1$, corresponds directly to the magnetic loading and is not expected to require any further explanation. Peak flux densities of 0.85 T and 1 T are used.

4.4.2 Design variable combinations

The sets of the design variables presented in the previous section result in 48 different combinations. Each combination result in a machine design that is labeled with a number and collected in Table 4.4.

Table 4.4: Design variable combinations and their corresponding machine design index.

#	D_r	l_g	B_{max}	$\hat{B}_1$
1	150	0.8	1.3	0.85
2	150	0.8	1.3	1
3	150	0.8	1.5	0.85
4	150	0.8	1.5	1
5	150	1.2	1.3	0.85
6	150	1.2	1.3	1
7	150	1.2	1.5	0.85
8	150	1.2	1.5	1
9	160	0.8	1.3	0.85
10	160	0.8	1.3	1
11	160	0.8	1.5	0.85
12	160	0.8	1.5	1
13	160	1.2	1.3	0.85
14	160	1.2	1.3	1
15	160	1.2	1.5	0.85
16	160	1.2	1.5	1
17	170	0.8	1.3	0.85
18	170	0.8	1.3	1
19	170	0.8	1.5	0.85
20	170	0.8	1.5	1
21	170	1.2	1.3	0.85
22	170	1.2	1.3	1
23	170	1.2	1.5	0.85
24	170	1.2	1.5	1

#	D_r	l_g	B_{max}	$\hat{B}_1$
25	180	0.8	1.3	0.85
26	180	0.8	1.3	1
27	180	0.8	1.5	0.85
28	180	0.8	1.5	1
29	180	1.2	1.3	0.85
30	180	1.2	1.3	1
31	180	1.2	1.5	0.85
32	180	1.2	1.5	1
33	190	0.8	1.3	0.85
34	190	0.8	1.3	1
35	190	0.8	1.5	0.85
36	190	0.8	1.5	1
37	190	1.2	1.3	0.85
38	190	1.2	1.3	1
39	190	1.2	1.5	0.85
40	190	1.2	1.5	1
41	200	0.8	1.3	0.85
42	200	0.8	1.3	1
43	200	0.8	1.5	0.85
44	200	0.8	1.5	1
45	200	1.2	1.3	0.85
46	200	1.2	1.3	1
47	200	1.2	1.5	0.85
48	200	1.2	1.5	1

4.4.3 From design variables to geometry parameters

Besides the rotor diameter, D_r, and the outer stator diameter, D_{out}, eight more parameters are needed to define the complete 2D machine geometry, see Figure 4.5. Six of the parameters are calculated and updated for each design variable configuration while five are held fixed.

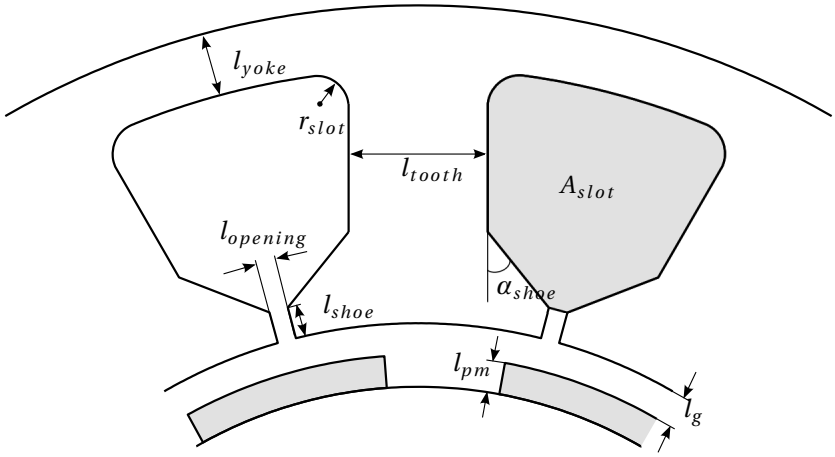

Figure 4.5: The eight geometry parameters that together with the rotor diameter, D_r, and the outer stator diameter, D_{out}, define the 2D machine geometry. The grey area in the right hand slot defines the slot area, A_{slot}, that is used when the fill-factor is calculated.

Permanent magnet length

The permanent magnet length, l_{pm}, is calculated based on the air-gap length, l_g, and the desired air-gap flux density, $\hat{B}_1$, using (1.4) and (1.5) in Section 1.2. The calculated permanent magnet lengths that are required for the four combinations of l_g and $\hat{B}_1$ are shown in Table 4.5.

Table 4.5: Required permanent magnet length, l_{pm}, in mm.

		Air gap length, $l_g[mm]$	
		0.8	**1.2**
$\hat{B}_1[T]$	**0.85**	1.9	2.8
	1	3.8	5.6

The permanent magnet length is varied within a great interval, it is likely that the shortest permanent magnet length of 1.9 mm will cause manufacturing issues. This has not been investigated further since it is not used in the final designs.

Stator yoke and teeth

The total flux from a permanent magnet can be calculated approximately by integrating the square shaped flux, B_m, in Figure 1.3. For a permanent magnet that covers 2/3 of a pole pitch it becomes

$$\phi_m = B_m \frac{\pi(D_r + 2l_{pm})2/3}{2p} \tag{4.3}$$

which is the maximum magnetic flux that links a tooth. The required thickness of the tooth, l_{tooth}, for a given stator flux density, B_{max}, is then calculated according to

$$l_{tooth} = \frac{\phi_m}{B_{max}} \tag{4.4}$$

When the PM flux that links a tooth enter the yoke region it divides about equal between the two paths that links the two neighboring teeth. Hence, the required thickness of the stator yoke for the same flux density is calculated as

$$l_{yoke} = \frac{\phi_m}{2B_{max}} \tag{4.5}$$

Fixed parameters

The fixed parameters and the values used can be seen in Table 7.2. The assumed values used for the parameters that have been held fixed is based on discussions and what is commonly used in existing machines. Values are therefore open for modifications if the machines are to be prototyped.

Table 4.6: Geometry parameters that are not affected by the design variables and held fixed.

Parameter	**value**
D_{out}	269 mm
r_{slot}	5 mm
l_{shoe}	2 mm
α_{shoe}	45°
$l_{opening}$	3 mm

Chapter 5

Analysis of fault-tolerant fractional slot machine designs

In this chapter, the 48 design variable combinations of each pole/slot combination are evaluated in order to motivate a choice from each set of combinations. An appropriate number of turns are selected for the windings of the machines and the impact of phase current on winding temperature rise is analyzed. The two final machine designs are compared together with the Toyota Prius from 2004 in terms of performance and material cost. Some key figures from the comparison of the three machines are summarized in the end of this chapter.

5.1 Machine design selection

The 48 machines are evaluated by comparing their torque production in relation to the material cost, [Nm/USD]. The material market price have fluctuated substantially over the last years, especially for neodymium which today is back on the same price levels as in 2010 (≈100 USD/kg) from the peak during 2011 (≈500 USD/kg). Due to the variation of the material cost, the current material cost is estimated and the results are presented to take cost variation of each material into account.

5.1.1 Estimation of the current material costs

Accurate calculations of the material costs is a difficult or even impossible task, since the material prices varies substantially over time as mentioned previously. Also the price at two different markets may not be the same at the same time. The estimations presented in this section are based on information collected in

the beginning of August in 2014. The current material cost estimation is presented in Table 5.1.

Table 5.1: Current material cost estimation.

Material	Cost [USD/kg]	Cost [SEK/kg]
Copper	7.1	49
Iron	2.1	14.4
PM	82.3	566

Copper

The material cost of copper that is used in this thesis, is an average of the three month average prices at London Metal Exchange (LME) and Commodity Exchange (COMEX) respectively.

Table 5.2: Three month average copper price presented at [43].

3 Month average price [USD/kg]	
LME	7.0960
COMEX	7.1650
Average	**7.1**

Iron

The material cost of the iron varies depending on the alloy content. Silicone steel had been rather stable at around 2.1 USD/kg the last three month, when data was collected in August 2014 [44].

Permanent magnets

Typical rare earth element content in neodymium magnets together with the chinese export prices are shown in Table 5.3. The values of the typical element content are 2-3 years old and it is possible that they are slightly lower today. There is at least an incentive to strive to lower them due to their relatively high price. The metal prices presented at [44] have been recalculated manually to a corresponding three month average.

Table 5.3: Rare earth element content in Neodymium magnets together with the chinese export prices.

Element	Typical weight	USD/kg
Neodymium	31% [45]	92.5 [44]
Dysprosium	8.5-11% [46]	550 [44]
Magnet	**31% and 9.75 %**	**82.3**

5.1.2 Torque per cost for different cost scenarios

It was concluded at an early stage that the Prius 2004 reference machine offers a quite high peak torque, why it was natural to sort out promising designs based on torque production. An aspect on torque production is that basically any PMSM produces higher torque if more permanent magnets are added to the rotor or if the machine is made larger. When the physical size or volume of the machine is used as a boundary for the design, an increase of one material or part will automatically lead to a decrease of another material or part. An important aspect is the balance between materials and parts, one want to know if it is more effective to add 100g of PM material to increase the magnetic loading than adding 100g of copper to increase the electric loading. Maybe even more interesting to see if 2 USD of PM material pays back better than 2 USD of copper in terms of machine performance.

Cost scenario diagrams were introduced in order to visualize the comparison of the performance to cost ratio for different machine designs. In this thesis, the ratios between torque production and material cost are compared. One can imagine a scenario where the PM material cost is very high and it is therefore beneficial to minimize the use of PM material. In another scenario, the PM material cost may have been reduced significantly and it is therefore beneficial to increase the use of PM material.

Cost scenario diagrams

An example of a cost scenario diagram is shown in Figure 5.1; permanent magnet cost on the vertical axis and copper cost on the horizontal axis. Point A is the default cost relation (Fe:Cu:PM), given by (2.1:7.1:82.3)=(1:3.4:39), previously presented in Table 5.1. Point B corresponds to a default iron price while both the copper and PM prices are increased by 50%, or a situation where the copper and PM prices keep their initial values while the iron price is reduced by 33%. In this way, the effect of a varying iron price can also be considered. Finally, point C refer to default iron and PM prices but a copper price that is reduced by 50%.

In order to make cost scenario diagrams, the torque production per cost is calculated for all the machines and different material cost scenarios according to

$$x_n = \frac{T_n}{m_{Fe}\$_{Fe} + m_{Cu}\$_{Cu} + m_{PM}\$_{PM}} \tag{5.1}$$

where m represents the mass of each material to produce the respective machine, n, and \$ is the material cost of each material. The maximum torque production per cost, $max(x_n)$, is calculated for each cost scenario. Machines that produce 95% or more torque per cost in comparison with the best machine are

considered as competitive designs for the cost scenario. All competitive machines, $x_n \geq max(x_n) \cdot 0.95$, are rewarded with a black dot in the corresponding location of their cost scenario diagram.

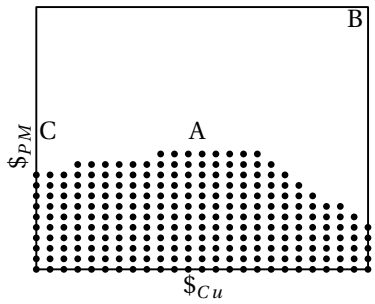

Figure 5.1: Example of a cost scenario diagram.

Regarding the example in Figure 5.1, the here investigated machine is not considered as a competitive machine design given the current material cost scenario, as there is no dot at point A. It is considered as competitive if the price of the permanent magnets is slightly reduced, as there are dots in the lower part of the diagram. It can also be seen that this particular design is not that sensitive to the price of copper when compared to the other designs.

5.1.3 Cost efficiency of the 12/5 machine designs

The output torque has been calculated at a speed of 1500 rpm for five different excitation levels, $J = [5\ 10\ 15\ 20]\ A/mm^2$, in the direction of the quadrature axis ($i_d = 0$). This to see the non-linear behavior of the machines and not to compare them in just one operating point.

The cost scenario diagrams for the 48 machine designs, previously presented in Table 4.4, excited by 5 A/mm^2 are shown in Table 5.4. It can be seen that the most cost competitive machines have a rotor diameter of 150-160 mm, and an air-gap of 0.8 mm. The maximal average permanent magnet flux density level, B_{max}, is not that critical at this relatively low current levels. It is clear that an air-gap flux density, $\hat{B}_1$, of 1 T is preferable compared to 0.85 T. Machine 2, 4 and 12 are the most cost competitive at the estimated current material cost scenario.

Table 5.4: Cost scenario diagrams for the 48 Q_s=12/p=5 machine designs at an excitation level of 5 A/mm^2.

		$l_g = 0.8$				$l_g = 1.2$			
		$\hat{B}_1$							
		0.85	1	0.85	1	0.85	1	0.85	1
D_r	150	1	2	3	4	5	6	7	8
	160	9	10	11	12	13	14	15	16
	170	17	18	19	20	21	22	23	24
	180	25	26	27	28	29	30	31	32
	190	33	34	35	36	37	38	39	40
	200	41	42	43	44	45	46	47	48
		1.3		1.5		1.3		1.5	
		B_{max}							

Table 5.5 shows cost scenario diagrams when the current excitation is $10 A/mm^2$, twice as high as in the previous case. In this case, a maximal average permanent magnet flux density level of 1.3 T is clearly preferable compared to 1.5 T. It can be seen that machine number 6 is competitive at this excitation level if the price of permanent magnets are reduced. One can also observe a shift towards greater rotor diameters.

Table 5.5: Cost scenario diagrams for the 48 Q_s=12/p=5 machine designs at an excitation level of 10 A/mm^2.

		$l_g = 0.8$				$l_g = 1.2$			
		$\hat{B}_1$							
		0.85	1	0.85	1	0.85	1	0.85	1
D_r	150	1	2	3	4	5	6	7	8
	160	9	10	11	12	13	14	15	16
	170	17	18	19	20	21	22	23	24
	180	25	26	27	28	29	30	31	32
	190	33	34	35	36	37	38	39	40
	200	41	42	43	44	45	46	47	48
		1.3		1.5		1.3		1.5	
		B_{max}							

When increasing the current density $5 A/mm^2$ further, the same but magnified tendencies are shown as before. The design variables of the air-gap and stator flux densities are at the same level for all the competitive machines. An air-gap length of 1.2 mm is still not beneficial considering the current cost scenario, but it will be by machine number 6 and 14 if the PM cost is lowered slightly.

Table 5.6: Cost scenario diagrams for the 48 Q_s=12/p=5 machine designs at an excitation level of 15 A/mm^2.

		$l_g = 0.8$				$l_g = 1.2$			
		$\hat{B}_1$							
		0.85	1	0.85	1	0.85	1	0.85	1
D_r	150	1	2	3	4	5	6	7	8
	160	9	10	11	12	13	14	15	16
	170	17	18	19	20	21	22	23	24
	180	25	26	27	28	29	30	31	32
	190	33	34	35	36	37	38	39	40
	200	41	42	43	44	45	46	47	48
		1.3		1.5		1.3		1.5	
		B_{max}							

As a last step, the current density is increased up to 20 A/mm^2, and the result is shown in Table 5.7. It can be seen that there is one machine design, number 14, that benefits from an increased air-gap length of, $l_g = 1.2$ mm, at this relatively high excitation level.

Table 5.7: Cost scenario diagrams for the 48 Q_s=12/p=5 machine designs at an excitation level of 20 A/mm^2.

		$l_g = 0.8$				$l_g = 1.2$			
		$\hat{B}_1$							
		0.85	1	0.85	1	0.85	1	0.85	1
D_r	150	1 	2 	3 	4 	5 	6 	7 	8 
	160	9 	10 	11 	12 	13 	14 	15 	16 
	170	17 	18 	19 	20 	21 	22 	23 	24 
	180	25 	26 	27 	28 	29 	30 	31 	32 
	190	33 	34 	35 	36 	37 	38 	39 	40 
	200	41 	42 	43	44 	45 	46	47 	48 
		1.3		1.5		1.3		1.5	
		B_{max}							

Based on the overall cost efficiency, considering all the four excitations levels, machine design number 10 turned out to be a favorable choice. Machine number 10 is therefore highlighted when the 12/5 machine designs are evaluated further.

5.1.4 Cost efficiency of the 24/11 machine designs

The cost scenario diagrams for the Q_s=24/p=11 machine designs have been calculated in exactly the same manner as in the previous section. The 48 designs, excited by 5 A/mm^2 are shown in Table 5.8. It can be seen that more machines turned out to be cost effective if comparing with the same excitation level for the Q_s=12/p=5 machine designs in Table 5.4. There are also several machines with lower air-gap flux density, $\hat{B}_1$=0.85 T, that are competitive at this relatively low current level. It can also be seen that there is a general shift towards higher rotor diameters compared with the Q_s=12/p=5 machine designs. This can be explained by the thinner stator yoke that is required when the number of poles are increased.

Table 5.8: Cost scenario diagrams for the 48 Q_s=24/p=11 machine designs at an excitation level of 5 A/mm^2.

		$l_g = 0.8$				$l_g = 1.2$			
		$\hat{B}_1$							
		0.85	1	0.85	1	0.85	1	0.85	1
D_r	150	1	2	3	4	5	6	7	8
	160	9	10	11	12	13	14	15	16
	170	17	18	19	20	21	22	23	24
	180	25	26	27	28	29	30	31	32
	190	33	34	35	36	37	38	39	40
	200	41	42	43	44	45	46	47	48
		1.3		1.5		1.3		1.5	
		B_{max}							

When increasing the current density to 10 A/mm^2, as shown in Table 5.9, there is a further shift towards higher rotor diameters but also a shift towards higher air-gap flux densities. At the current cost scenario, only machine design number 28 is competitive on the higher stator flux density level of B_{max}=1.5 T.

Table 5.9: Cost scenario diagrams for the 48 Q_s=24/p=11 machine designs at an excitation level of 10 A/mm^2.

		$l_g = 0.8$				$l_g = 1.2$			
		$\hat{B}_1$							
		0.85	1	0.85	1	0.85	1	0.85	1
D_r	150	1	2	3	4	5	6	7	8
	160	9	10	11	12	13	14	15	16
	170	17	18	19	20	21	22	23	24
	180	25	26	27	28	29	30	31	32
	190	33	34	35	36	37	38	39	40
	200	41	42	43	44	45	46	47	48
		1.3		1.5		1.3		1.5	
		B_{max}							

Cost scenario diagrams for a current excitation level of 15 A/mm^2 are shown in Table 5.10. The previous trend towards higher rotor diameters and air-gap flux density continues.

Table 5.10: Cost scenario diagrams for the 48 Q_s=24/p=11 machine designs at an excitation level of 15 A/mm^2.

		$l_g = 0.8$				$l_g = 1.2$			
		$\hat{B}_1$							
		0.85	1	0.85	1	0.85	1	0.85	1
D_r	150	1	2	3	4	5	6	7	8
	160	9	10	11	12	13	14	15	16
	170	17	18	19	20	21	22	23	24
	180	25	26	27	28	29	30	31	32
	190	33	34	35	36	37	38	39	40
	200	41	42	43	44	45	46	47	48
		1.3		1.5		1.3		1.5	
		B_{max}							

The cost scenario diagrams for the highest excitation level, 20 A/mm^2, of the $Q_s = 24/p = 11$ machine design are presented in Table 5.11. It can be seen that there are only two designs that are competitive at the current cost scenario, number 26 and 34. Both machines have the same design variables except for the rotor diameter.

Table 5.11: Cost scenario diagrams for the 48 Q_s=24/p=11 machine designs at an excitation level of 20 A/mm^2.

		l_g = 0.8				l_g = 1.2			
		$\hat{B}_1$							
		0.85	1	0.85	1	0.85	1	0.85	1
D_r	150	1	2	3	4	5	6	7	8
	160	9	10	11	12	13	14	15	16
	170	17	18	19	20	21	22	23	24
	180	25	26	27	28	29	30	31	32
	190	33	34	35	36	37	38	39	40
	200	41	42	43	44	45	46	47	48
		1.3		1.5		1.3		1.5	
		B_{max}							

It can be noticed that none of the designs where the air-gap length, l_g=1.2 mm, are cost competitive for the Q_s=24/p=11 designs. However, it can be mentioned that when studying the output torque at the highest current density of 20A/mm^2, regardless of the machine cost; it was actually the machines with an air-gap length of, l_g=1.2 mm, that delivered the highest torque for both the Q_s=12/p=5 and the Q_s=24/p=11 designs. The higher torque is produced to an considerably increase of the PM cost, as the PM lengths are increased according to Table 4.5, they are not considered cost efficient and can therefore not be seen in the cost scenario diagrams.

Both machine number 18 and 26 turned out to be cost efficient when considering all the four excitation levels. Except for the highest excitation level, machine

18 is favorable while machine number 26 is favorable with exception from the lowest excitation. Both machine number 18 and 26 are therefore highlighted when the 24/11 configurations are evaluated further.

5.1.5 Torque speed characteristics of the 12/5 machine designs

The torque speed characteristics are calculated based on the 10 A/mm^2 operating point from the cost scenario section. Appropriate turn selections are calculated for each machine design in order to enter field weakening as close as possible to 2250 rpm, as the number of turns must be chosen as a discrete value. The turn selections are made for an excitation of 10 A/mm^2 and a maximum peak phase voltage of $V_{ph-max} = 500 \cdot 2/\pi$ V.

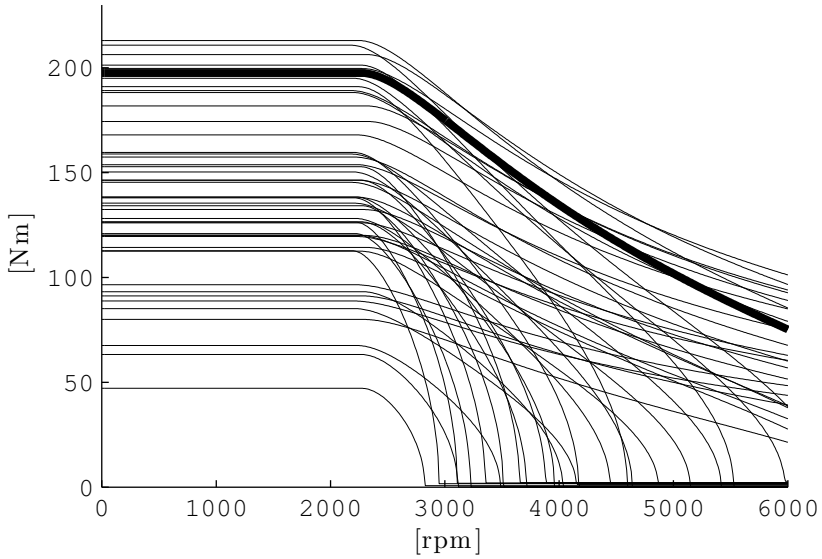

Figure 5.2: Torque speed characteristics for the 48 design combinations when $n_n = 2250$ rpm, 10 A/mm^2 and $V_{ph-max} = 500 \cdot 2/\pi$ V. Machine number 10 is plotted using a thicker line width.

The torque speed characteristics of the 48 design combinations of the Q_s=12/p=5 configuration are shown in Figure 5.2. Machine number 10 was regarded as the most promising design considering the evaluation of the cost scenario diagrams previously, machine number 10 is therefore plotted using a thicker line width in Figure 5.2. It can be seen that machine number 10 is not only cost effective, it offers also a reasonable torque speed characteristics compared to several of its

competitors. Machine number 10 is therefore chosen as the final Q_s=12/p=5 design and called **machine A** from now and on.

5.1.6 Torque speed characteristics of the 24/11 machine designs

Figure 5.3 shows the torque speed characteristics of all the 48 design combinations for the Q_s=24/p=11 configuration, calculated in the same way as in the previous section. Both machine number 18 and number 26 were regarded as promising designs when evaluating the cost diagrams. The two most interesting designs are plotted using thicker lines in Figure 5.3. Both the machines offers approximately the same peak torque when excited by 10 A/mm^2 but machine 26 shows a better torque speed performance in the field weakening region. Machine number 26 is therefore chosen as the final Q_s=24/p=11 design and called **machine B** from now and on.

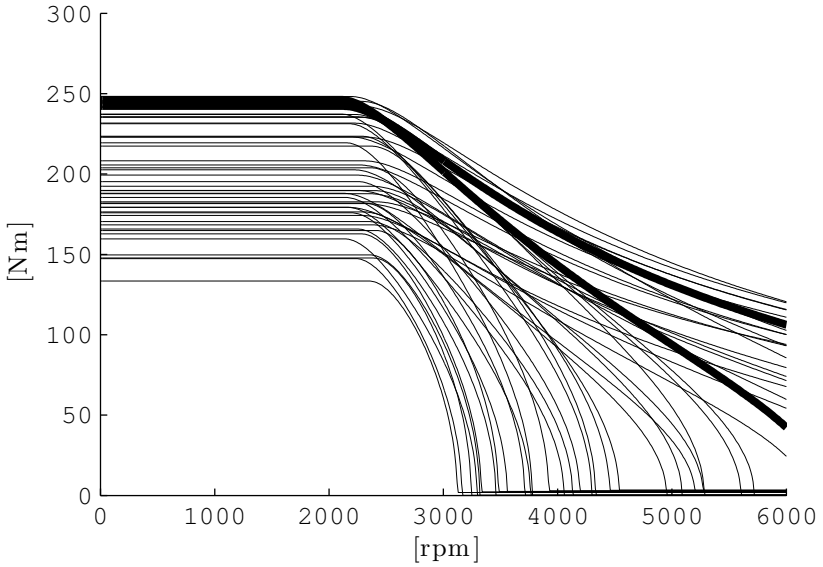

Figure 5.3: Torque speed characteristics for the 48 design combinations when $n_n = 2250$ rpm, 10 A/mm^2 and $V_{ph-max} = 500 \cdot 2/\pi$ V. Machine number 18 and 26 are plotted using a thicker line width.

5.2 The two selected machine designs

The geometry of machine A and B are shown in Figure 5.4.

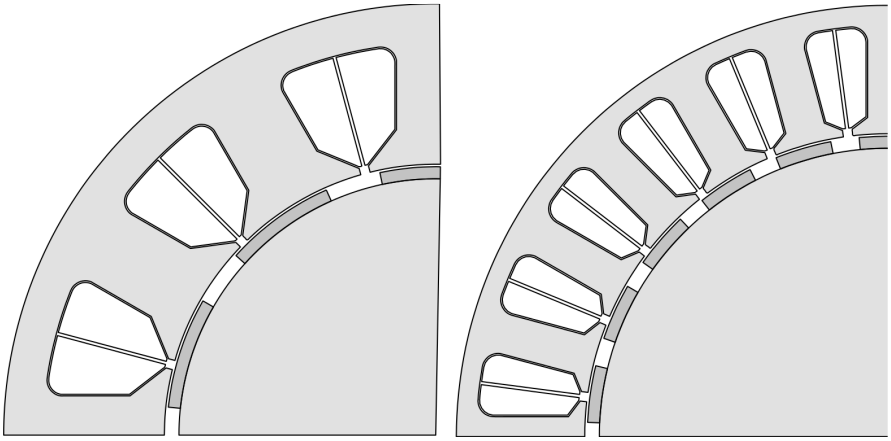

Figure 5.4: Geometry of machine A and machine B

5.2.1 Estimation of end-windings

The protrusion of the end-windings has been estimated according to the illustration in Figure 5.5, where the width of the coil, W_{cu}, is calculated as half the average slot width. The average slot width has been estimated as

$$W_{cu} = \frac{\pi(D_r/2 + l_{pm} + l_g + l_{shoe} + D_{out} - l_{yoke}) - Q_s l_{tooth}}{2Q_s} \tag{5.2}$$

The bend of the coil is assumed to have a minimum bend radius, r_{cu}. The total space occupied by the end-windings in axial direction is then $2(W_{cu} + r_{cu})$. The calculated values for the two machines are presented in Table 5.12.

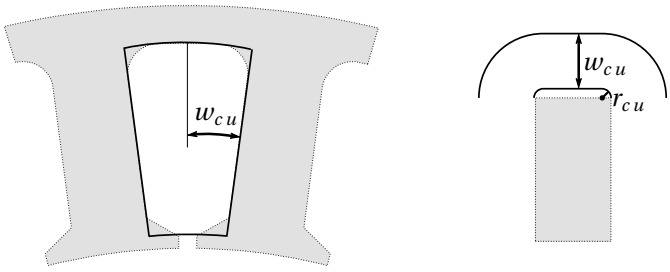

Figure 5.5: Illustration of how the axial protrusion of the end-windings have been estimated.

No measured values of the total length (stator stack + end-windings) of the Prius 2004 machine was found. However, using the known stack length of 84 mm and a photograph presented in [47], the total length was estimated to be around 140 mm. According to [48], the end-windings or the "coil-end length" of the Toyota Prius 2010 machine are 29 mm each. In [36] it is shown that the winding configuration of the 2004 and the 2010 Prius machines are not identical but similar. The total length of the 2004 Prius stack length in [36] and the end-windings of the 2010 Prius in [48] is 142 mm.

If a total length of 140 mm is assumed together with the values presented in Table 5.12, it was possible to extend the 2004 Prius stack length by 24% for machine A and by 40% for machine B. These numbers are to be compared with the assumption of 30% made in section 4.1. By adding the estimated end-windings to the assumed stack length of 108 mm, the total stack length of machine A turned out to be 146 mm and machine B turned out to be 132 mm. These numbers indicate that machine A has been made 6 mm too long and that it is possible to extend machine B by 8 mm additionally. Because of time constraints and the uncertainties involved in the end-winding estimation, it was decided to keep the stator stack length according to the initial assumption of 30% extension of the 2004 Prius stator stack length.

Table 5.12: End-winding estimation using a minimum bend radius, r_{cu}, of 3 mm.

	Machine A	**Machine B**
W_{cu} **[mm]**	15.5	8.5
$2(W_{cu}+r_{cu})$ **[mm]**	37.0	23.00

5.2.2 Turn selection

The intention was to select the number of turns as high as possible to maximize the low speed torque without reducing the output power by voltage limitation at higher speeds. The same voltage (225 V_{RMS}) and current (250 A_{RMS}), as presented for the Prius 2004 machine in Section 4.1.1 are used as limits. Figure 5.6 and 5.7 show possible torque speed characteristics for the two machines when varying the number of turns in five steps. 13 turns was regarded as a suitable choice for machine A and 8 turns for machine B.

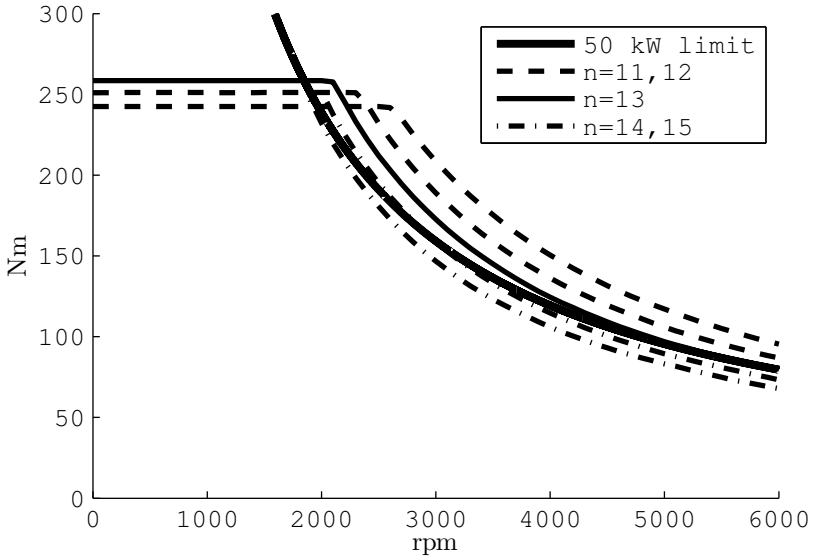

Figure 5.6: Torque speed characteristics for five different turn selections of machine A.

When taking a closer look at Figure 5.7, one can see that the output power actually is slightly limited by the voltage using the turn selection, n=8. The reason is that a linear model was used, in an earlier stage. When determining the number of turns and using the linear model, the voltage limit was not affecting the output torque at higher speeds. Both Figure 5.6 and 5.7 have been reproduced using dense data that was obtained in connection to the calculation of the efficiency maps shown in Section 5.3. This is also the reason why the current limited torque at lower speeds can't be seen for the higher number of turns; such high currents were not included in the data obtained in Section 5.3.

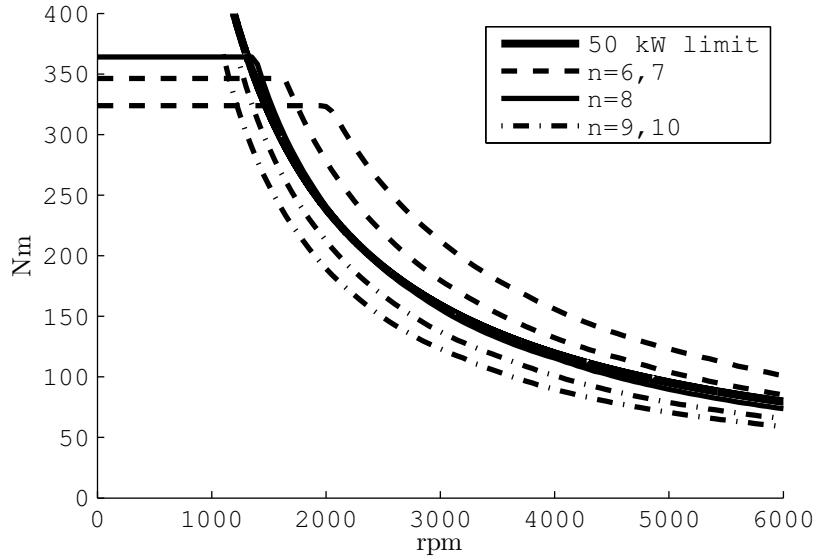

Figure 5.7: Torque speed characteristics for five different turn selections of machine B.

5.2.3 Thermal impact of the slot geometry

The thermal conductivity of the winding mix i.e. copper, insulation and impregnation is extra critical in concentrated winding fractional slot machines, as the slots are fewer and larger than in a conventional machine. Due to the larger slots and the relatively low thermal conductivity of the winding mix (compared to the stator lamination) a greater thermal gradient is expected across the winding mix inside each slot. It is necessary to achieve a high thermal conductivity of the winding mix to keep the winding temperature within adequate levels.

The thermal characteristics of two slot segments of the stator are analyzed in a somewhat simplified 2D model, one for machine A and one for the 2004 Prius slot geometry presented in [37]. The simplified geometries are shown in Figure 5.8; the air pockets in the slot openings are removed and a 0.5 mm thick and 0.2 W/(m·K) insulation film is placed between the winding mix and the stator lamination. A thermal conductivity of 28 W/(m·K) is used for the stator lamination. Insulation boundaries are used around the stator segment except for the outer boundary, representing the surface of the stator yoke, where a fixed temperature is used. The winding mix is then evenly excited by its portion of 5% copper loss in a 50 kW machine. This to show the temperature rise inside the different parts of the stator segments relative a fixed temperature of the outer

stator surface due to the copper losses.

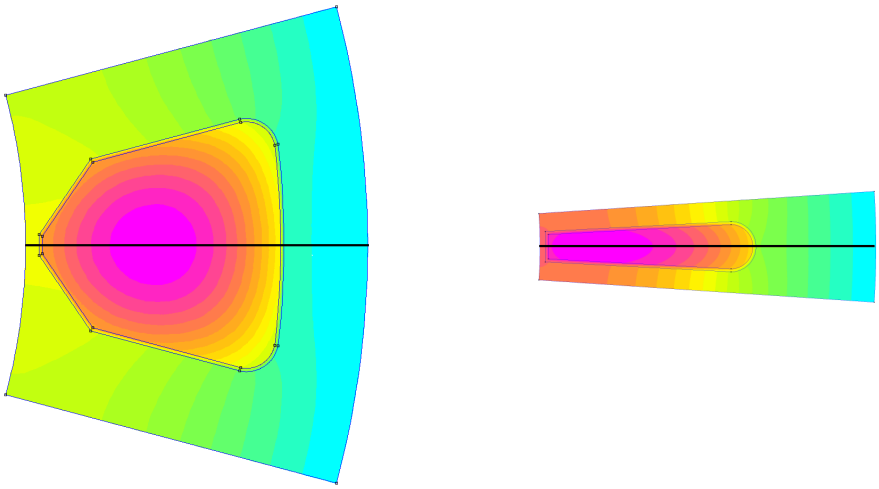

Figure 5.8: Simplfied 2D geometries used to calculate relative temperature rise within a stator segment.

The distribution of the temperature rise along the black center lines in Figure 5.8 are shown in Figure 5.9. They are plotted for two different thermal conductivities of the winding mix, 0.5 W/(m·K) and 3 W/(m·K), for both geometries. It is clear that the thermal conductivity of the winding mix is of great importance for the maximum winding temperature of machine A; the difference is about $27^{o}C$ depending on the thermal conductivity of the winding mix material. For the 2004 Prius machine, the maximum winding temperature is only affected by a few degrees.

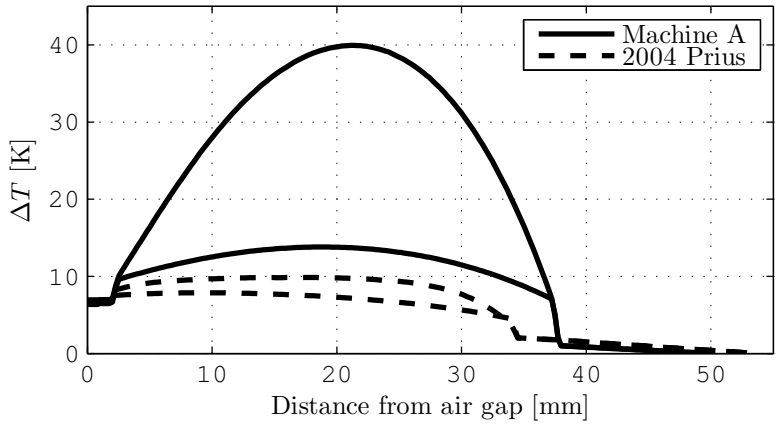

Figure 5.9: Relative temperature rise across the stator slot for two different thermal conductivities of the winding mix, 0.5 W/(m·K) and 3 W/(m·K) respectively.

5.2.4 Thermal restriction of the electric loading

The temperature distribution along a line, from the air-gap through the winding and to the outer stator yoke, was shown previously in Figure 5.9. In this section, the temperature rise at the maximum temperature along this line or the hottest spot inside a winding is calculated relative to a constant temperature at the surface of the outer stator yoke. This temperature difference is denoted ΔT_{max} and is calculated as function of the phase current for six different values of the equivalent thermal conductivity of the winding mix in the slot,
λ_{w-mix}=[0.5 1 1.5 2 2.5 3] W/(m·K). The aim is to find current density values for the two machines, A and B, and the Prius 2004 machine where the temperature rise of the windings are of the same or similar magnitude.

The relative temperature rise, ΔT_{max}, are shown for the three machines in Figure 5.10, where solid lines are used for λ_{w-mix}= 1.5 W/(m·K). One can directly conclude that machine A is the most sensitive to the thermal conductivity of the winding mix as the curves are rather spread, this is due to the relatively large slots of machine A. In the same way, the Prius 2004 machine is the least sensitive due to its relatively small slots.

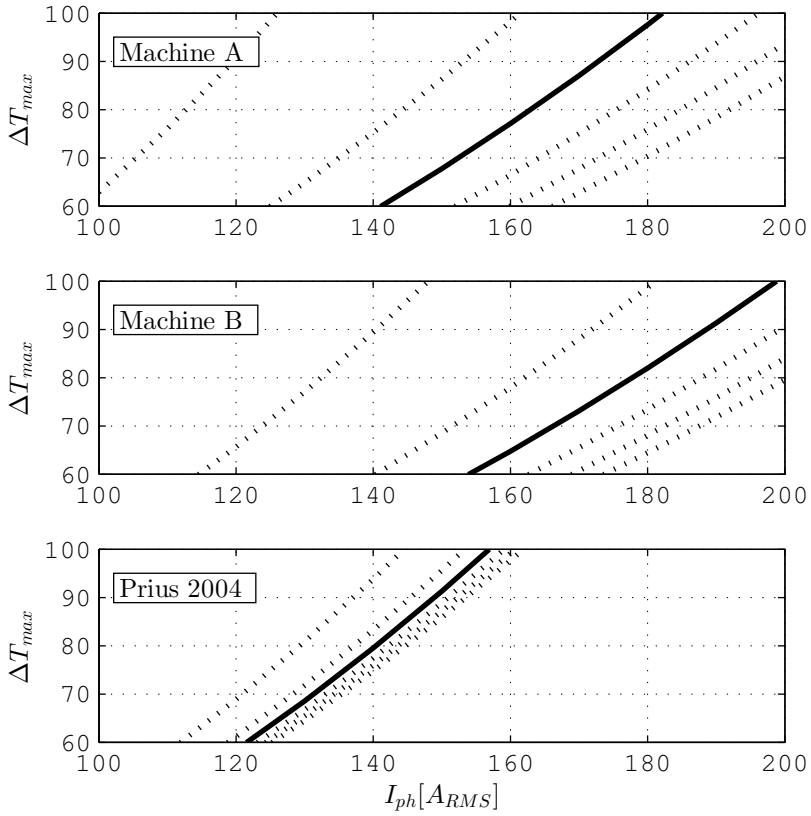

Figure 5.10: The relative temperature rise, ΔT_{max}, of the hottest spot in the winding in relation to the outer stator yoke surface as function of phase current, for different values of thermal conductivity. The solid lines correspond to an equivalent thermal conductivity of 1.5 W/(m·K) for the winding mix.

An equivalent winding mix conductivity of λ_{w-mix}= 1.5 W/(m·K) and a relative temperature rise of ΔT_{max}=80^{o}C have been assumed as an operating point with reasonable current density levels where the three machines can be compared. The relative temperature rise of ΔT_{max}=80^{o}C is chosen to leave some margin for additional heat flux to build up the thermal gradient further due to other loss components. This operating point should therefore not be considered as an absolute value of continuous operation.

5.3 Efficiency

Before the efficiency maps can be obtained, the operating points have to be calculated. A number of transient simulations, for different i_d and i_q combinations, were carried out for each machine. The average torque as a function of the currents, $T_{avg}(i_d, i_q)$, and the fundamental component of the stator flux as a function of the currents, $\Psi_{dq}(i_d, i_q)$, were calculated. The shortest current vector, $\min\left(\sqrt{i_d + i_q}\right)$, that fulfills the current limit, the power limit and the voltage limit is then calculated for each operating point.

The efficiency maps have been interpolated over 126 operating points made up by 9 current excitation levels and 14 speed levels, represented by the black dots in the efficiency maps. The outer black lines in the efficiency maps show the peak torque limited by current or voltage or power. The inner black lines shows the calculated torque limited by their respective ΔT_{max}=80^{o}C current, defined in the previous section.

Each operating point is simulated over two electrical periods where the losses have been calculated as an average over the last period. Core losses, P_{Fe}, of the rotors and stators are extracted directly from the FEA software together with the eddy current losses in the PMs, P_{PM} . Copper losses, P_{Cu}, are calculated in a postprocess manner using phase currents and phase resistances. The Prius 2004 phase resistance of 69 mΩ at 21 ^{o}C presented in [36] has been recalculated to 91.5 mΩ corresponding to the copper resistivity at 120 ^{o}C in Section 4.3. The phase resistances of machine A, 20.5 mΩ, and machine B, 28.1 mΩ, are calculated including the estimations of the end-windings presented in Section 5.12 and considering the copper resistivity at 120 ^{o}C. The output power is calculated as the average torque multiplied with the mechanical speed at each operating point. The efficiency, η, in the efficiency map represents then

$$\eta = \frac{T_{avg}\Omega}{T_{avg}\Omega + P_{Fe} + P_{PM} + P_{Cu}} \tag{5.3}$$

The efficiency map of machine A can be seen in Figure 5.11, the peak torque at a phase current of 250 A_{RMS} is 250 Nm while the peak torque at ΔT_{max}=80^{o}C is 214 Nm. One can observe that the highest efficiency is obtained at relatively low torque and speed levels, as the losses are strongly dependent on both the current or flux levels and frequency.

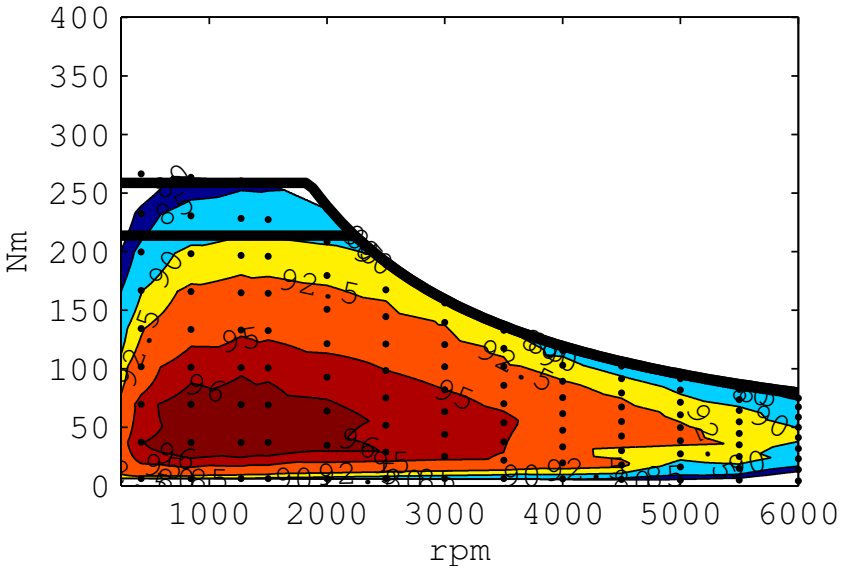

Figure 5.11: Interpolated efficiency map of machine A.

Figure 5.12 shows the efficiency map of machine B, the two black lines represents the peak torque at 250 A_{RMS} and at ΔT=80^{o}C respectively. Both the current and thermal limited torque are higher for machine B compared to machine A. Also the overall efficiency is higher, regardless of the higher pole number and the higher electric frequency.

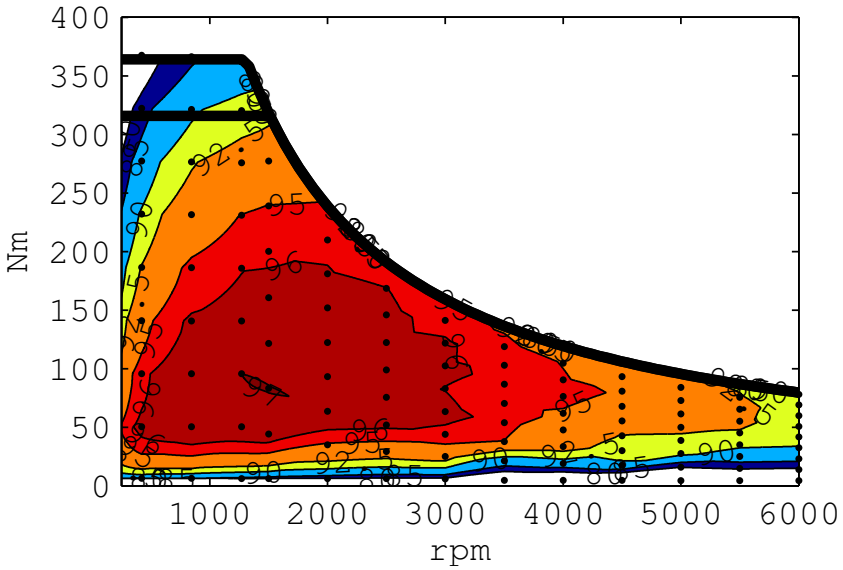

Figure 5.12: Interpolated efficiency map of machine B.

The calculated efficiency map of the 2004 Prius machine can be seen in Figure 5.13. One can notice that the efficiency is below 80% when the peak torque is delivered, the measured efficiency map in [38] shows a similar result. The overall picture when comparing the calculated and the measured efficiency maps, is that the efficiency presented in Figure 5.13 is somewhat generally higher than in [38]. The peak efficiency is also shifted from around 2250 rpm in [38] to approximately 3500 rpm in Figure 5.13. There are a number of possible sources for the discrepancy. First of all, sinusoidally shaped currents have been used when calculating the efficiency using FEA while the voltage over the measured machine has been switched. Torque measured on the machine shaft is lower than the electrodynamic torque due to mechanical losses. The exact method of how the current angle is chosen in the real system is not known, it may not be the same as the one presented in the beginning of this section. There is always an uncertainty related to the loss calculation in the simulations, especially to the core loss calculation. But there are also uncertainties involved when measuring efficiency.

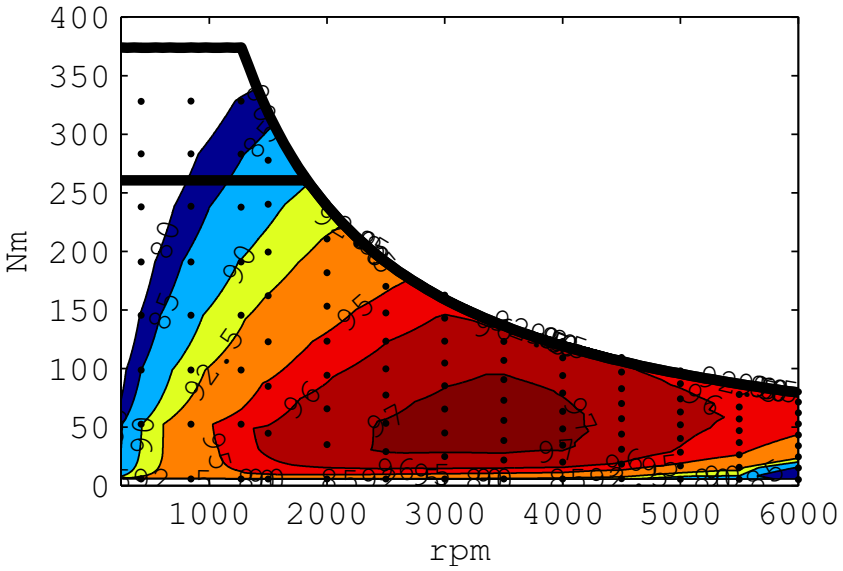

Figure 5.13: Interpolated efficiency map of the Prius 2004 machine.

5.4 Summary of comparison

Some figures from the comparison of machine A, machine B and the Prius 2004 reference machine are presented together in Table 5.13. The major difference in material consumption is that the 2004 Prius machine requires a considerable lower amount of copper and a slightly higher amount PM material. The fractional slot machine designs end up with the same material cost, which is about 8% higher than the 2004 Prius machine. Machine B and the 2004 Prius machine deliver similar torque in the current limited low speed region, while the torque production of machine A is substantially lower. The current density of the 2004 Prius is about twice the current density of machine B, which is a consequence of the relatively large end-windings and the low copper material consumption. Therefore, the torque production of machine B is considerable higher at the calculated $\Delta T_{max} = 80^o\,C$ excitation level.

Table 5.13: Some figures collected from the comparison of the three machines.

	Prius 2004	**Machine A**	**Machine B**
Outer stator diameter [mm]	269	269	269
Estimated total length [mm]	140 [1]	146 [1]	132 [1]
$\mathbf{T}_{max}$ **[Nm]**	374	258	364
$\mathbf{T}_{\Delta T_{max}\,80^o C}$ **[Nm]**	261	214	316
PM [kg]	1.232	1.050	1.178
Cu [kg]	6.8	13.739	9.776
Fe [kg]	29.25	36.51	35.79
Material cost [USD]	211	228	228
$\mathbf{T}_{max}$**/Cost [Nm/USD]**	1.77	0.990	1.51
$\mathbf{T}_{\Delta T_{max}\,80^o C}$**/Cost [Nm/USD]**	1.24	0.821	1.31
J @ $\mathbf{T}_{max}$ $[\boldsymbol{A_{RMS}/mm^2}]$	29.4	13.2	15.6
J @ $\mathbf{T}_{\Delta T_{max}\,80^o C}$ $[\boldsymbol{A_{RMS}/mm^2}]$	16.5	8.6	11.1

[1] See Section 5.2.1 for estimation of total lengths (stator stack + end-windings).

Chapter 6

Analysis of the chosen fault-tolerant fractional slot machine

This chapter deals with the further analysis of one of the fault-tolerant PMSM machine designs that are presented earlier in this thesis. Of the machine designs evaluated in Chapter 5 , machine B turned out to be a promising design and it is thus considered in this chapter regarding analysis of unbalanced operation as well as MMF harmonic content on the rotor side during balanced operation.

Although some converter limitations related to a number of converter topologies are presented briefly in section 2.4, the analysis of unbalanced operation is mainly done from a machine perspective, where the same phase RMS current (250 A_{RMS}) and the same phase peak voltage (318 V) that are available during balanced operation are assumed to be available during unbalanced conditions as well. The analysis is based on two different methods; in the first method, the currents are arranged to maintain constant direct and quadrature components in the dq0 reference frame, as presented in section 2.5.2. This first method takes only the fundamental frequency components into account and does not include the different saturation levels of the phases during unbalanced operation. Using the second method, that is based on the numerical solution of operating points presented in section 3.2, both the difference in saturation level of the phases and several harmonic components are included.

6.1 Unbalanced operation using resonant controller

In this section, the ordinary PI controller together with the resonant controller presented in Section 2.5.2 are used to find steady-state operating points when a

single phase open circuit fault or a single phase short circuit fault occurs. The operating point found for the single phase open circuit fault is simulated and analyzed also using transient FEA and using the per phase flux machine model described in Chapter 3.

6.1.1 Phase open circuit

The simulation of a phase open circuit is divided into three time periods, separated by vertical dashed lines in the figures. The first part corresponds to normal operation at 1300 rpm and the current references are put to; $i_d^* = 0$ A and $i_q^* = 150\sqrt{2}/3$ A, controlled by only the PI controller. This operating point is chosen to illustrate an example where both the phase currents and phase voltages are kept within the given boundaries. In the second part, phase C is opened close to its current peak and the current is controlled down to zero as a first order system of 1 MHz bandwidth, mimicking an interruption due to a open circuit fault. During the second part, the resonant controller is still turned off and the PI controller alone, tries to reach the same current references as in the first time period. In the third and last part, the resonant controller is turned on while the current reference, i_q^*, is reduced by a factor $1/\sqrt{3}$ to end up with phase currents of the same magnitude as during the normal operation in the first time period.

As the intention is to show the three steady-states in the same figures, the controllers are tuned accordingly to achieve that. Therefore, the dynamic behavior during the two transitions between the three time periods are not representative. As an example, a_0 and a_2 of the resonant controller, see Figure 2.6, are put to zero according to [15] while a_1 is put to a value high enough to quickly remove the oscillations in i_d and i_q.

The dq0 transformation of the phase currents are shown in Figure 6.1. During normal operation, they are following their references as expected and the zero sequence component is zero as it is a balanced three phase operating point. When the fault occurs and phase C is opened, it can be seen that the PI controller alone cannot control the currents according to the references and there are oscillations in all the dq0 components. In the third time period, when the resonant controller is activated, the oscillations are removed from i_d and i_q while only i_0 is left oscillating.

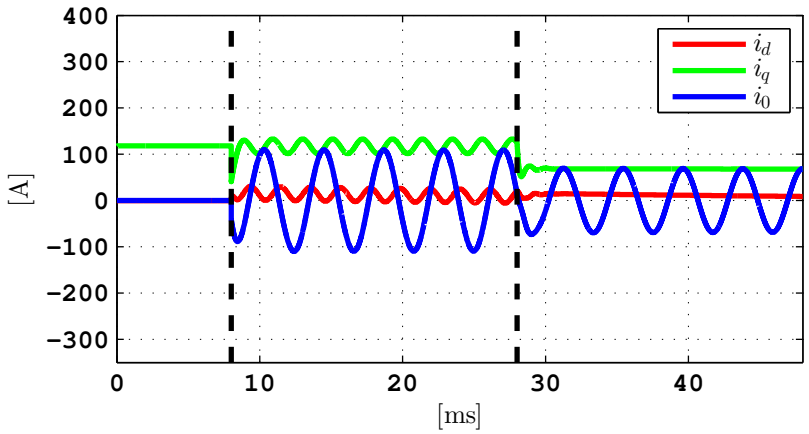

Figure 6.1: The dq0 transformation of the phase currents during normal and open circuit fault operation without and with resonant controller.

Figure 6.2 shows the phase currents during the three time periods. It can be seen that the current in phase C is interrupted when the fault occurs. In the third time period, the phase shift between phase A and B is 60 electrical degrees and both phases are shifted 30 degrees with respect to their respective phase angle during normal operation.

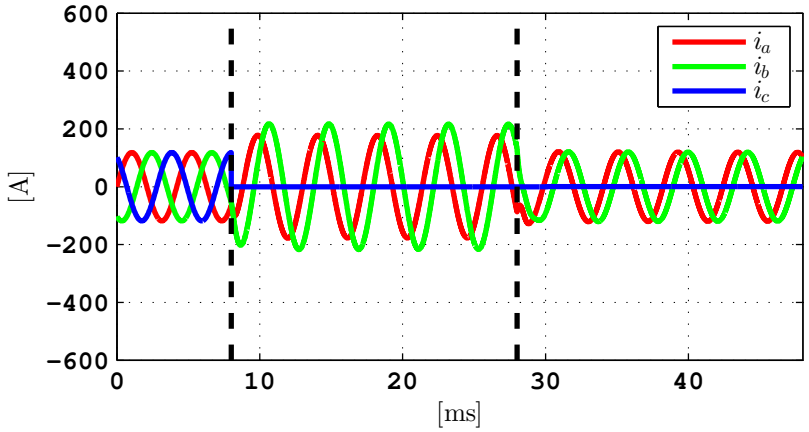

Figure 6.2: The phase currents during normal and open circuit fault operation without and with resonant controller.

The three phase voltages are presented in Figure 6.3. Considering the steady-states, it can be seen that the phase voltages are kept below 500·2/π=318 V at

the current operating point. It can also be noted that the phase voltage of phase A is considerably higher than both phase B and C in the last time period. This is due to the fact that the current of phase A is shifted towards the PM flux vector in phase A, corresponding to a positive direct axis magnetization.

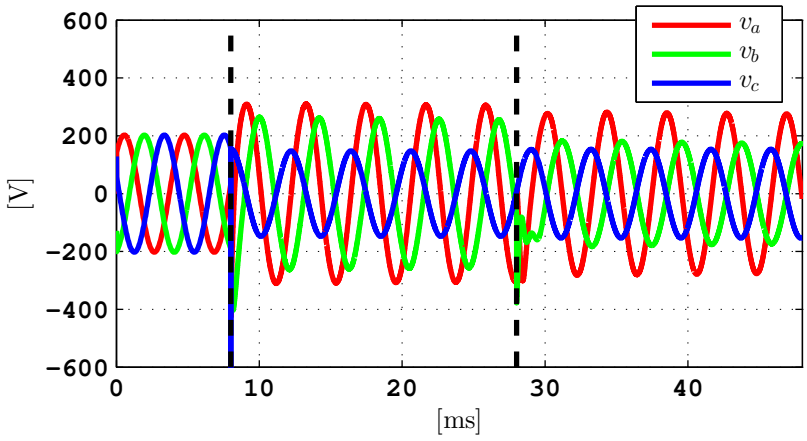

Figure 6.3: The phase voltages during normal and open circuit fault operation without and with resonant controller.

Figure 6.4 shows the torque production, the portion from each phase and the sum of the three phases. It can be seen that the oscillations in i_d and i_q give rise to oscillations also in the torque in the second time period, where the PI controller without resonant controller is used. The torque oscillations disappear when the resonant controller is activated. It can be noted that phase A and B produce sinusoidal torque components that are displaced 180 electrical degrees. This can be regarded as a fairly effective way of producing a DC torque level, because of the small amount of negative torque required.

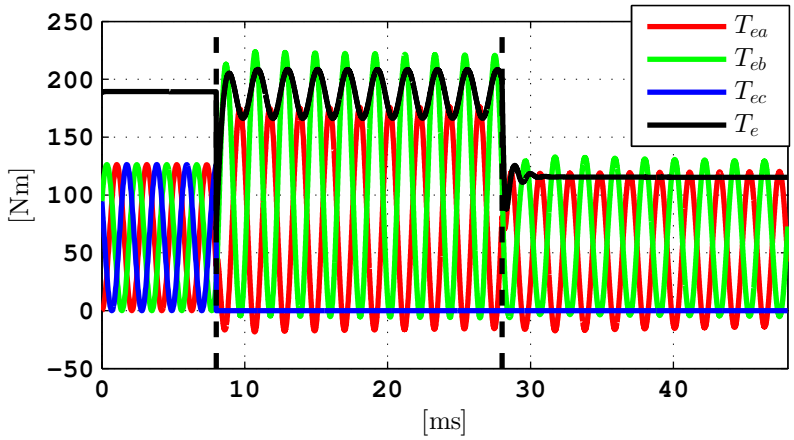

Figure 6.4: The torque production during normal and open circuit fault operation without and with resonant controller.

Comparison with FEA and the per phase flux machine model

The steady-state operating point found by the resonant controller, is simulated with the non-linear machine models; using transient FEA and using the per phase flux machine model. The phase currents for 7.5 ms of normal operation and 7.5 ms of phase open circuit operation are shown in Figure 6.5.

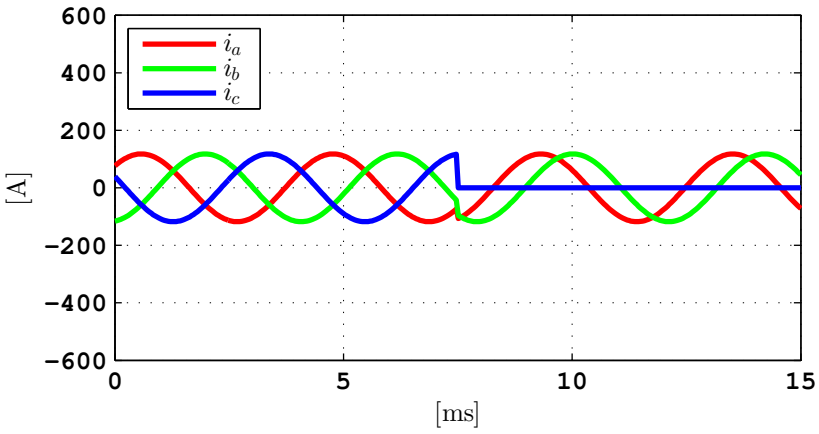

Figure 6.5: The three phase currents used as input to both the FEA and the per phase flux machine model.

The calculated torque can be seen in Figure 6.6, where the black line represents the result from the transient FEA. In this specific operating point, the ripple

torque during normal operation is approximately 5% of the average torque while it is around 25% when the machine is operated during open circuit fault. The torque calculated using the per phase flux machine model gives a result that is very close to the transient FEA. If comparing Figure 6.6 and Figure 6.4, it can be seen that an additional torque ripple is introduced when the non linear machine models are excited to keep the resulting quadrature component of the current constant.

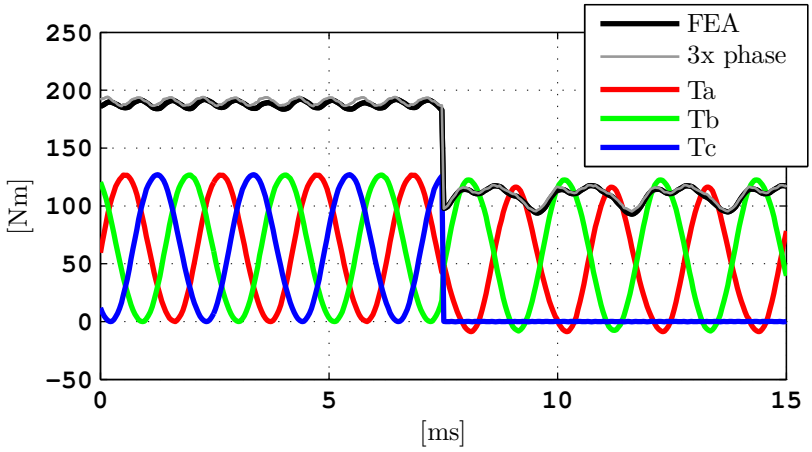

Figure 6.6: Torque production during 7.5 ms of normal operation and 7.5 ms of phase open circuit operation.

The three phase voltages obtained by the FEA and the per phase flux machine model are shown in Figure 6.7. It is hard to distinguish the results and the voltages are distorted, especially when the machine is operated during open circuit fault. The voltages during the last 7.5 ms are to be compared with the third time period in Figure 6.3. It is clear that phase A is the most distorted, as the current in phase A produces induced flux that enhances the PM flux while the current in phase B induces flux that weakens the PM flux, see the phase vectors shown on Figure 2.9 in section 2.5.3.

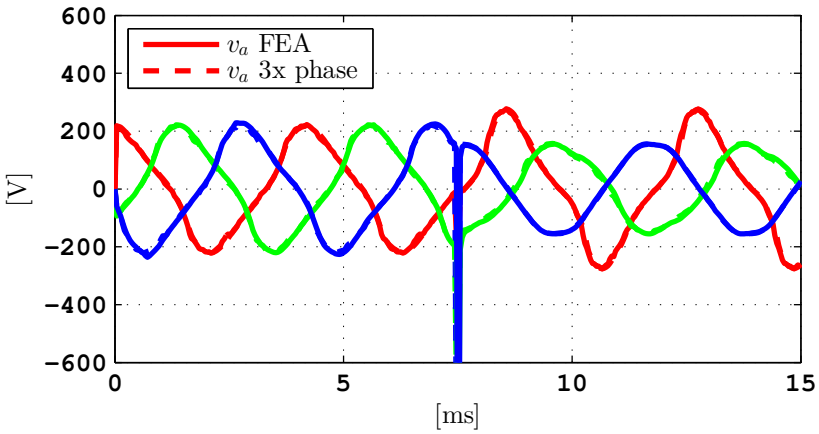

Figure 6.7: Phase voltages during 7.5 ms of normal operation and 7.5 ms of phase open circuit operation.

6.1.2 Phase short circuit

This section shows the event of a phase short circuit fault in the same manner as the open circuit fault in the previous section. Both the same operation point and the same controller reaction are considered. The only difference is that the terminal voltage of the faulty phase (C) is instantaneously put to zero, instead of controlling the phase current to zero.

The dq0 transformation of the phase currents are shown in Figure 6.8. It can be seen that oscillations are introduced in all the dq0 components when phase C is short circuited. When the resonant controller is activated, the oscillations are removed from i_d and i_q again.

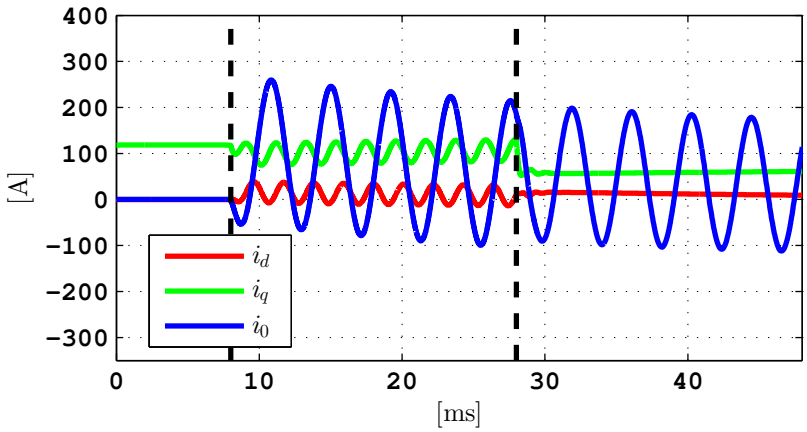

Figure 6.8: The dq0 transformation of the phase currents during normal and short circuit fault operation without and with resonant controller.

The three phase currents are presented in Figure 6.9 and some critical changes can be observed. First of all, there is current in phase C as it is short circuited. The short circuit current is limited to about 84 A_{RMS} by the impedance of the phase, mainly the inductance. The current in the faulty phase will introduce an additional torque component compared with the case of an open circuit fault. The final steady-state cannot be seen in Figure 6.9 but the phase shift between phase A and B will end up to around 35 electrical degrees for this particular operating point. As a consequence, this operating point is even further away from the balanced case, compared with the open circuit fault. The phase current of both phase A and C end up with approximately the same amplitudes as during normal operation, while the amplitude of phase B is increased by 76% to maintain the current reference, i_q^*, that is still reduced by a factor $1/\sqrt{3}$.

The torque production of the three phases during normal and short circuit operation are shown in Figure 6.10. It can be observed that there are a lot of oscillations in the different torque components and that there are a considerable amount of negative torque that is produced. One can conclude that the control strategy, using the PI and the resonant controller and only utilizing the fundamental frequency, to maintain a DC torque level is not that strategic; a great portion of the torque produced by phase A and B cancel out each other.

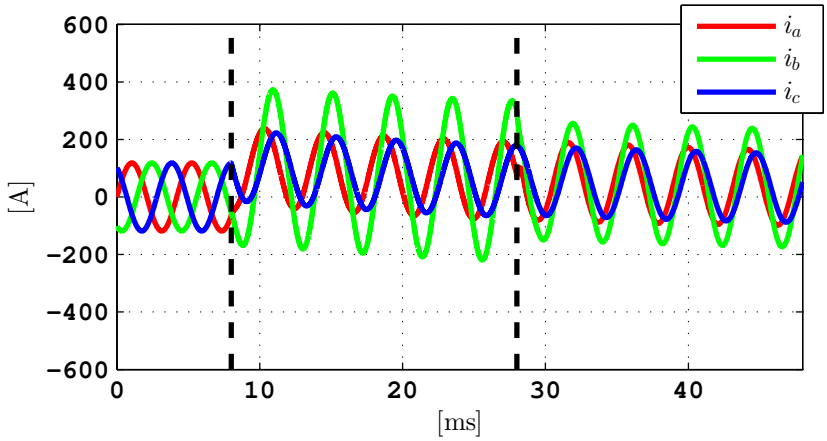

Figure 6.9: The phase currents during normal and short circuit fault operation without and with resonant controller.

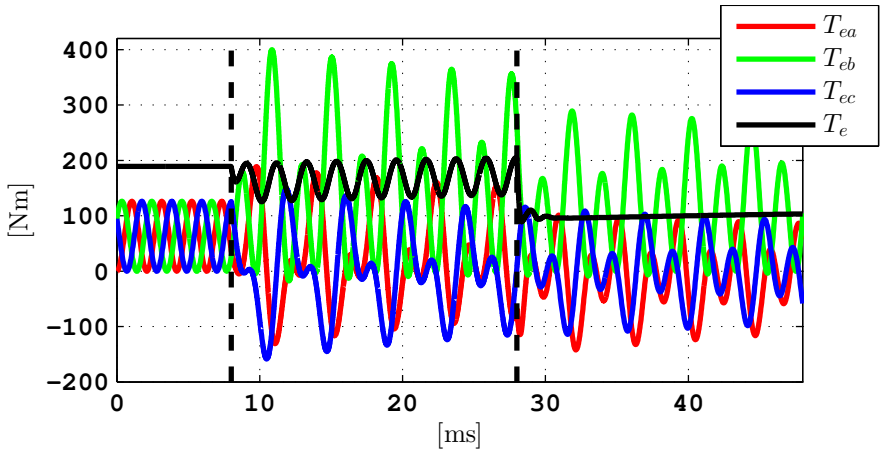

Figure 6.10: The torque production during normal and short circuit fault operation without and with resonant controller.

6.2 Numerically calculated unbalanced operating points

This section is based on the per phase flux machine model introduced in Chapter 3. The impact of harmonic content in the currents are analyzed and torque speed characteristics during a phase open circuit fault and a phase short circuit fault are evaluated.

6.2.1 Filtering of numerically calculated currents

In the flowchart, presented in Figure 3.7, it shown that the shortest current vector, $\min\left(\sqrt{i_a^2+i_b^2}\right)$, for a given torque reference, T^*, is calculated based on a torque map. The calculated current waveforms are then low pass filtered using a discrete Fourier transform (DFT) in order to remove unrealistically high harmonics. It is therefore of interest to analyze the magnitude of the torque ripple that is introduced as a consequence of the filtering. The peak to peak torque ripple expressed relative to the average torque in percent is presented in Figure 6.11 for different number of harmonics.

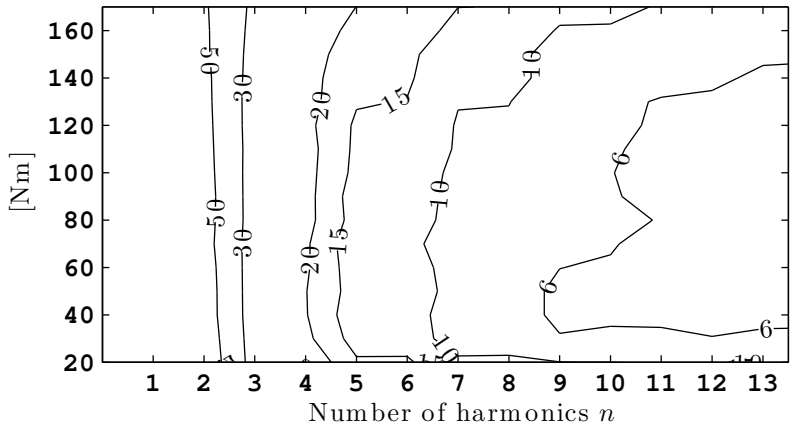

Figure 6.11: Peak to peak torque ripple expressed relative to the average torque in percent for different number of harmonics.

A choice of how many harmonics to include in the currents is a trade-off between torque quality and other constraints. The torque ripple is of course reduced with an increased harmonic content as seen in Figure 6.11, but higher harmonic content will likely increase the losses. Higher voltage may be required when the harmonic content of the current is increased, thereby is it possible that the speed will be further limited for a certain DC-link voltage. The controller bandwidth is another aspect to consider with a higher harmonic content. A torque ripple of 10-15% in the interval 20-170 Nm is assumed to be reasonable, why a harmonic content of n=7 has been chosen.

6.2.2 Torque speed characteristics

The torque speed characteristics of machine B, when using two different numbers of harmonic content, during phase open circuit fault is presented in Figure 6.12. The current limited low speed torque is 175 Nm, which is about 17% lower than the theoretical limitation presented in Section 2.4 (364/$\sqrt{3}$=210 Nm). The torque reductions start at 400 rpm and 600 rpm respectively. At 2000 rpm, the torque production has dropped to 53 Nm and 62 Nm respectively and it decreases fast until it becomes zero at about 2600 rpm.

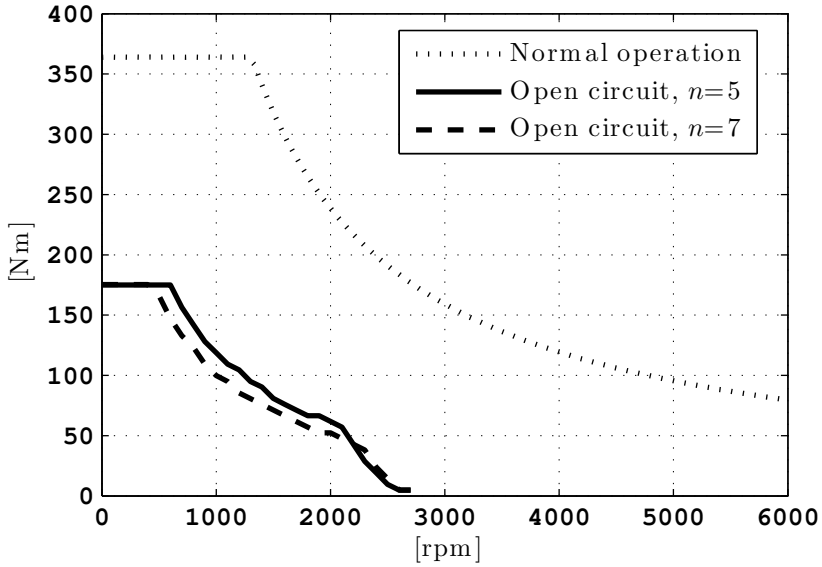

Figure 6.12: Torque speed characteristics of machine B during open circuit fault.

In Figure 6.13, the torque speed characteristics of machine B during phase short circuit operation is shown. The torque production is calculated for two different numbers of harmonic content, a local minimum at around 40 rpm can be seen in both cases. The local minimum coincide with the maximum of the braking torque produced by the short circuited phase C, see $|T_{c-avg}|$ in Figure 6.13. The speed levels, where the torque must be reduced are actually slightly higher than in the case of the open circuit fault, 600 rpm and 700 rpm respectively. After that, the torque is reduced faster compared with the open circuit fault. The remaining phases must not only produce the DC torque level, they must also compensate for the oscillating torque produced in the short circuited phase.

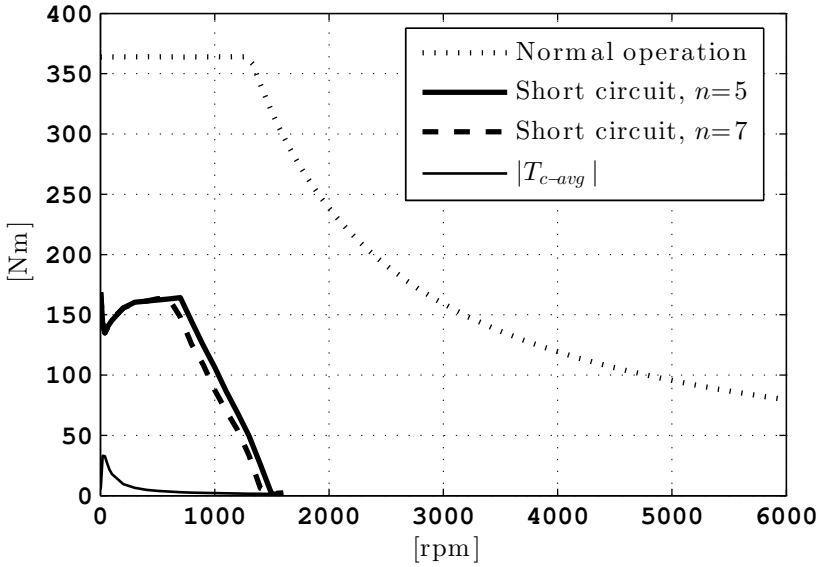

Figure 6.13: Torque speed characteristics of machine B during short circuit fault.

At a speed around 600-700 rpm, the braking torque, $|T_{c-avg}|$, is relatively low, the torque produced by the short circuited phase is just oscillating around zero. As a higher speed is reached before the torque must be reduced compared with the open circuit fault, it can be concluded that oscillating torque helps the remaining phases to maintain the DC torque level. For the strategy used, with the filtering of the ideal MTPA operating points, it is beneficial to utilize the positive part and to cancel the negative part of the oscillating torque compared to producing the whole DC torque level as in case of a open circuit fault. At least, if considering only the torque level at this particular speed.

6.2.3 Efficiency

The calculated efficiency map for machine B, interpolated over 81 operating points, when operated during phase open circuit fault can be seen in Figure 6.14. The operating points are calculated according to the numerical method presented in Section 3.2 (the per phase flux machine model), where harmonics up to n=7 are included in the phase currents. Each operating point (of input currents at a given speed) is simulated using transient FEA and the losses and torque at a given speed are calculated in the same way as presented in Section 5.3. Thus, the outer black line in the efficiency map shows the peak torque limited by current or voltage when n=7, calculated with the per phase flux machine model, and the efficiency map and the black points are results from the transient FEA. The efficiency during open circuit fault is lower compared with the normal operation, presented in Figure 5.12 in Section 5.3. This is expected since one third of the machine is somehow deactivated, while the remaining two thirds are pushed harder and harmonics are introduced to reduce the torque ripple.

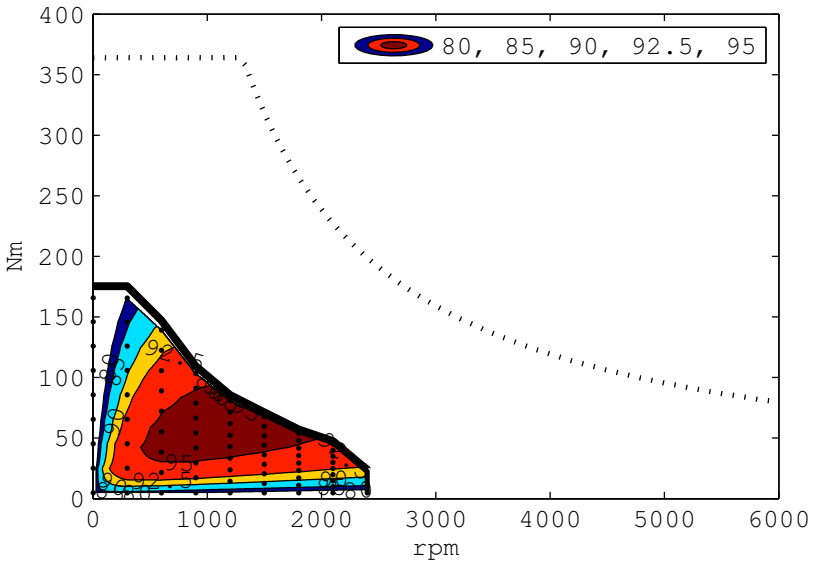

Figure 6.14: Efficiency map of machine B during open circuit operation.

The calculated efficiency map of machine B, when operated during short circuit fault, is presented in Figure 6.15. It is interpolated over 90 operating points and harmonics up to n=7 are included in the phase currents, which are simulated using transient FEA. The efficiency when operating during short circuit fault is even lower than in the case of an open circuit fault, which is expected since there are additional losses in the short circuited phase and the remaining

phases are pushed even harder. One can also observe a discrepancy of about 6 % in the maximum torque between the per phase flux machine model and the transient FEA. The discrepancy could be caused by both the fact that the phases are not completely decoupled and the discretization of the per phase flux machine model.

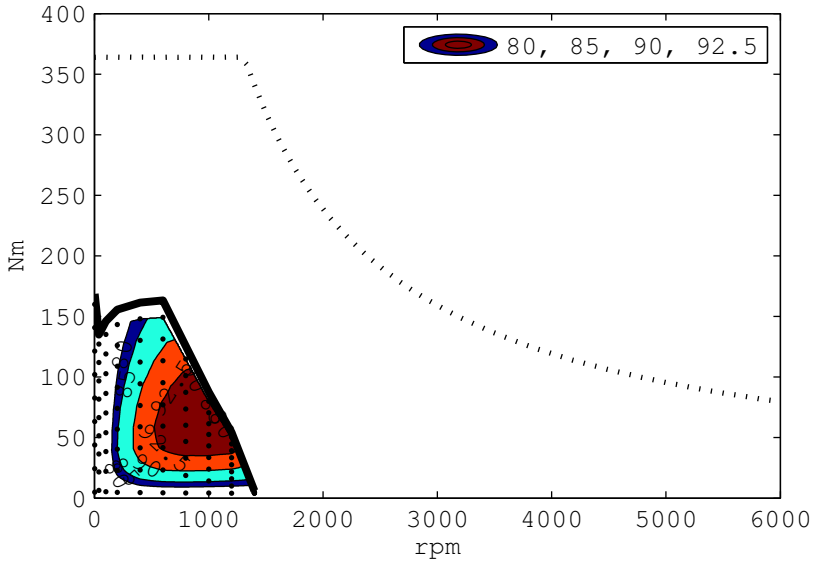

Figure 6.15: Efficiency map of machine B during short circuit operation.

6.3 2D modeling of MMF harmonic content and losses on the rotor side

In Figure 6.16, the harmonic content in magnetic field over the air-gap, and the flux and current on the rotor side are shown. The amplitudes are calculated in two different ways and are normalized around their respective $f_{rn}/f = 2^2/_{11}$ component. The MMF harmonic content is calculated analytically in the same way as Figure 4.3 and Figure 4.4 are obtained. The radial component of the flux density, B_r, and the axial component of the current density, J_z, are calculated using FEA. B_r is extracted in a point close to the rotor surface and J_z is extracted 2 electrical degrees from a PM edge. It is clear that the analytically predicted harmonic content is seen also in the FEA. The individual amplitudes of the flux densities are not exactly the same as in the MMF wave, which is an expected result as the reluctance seen by different wave-lengths are not the same. In the same manner, the current path for different wave-lengths is not the same. From the result presented in Figure 6.16, it is not possible to directly determine which harmonics that create the highest losses, as they are only evaluated in single points. To divide the losses produced by different harmonics, each frequency component must be calculated and integrated separately over the whole surface of the 2D object of interest.

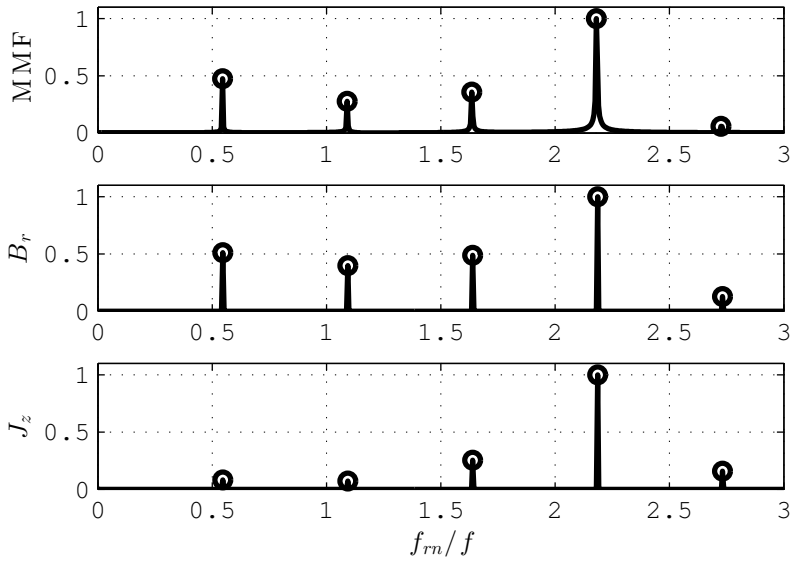

Figure 6.16: Harmonic content on the rotor side of machine B.

It should be mentioned that the induced eddy currents in the PMs flow in three

dimensional current paths and that 3D modeling is required for correct eddy current loss calculations. However, due to the difficulties associated with the computational time to solve the 3D problems with a reasonable mesh resolution and accuracy, the eddy current losses and segmentation of the PM have been studied in 2D only. In the FEA, the PMs are treated as solid objects with a certain bulk conductivity. Current can flow freely in the axial direction of a PM but the sum of the current in the axial direction of a single PM must be zero. Since it is defined as a 2D problem, it is not possible to segment the PMs in the axial direction. The PMs are therefore segmented in the circumferential direction only.

The total PM loss is calculated at the maximum torque at 14 different speeds, shown in Figure 6.17. It is clear that the PM losses are increased with both frequency and current, as the losses are lowered when the current is reduced due to the power limit at 1270 rpm. It can be seen that the very high total losses are reduced drastically when each PM is segmented into two parts. Even when going from two parts to three, the losses are reduced almost 50% while the difference in the last step is about 30 %.

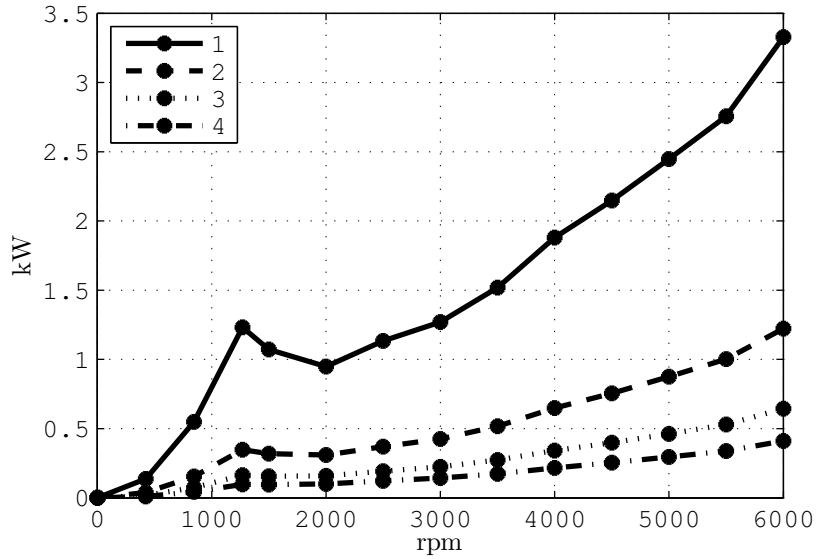

Figure 6.17: Total PM loss in machine B, when each PM consists of 1-4 equally sized pieces.

From Figure 6.17, it is obvious that the losses that are calculated in the non segmented PMs using 2D FEA is unrealistically high in a practical sense. The effi-

ciency map that is presented in Figure 5.12 in Section 5.3 using non segmented PMs, are therefore reproduced using segmented PMs. The efficiency map over machine B, when the PMs are divided into four equally sized pieces is shown in Figure 6.18. The maximum efficiency is achieved at a higher frequency compared with the previous case with solid PMs. It can also be noticed that the peak torque is reduced slightly due to the segmentation. The area corresponding to an efficiency above 97% is even larger than calculated for the 2004 Prius machine, presented in Figure 5.13.

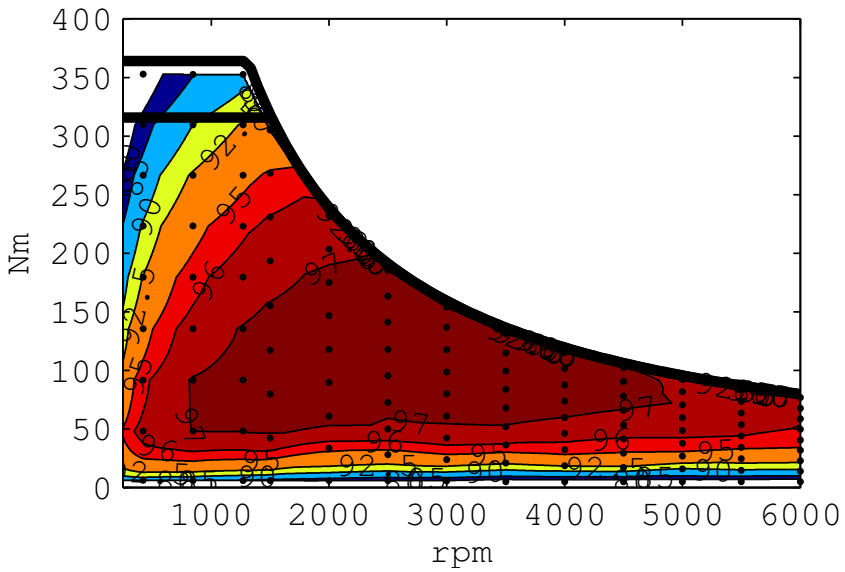

Figure 6.18: Interpolated efficiency map of machine B, when the PMs are divided into four equally sized pieces.

6.4 Loss components comparison

In this section, the different loss components of machine B during normal and during phase open circuit operation are presented and compared. The loss components are calculated using 2D FEA in the same manner as previously in the chapter, but a few adjustments have been made. From section 6.3, it is clear that the permanent magnets have to be segmented to reach reasonable loss levels. Therefore, the model with the permanent magnets segmented in four equally sized pieces in the circumferential direction is used. The same phase RMS current (250 A_{RMS}) and the same phase peak voltage (318 V) are kept, but the power limitation associated with the DC-link of the Prius 2004 drive system is removed. This is done in order to better show the thermal limitation of the machine, as the losses from this section is used for thermal analysis of the machine, in Chapter 9. During open circuit operation, only the fundamentals are present in the two phase currents of the same amplitude and oriented 60 electrical degrees apart and the voltage limits are calculated based on the highest phase voltage. The different phase voltages are visualized in Chapter 8.

6.4.1 Torque speed characteristics

In Figure 6.19, the torque speed characteristics for three different current levels without the power limitation at 50 kW can be seen. It can be observed that the 250 A_{RMS} curve in Figure 6.19b gives a low speed torque that is much closer the theoretical $364/\sqrt{3}$=210 Nm compared to what is obtained with current harmonics, as introduced in Figure 6.12. Also the speed range is increased substantially. It can further be seen that the torque at 200 rpm is reduced by approximately 50% when introducing current harmonics in order to reduce the torque ripple.

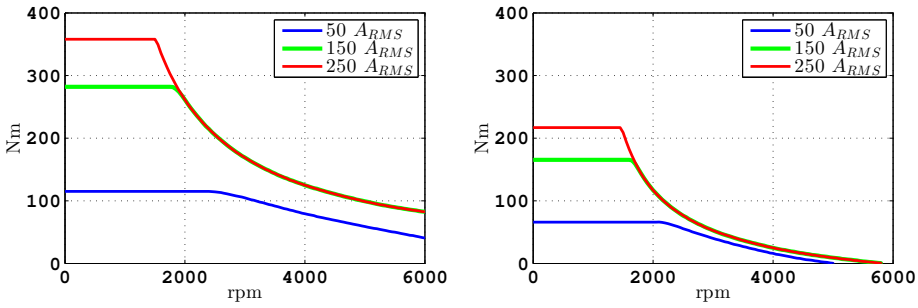

(a) Normal operation.

(b) Single phase open circuit operation.

Figure 6.19: Torque speed characteristics for different phase currents.

6.4.2 Loss components and efficiency

The total losses during normal and phase open circuit operation are shown in Figure 6.20. By comparison between Figure 6.20a and Figure 6.20b, a loss increase depending on torque level can be observed but there is no distinct loss increase related to the speed.

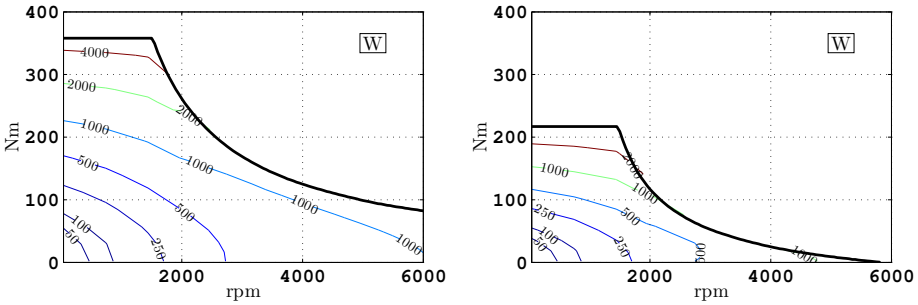

(a) Normal operation.

(b) Single phase open circuit operation.

Figure 6.20: Total loss as function of speed and torque.

The calculated copper losses during normal and open circuit operation are presented in Figure 6.21. By a visual comparison between Figure 6.21a and Figure 6.21b, it can be seen that the copper losses are approximately twice as high during open circuit operation for the same torque level. This is expected according to

$$\frac{P_{Cu,open}}{P_{Cu,normal}} = \frac{2R_s I^2_{RMS,open}}{3R_s I^2_{RMS,normal}} = \frac{2R_s(\sqrt{3}I_{RMS,normal})^2}{3R_s I^2_{RMS,normal}} = 2 \tag{6.1}$$

where the current during open circuit operation must be increased by a factor $\sqrt{3}$ in order to achieve the same torque level, $I_{RMS,open} = \sqrt{3}I_{RMS,normal}$. However, it is likely that the difference will be even greater, if also the thermal influence on the phase resistance is considered.

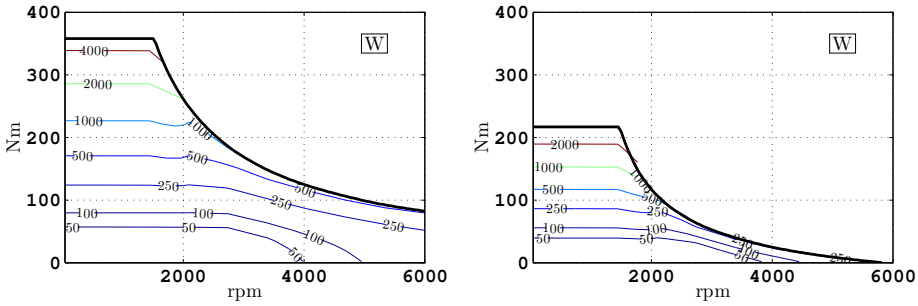

(a) Normal operation.

(b) Single phase open circuit operation.

Figure 6.21: Copper loss as function of speed and torque.

The iron losses as function of torque and speed can be seen in Figure 6.22. At lower speeds, the levels are more or less identical but an increase during phase open circuit operation at higher speeds can be noticed.

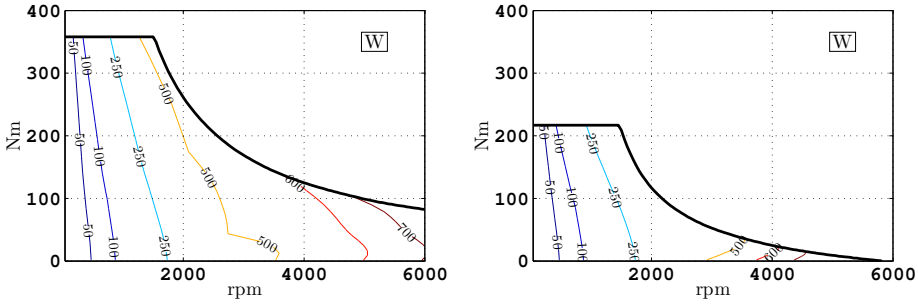

(a) Normal operation.

(b) Single phase open circuit operation.

Figure 6.22: Iron loss as function of speed and torque.

The permanent magnet losses during normal and phase open circuit operation are shown in Figure 6.23. By a visual comparison of Figure 6.23a and Figure 6.23b, it can actually be seen that the permanent losses tend to be slightly lower during open circuit operation than during normal operation.

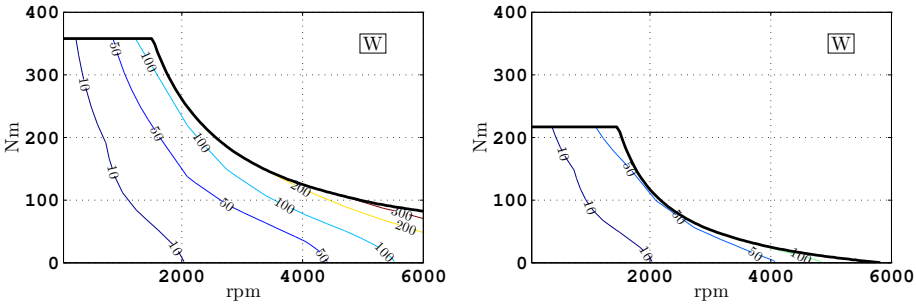

(a) Normal operation.

(b) Single phase open circuit operation.

Figure 6.23: Permanent magnet loss as function of speed and torque.

The calculated efficiency map during open circuit operation is presented in Figure 6.24. It can be compared directly with Figure 6.18, as the area of power limited operating points is beyond the possible operating points during phase open circuit operation. The area corresponding to at least 95% efficiency in Figure 6.24 is similar to the area corresponding to at least 97% efficiency in Figure 6.18. A greater difference ca be observed for lower speeds and higher torque, mainly due to the higher copper losses during phase open circuit operation.

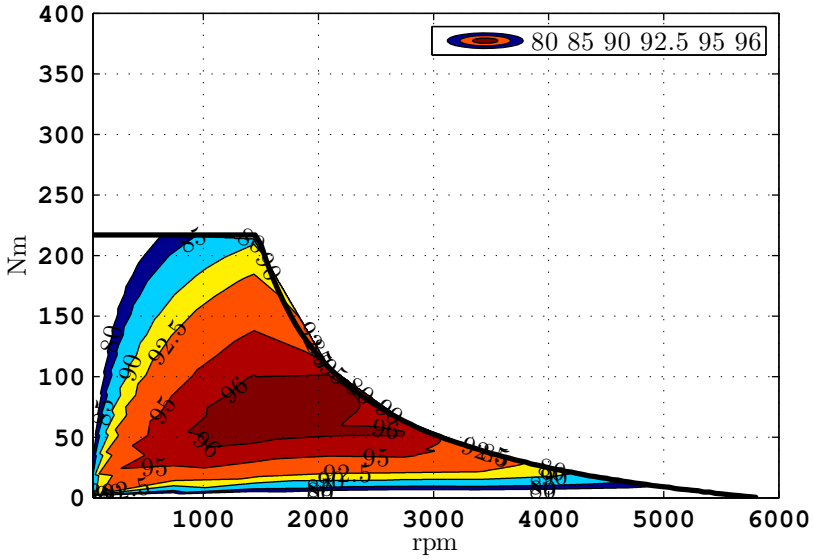

Figure 6.24: Efficiency map of single phase open circuit operation.

Chapter 7

The experimental IPM machine

This chapter introduces the experimental IPM machine that has been prototyped and evaluated in the lab as a part of this PhD project. The work with the design of the experimental IPM machine was started in the very beginning of the project with the original purpose to verify loss calculations and thermal calculations, and thus it was not designed to be a fault-tolerant machine. For example, this design cannot withstand a phase short circuit fault continuously but it can be operated during an open circuit fault, as most three phase machines actually are able to. Further, the introduction of sensors for continuously monitoring of temperatures on the rotor side complicated the interfaces between the electromagnetic and the mechanical part of the design severely and delayed the delivery of the machine.

In the first sections of this chapter, the geometry and the material data are presented together with the integrated thermal measurement system , which was designed and developed in close conjunction with the electromagnetic design of the machine. In the later sections, some characteristics, calculated by means of FEA, and some base verifications measured in the lab are presented.

7.1 Design specification

The machine data for the IPM design is presented in Table 7.1, where the amount of copper has been calculated based on electrical resistance measurements together with the wire diameter of 1.4 mm. Nominal speed and phase voltage is calculated based on an available DC-link voltage of 300 V. The phase current is given in an interval, since two methods are used to calculate winding temperature and they result in slightly different values. The two methods are presented

in section 7.3.1 and section 9.3.1. The continuous output power, which of course is related to the phase current, is approximately 4 kW for these currents.

Table 7.1: Machine data of the IPM design.

Parameter	**value**
Mass of active parts	22.30 kg
Mass of NdFeB magnets	0.89 kg
Mass of copper	2.35 kg
Mass of electrical steel rotor	7.63 kg
Mass of electrical steel stator	11.43 kg
Maximum speed	3000 rpm
Nominal speed	750 rpm
Phase voltage	106 V_{RMS}
Phase current	13.5-15 A_{RMS}
Continuous output power	≈4 kW
Average phase resistance @ 19.20°C	620 mΩ
Direct axis inductance, L_d	22 mH
Quadrature axis inductance, L_q	34 mH

7.1.1 Geometry

The active parts of the IPM design is shown in Fig. 7.1, it has three pole-pairs and nine slots wound with concentrated windings.

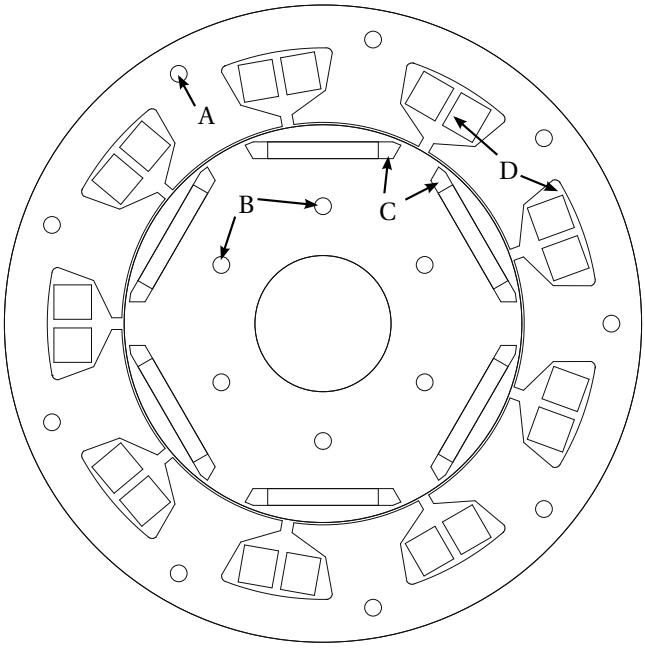

Figure 7.1: Geometry of the IPM design, where the locations of the temperature sensors are marked out, A-D.

Holes for temperature sensors (5 mm in diameter) have been introduced in the stator (A) and rotor (B) lamination stacks during the electrical discharge machining manufacturing process. The holes are positioned directly behind the stator teeth and the permanent magnets in order to limit the impact on the flux distribution compared to a design without the holes.

Some of the air-pockets beside the permanent magnets (C) are also utilized to place temperature sensors. Finally, a number of sensors are placed on/in the windings inside the slots (D) and also in the end windings (not shown in the 2D illustration). In total, 32 sensors have been placed in different axial depths inside the machine, 16 on the rotor and the stator side respectively.

Key design parameters of the prototyped IPM are presented in Table 7.2.

Table 7.2: Geometrical data of the experimental IPM design.

Parameter	value
Outer stator diameter	190 mm
Rotor diameter	118.6 mm
Shaft hole diameter	40.6 mm
Sensor hole diameter	5 mm
Air-gap length	0.7 mm
PM thickness	5 mm
PM width	33 mm
Stack length	120 mm
Number of stator slots	9
Yoke thickness	12.8 mm
Toot width	22.6 mm
Shoe height, inner	9.6 mm
Shoe height, outer	3.0 mm
Slot opening width	3.5 mm
Slot area	481 mm^2
Number of pole pairs	3
Number of turns	48 per tooth
Wire diameter	1.4 mm

7.1.2 Material data

The material data used for the models of the experimental IPM machine is presented in Table 7.3. It should be pointed out that the values may not reflect the exact alloy compositions of the materials in the machine, as this was not known. Another uncertainty is the PET film, which consists of a solid PET film covered by PET fleece (containing a lot of air) on both sides. Ideally, the PET fleece should be completely soaked by the winding impregnation material. According to the manufacturer of the PET film, the heat conductivity has to be determined for the combination of the materials by measurements.

In addition to the machine parts, two more materials are listed in the bottom of Table 7.3: the Armaflex sheet insulation that is covering the machine housing in order to minimize the convective heat coupling to the room, and the 2 mm bakelite sheet, which is used to reduce the conductive heat transfer via the mounting flange.

Table 7.3: Material data used for the models of the experimental IPM machine.

Machine part	**Material**	**Density** (kg/m^3)	**Heat conductivity** (W/(m·K))	**Specific heat capacity** (J/(kg·K))
Lamination	M310-50A	7650	28	471
Winding	Copper (Cu)	8933	400	391
Shaft	Steel	8043	60.5	476
Magnets	N35SH	7500	-	502
Winding impregnation	varnish	-	-	-
Slot insulation	PET film	-	-	-
Insulation envelope	Armaflex 25 mm	-	⩽0.045 @ 40°C	-
Flange insulation	Bakelite 2 mm	-	0.2	-

7.2 Integrated thermal measurement system

In this section, the design of the temperature measurement system on the rotor side is presented, but the same system is used on the stator side as well. The only difference is that the wireless transmission is replaced by wired transmission with optocouplers.

A schematic illustration of the IPM machine, together with the temperature measurement system attached on the shaft on the backside of the machine, is shown in Figure 7.2. As can be seen in Figure 7.2, the shaft has been made hollow from the left-hand side into the first rotor surface, this is done in order to get access to the sensors in the rotor from the end of the shaft. An infrared transmitter/receiver is located concentric to the shaft and pointing in the axial direction providing online data while the rotor is rotating.

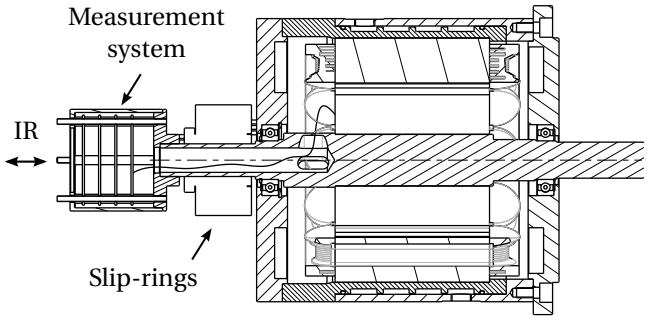

Figure 7.2: Cross-sectional view of the IPM design together with the temperature measurement system on the rotor-shaft.

For the DC power supply of the measurement system on the rotor side, it was decided to use a slip-ring unit to avoid battery replacement during an ongoing experiment and also to lower the rotating mass mounted in the end of the shaft.

Micro controller unit

A low cost 8-bit micro controller unit (MCU), ATmega128A [49], is used and its program is developed in C-code. This simple and cheap MCU is fast enough, it has plenty of pins and counters to run both sensor readings and the IR communication fully interrupt based. In addition to the program, its memory houses a 30 sample buffer for each of the 16 temperature channels at the rotor and the stator respectively (30 seconds of temperature recording of all channels at 1 Hz sample rate).

Digital sensors

A great advantage of the digital sensors used, DS18B20, is that no calibration of the sensors is necessary if the specified accuracy of $\pm 0.5^{o}$C in the range from -10^{o}C to +85^{o}C is sufficient [50]. They can be connected directly to a digital input/output (I/O) pin on the MCU. The only external component required is a single pull-up resistor and the temperature is read serially.

However, this simplest configuration means that an (I/O) pin of the MCU is stiffly connected to the sensor wire, which in turn is placed in the electromagnetically noisy environment inside the machine. To protect the MCU and increase the immunity towards EMI, a bidirectional digital isolation device, ADuM1250 [51], was introduced between the MCU and the sensor which is shown in Figure 7.3. The isolation device has two isolated bidirectional channels and two sensors were connected to each device, but only one is shown in Figure 7.3.

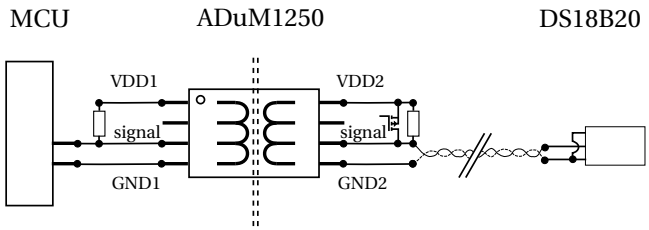

Figure 7.3: Digital sensor connection diagram.

Further, it was decided to utilize the "parasite-powering" feature of the sensor, which means that the sensor is supplied via the signal wire during the temperature readings. To ensure that the sensor has sufficient supply during the temperature conversion, a p-channel MOSFET is connected over the sensor side pull-up resistor to provide a strong pull-up. In this configuration, only two wires are needed and a twisted pair is used for each sensor to further increase the EMI immunity.

Analog sensors

The analog PT1000 temperature sensors were all connected via twisted pair wires to a small package differential input instrumentation amplifier, AD8236 [52], see Figure 7.4. The main purpose of the instrumentation amplifier is to amplify the sensor signal and adjust it to a suitable range for the MCU AD-converter but also to increase the input impedance of the measurement circuit. In that sense, especially together with its input filter, it also works as a protective device for the MCU and the rest of the measurement system.

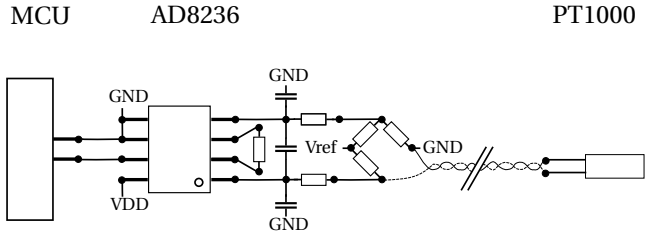

Figure 7.4: Analog sensor connection diagram.

Wireless data transmission

The wireless data transmission is based on an IR receiver module for remote control systems, TSOP75256WTR [53], and light emitting diodes (LEDs), which are modulated with a carrier frequency of 56 kHz. The IR receiver is placed concentric to the shaft and surrounded by four IR LEDs, as marked out in Figure 7.5.

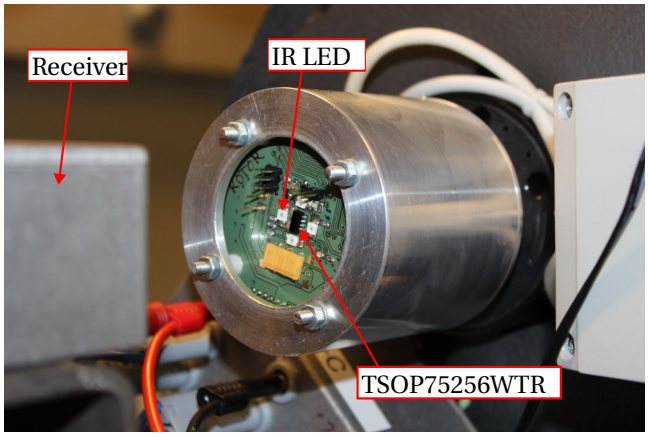

Figure 7.5: The temperature measurement system mounted on the IPM shaft.

Ten pulses at 56 kHz is the minimum number of pulses in a burst, which is shown in Figure 7.6. This gives theoretically an available data transmission bandwidth of 5.6 kbit/s if each bit is represented by a burst. Data corresponding to the reading of each of the 16 sensors on the rotor side is represented by 2 bytes and the sample frequency is 1 Hz. Hence, the theoretic data rate needed is $16 \cdot 2 \cdot 8 = 256$ bit/s, which is about 5% of the theoretically available data transmission bandwidth only. The remaining 95% can be used for: command bytes, indexing, checksums, retransmissions etc. and it results thereby in a reliable data transfer.

t

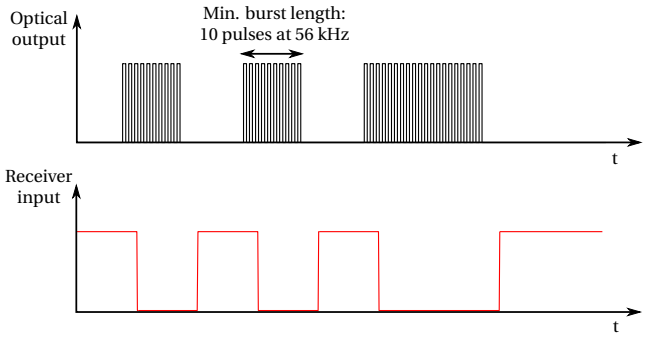

Figure 7.6: The IR transmitter/receiver signals.

Data collection

From the receivers, the temperature data was collected to a PC using RS-232. The "OpenFormat Zero Sensor" device configuration in the donation-ware "LogView Studio" [54] was easily implemented for live visualization and database storage of temperature data.

7.2.1 Sensor map

The individual locations of the sensors are shown in Figure 7.7, where "middle" means that the sensor is mounted in the middle of the lamination stack and the presented distances are given referred to the bottom or the top of the lamination stacks. Top corresponds to the side where the measurement system is mounted (the left hand side in Figure 7.2) and bottom corresponds the side where the load is attached (the right hand side in Figure 7.2). Additionally, there are three sensors positioned on/in the end windings and three in the slots, which are also shown in Figure 7.7.

Apart from that, the location of the water inlet and outlet is illustrated in Figure 7.7. There is also a displacement of the water inlet and outlet in the axial direction, where the inlet is positioned corresponding to the top of the lamination stack and the outlet is positioned corresponding to the bottom of the lamination stack.

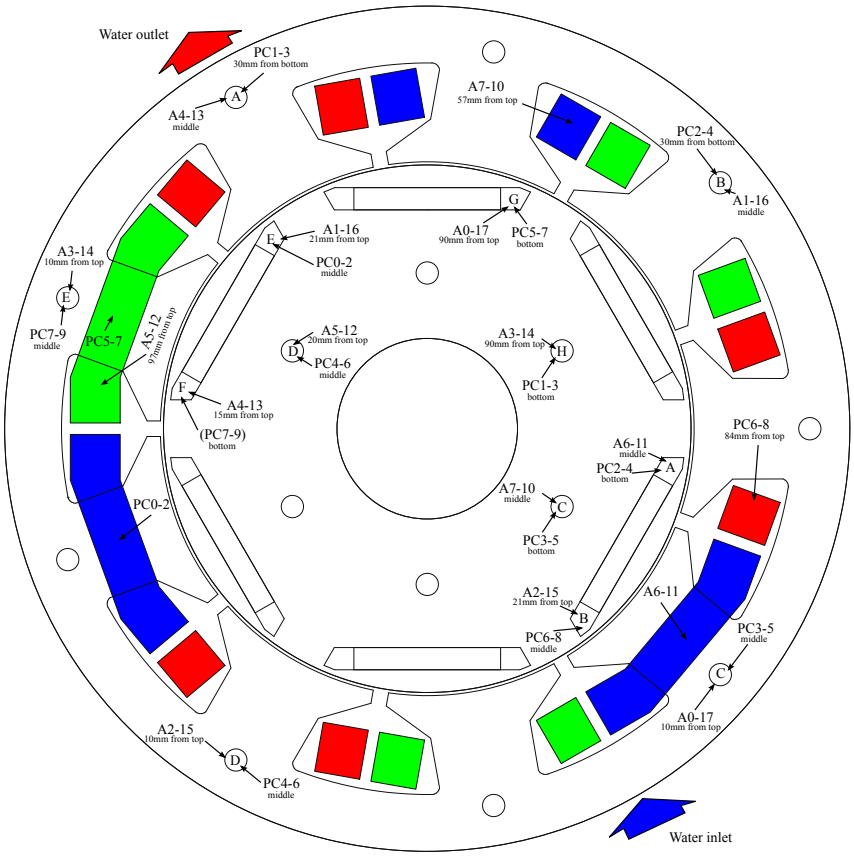

Figure 7.7: Sensor map showing positions of all the 32 sensors mounted in the machine, the phases A-B-C are represented by the colors R-G-B.

7.3 Estimation of the thermal properties inside the slot

As already mentioned in section 7.1.2, there is an uncertainty regarding the thermal conductivity of the PET film slot liner, which does not have a homogeneous structure. Furthermore, it is clear that the individual strands in the winding are not evenly distributed over the whole slot. This is why an air pocket is introduced into the slot of the simplified 2D FEA model that is used for calibration of the thermal properties in the slot, see the red rectangles in Figure 7.8.

The green area in Figure 7.8, representing the approximate locations of the strands, is 189 mm^2. Together with the 48 turns per tooth and the wire diameter of 1.4 mm, this gives an effective fill-factor of 39% in that area. For an impregnation mate-

rial with a thermal conductivity of 0.2 W/(m·K), an equivalent thermal conductivity of the winding mix material of 0.26-0.46 W/(m·K) is expected according to Figure 1.11. In order to reach a desirable accuracy, the FEA model is used to calibrate the thermal conductivity of both the slot liner and the equivalent winding mix material.

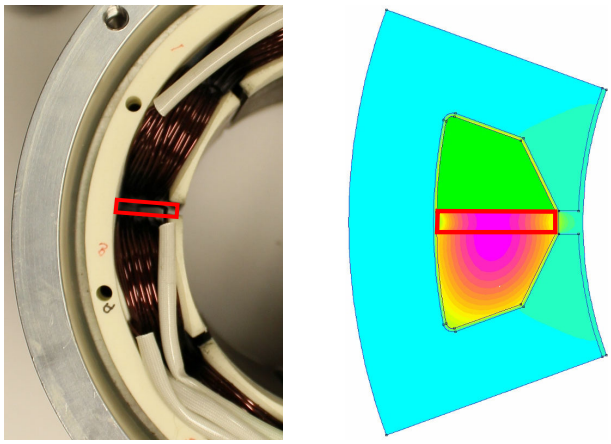

Figure 7.8: The simplified 2D geometry used to calibrate the thermal properties of the slot with respect to measurements. An air pocket is introduced in the middle of the slot for better representation of the actual distribution of the wires in the slot.

Two measurement series of about four hours each were carried out in the lab. The data presented in Table 7.4 represents average temperatures when the machine is close to thermal steady-states. During the measurements, a DC-current source is connected to the DC-link of the converter which switches the phase connected to the positive DC-link terminal every 20th second, the remaining two phases are connected to the negative terminal. This is done in order to get a well defined and evenly distributed power injected to the windings. The average winding temperatures are based on the resistance measurements.

Table 7.4: Measured data used for estimation of the thermal properties inside the slots.

	Measurement 1	**Measurement 2**
Rotor temp.	14.6°C	40.0°C
Stator temp.	9.4°C	35.9°C
Ph A temp.	71.8°C	94.4°C
Ph B temp.	75.9°C	98.0°C
Ph C temp.	72.4°C	96.1°C
Winding avg temp.	73.4°C	96.0°C
Copper losses	255 W	275 W

The measured rotor and stator temperatures in Table 7.4 are assigned to the rotor boundary and the outer stator boundary of the model in Figure 7.8 respectively. Insulation boundaries are used on the symmetry boundaries, the middle of the two teeth in Figure 7.8. A loss density, calculated based on the measured copper losses is assigned homogeneously to the two winding mix domains inside the slot.

In Figure 7.9, the combination of conductivities that give a match between the calculated average winding mix temperatures and the corresponding measured average winding temperatures are represented by a line for each measurement. There is no perfect combination of thermal conductivities for the winding mix and the slot insulation, as there is no intersection between the two curves. The reason could simply be that it is not possible to find a perfect match between the real 3D geometry of the machine and the proposed 2D model in Figure 7.8. Anyhow, if the least square error is calculated according to

$$min(E) = min\left(e_1^2 + e_2^2\right) = min\left(\left(T_{FEA1} - T_{Meas.1}\right)^2 + \left(T_{FEA2} - T_{Meas.2}\right)^2\right) \quad (7.1)$$

the point (0.0430, 0.378) is found. This thermal conductivity of the winding mix, 0.378 W/(m·K), agrees very well with the 0.26-0.46 W/(m·K) found in Figure 1.11 previously. According to the data sheet, the thickness of the PET film is 0.21mm. If it is considered to be solid with a thermal conductivity of 0.2 W/(m·K), then the 0.5 mm thick slot insulation of 0.0430 W/(m·K) in the 2D model is equivalent to an additional 0.02 W/(m·K) air gap of 0.21 mm added to the solid PET film. Considering these values, there exists at least a reasonable physical representation that corresponds to the 2D model.

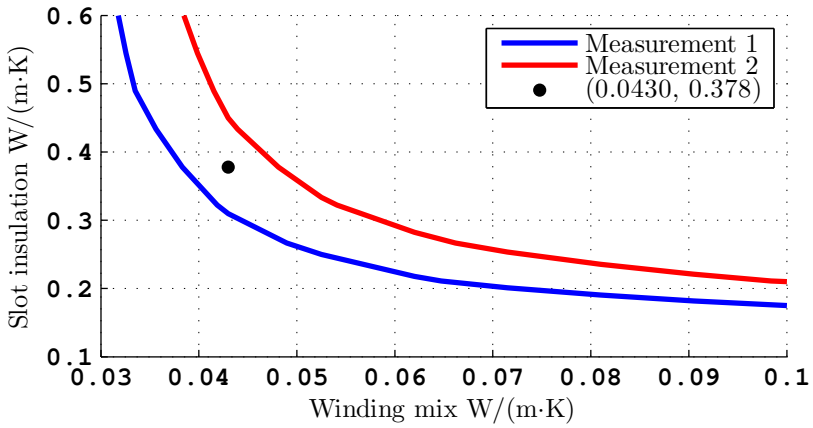

Figure 7.9: The combination of thermal conductivities that give the same temperature in the FEA as in the measurements.

7.3.1 Thermal limit due to the heat transfer from the winding

The simplified 2D model, previously presented in Figure 7.8, is used to calculate the winding temperature as function of the phase RMS current as well. The thermal conductivities of the winding mix and the slot insulation was put to 0.378 W/(m·K) and 0.043 W/(m·K) respectively, according to the previous section. The rotor boundary was put to insulation and the stator boundary was fixed to 20°C. For each current level, the phase resistance and hence the copper losses are updated based on the calculated average winding temperature, T_{AVG}, until a steady-state is reached. The maximum winding temperature, T_{MAX}, which is of interest when determining the thermal limit of the machine is shown together with the average temperature in Figure 7.10.

The black dot in Figure 7.10 shows that the calculated maximum winding temperature of 180°C is reached for a phase current of 13.5 A_{RMS}, when the copper losses and a constant outer stator boundary temperature of 20°C are considered. Furthermore, the three dashed lines indicate current levels that are of interest later on in the thesis.

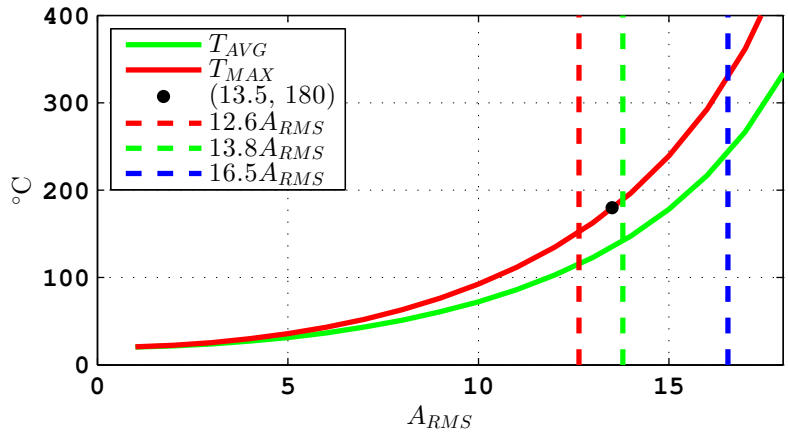

Figure 7.10: Calculated winding temperature as function of the RMS phase current, the dashed lines indicate current levels that are of interest later on in the thesis.

7.4 Calculated properties of the experimental machine

In this section, the calculated torque speed characteristics and the different loss components together with the efficiency of the experimental IPM machine are presented. The loss components are calculated in the same manner as in section 5.3 previously. The measured average phase resistance, given in Table 7.1, has been recalculated for a winding temperature corresponding to 120°C using (1.38). The efficiency is calculated according to (5.3) in section 5.3.

7.4.1 Torque speed characteristics

The calculated torque speed characteristics for three different phase current levels both during normal operation and during single phase open circuit operation are presented in Figure 7.11. During open circuit operation, the currents are arranged and the voltages are calculated in the same manner as in section 6.4.

The current limited torque is reduced, almost exactly, by a factor $1/\sqrt{3}$ during single phase open circuit operation and the field weakening region starts at approximately the same speed in both cases. For the lower current levels during single phase open circuit, there is a significant reduction of the field weakening range, from 2690 rpm to 1590 rpm in case of 10 A_{RMS} and from 3000 rpm to 2230 rpm in case of 15 A_{RMS}.

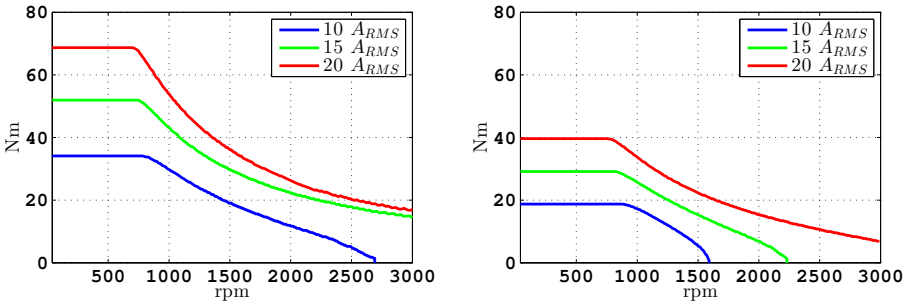

(a) Normal operation.

(b) Single phase open circuit operation.

Figure 7.11: Torque speed characteristics for different phase currents.

7.4.2 Loss components and efficiency

The total loss distributions are shown in Figure 7.12, where the losses during single phase open circuit operation are increased both with torque and with speed. For low speeds, the losses are approximately twice as high during phase open circuit operation for the same torque.

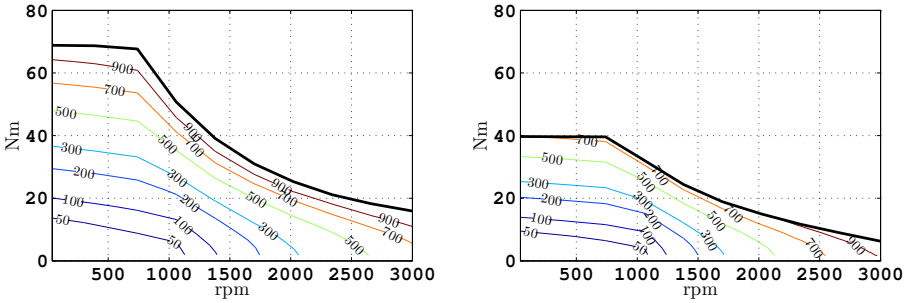

(a) Normal operation.

(b) Single phase open circuit operation.

Figure 7.12: Total loss as function of speed and torque.

The calculated copper losses during normal and open circuit operation are presented in Figure 7.13. By a visual comparison between Figure 7.13a and Figure 7.13b, it can be seen that the copper losses are approximately twice as high during open circuit operation for the same torque level. Which is expected and was also shown in Figure 6.21 in section 6.4.

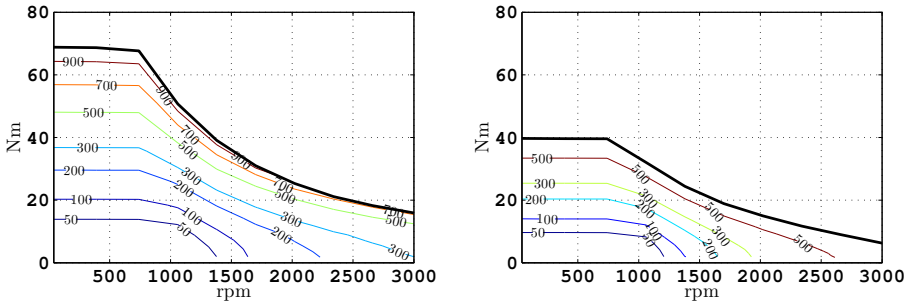

(a) Normal operation.

(b) Single phase open circuit operation.

Figure 7.13: Copper loss as function of speed and torque.

The iron loss distributions are shown in the torque speed diagrams in Figure 7.14. The loss levels are low compared with the copper losses presented in Figure 7.13, and there is hardly no difference between normal and single phase open circuit operation.

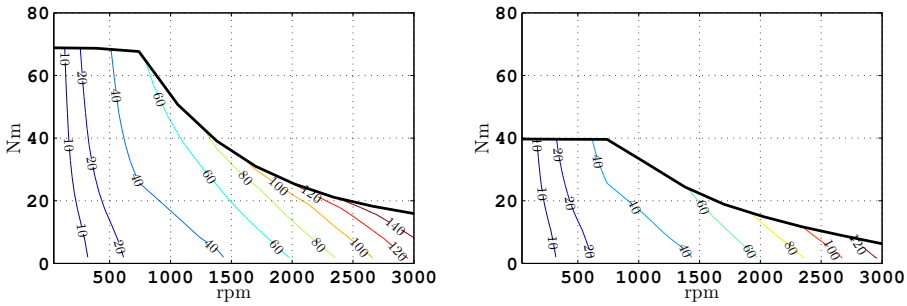

(a) Normal operation.

(b) Single phase open circuit operation.

Figure 7.14: Iron loss as function of speed and torque.

The calculated permanent magnet loss distributions are presented in Figure 7.15. As with the iron losses, the permanent magnet losses are more or less the same both during normal operation and during single phase open circuit operation.

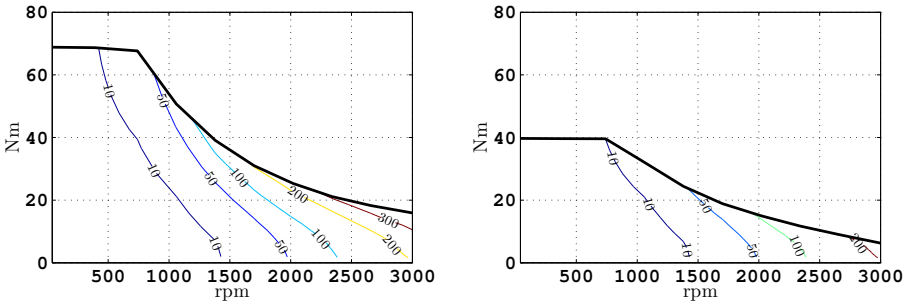

(a) Normal operation.

(b) Single phase open circuit operation.

Figure 7.15: Permanent magnet loss as function of speed and torque.

The calculated efficiency maps for normal operation and single phase open circuit operation are shown in Figure 7.16 and Figure 7.17 respectively. For normal operation, there is an area with at least 92.5% which is located relatively far down in the map due to rather high copper losses. The map of the efficiency during single phase open circuit operation shows a somewhat similar appearance but a generally lower efficiency. For instance, the area with at least 85% efficiency in Figure 7.17 matches the area with at least 90% efficiency in Figure 7.16 quite well.

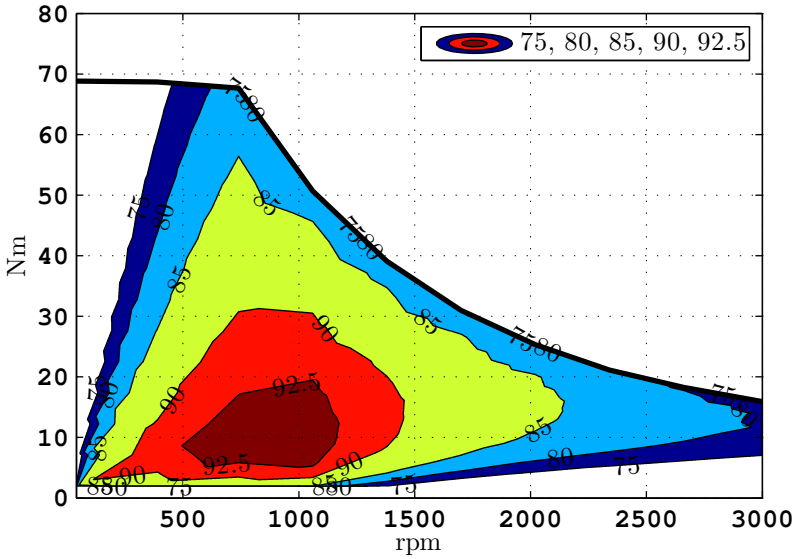

Figure 7.16: Efficiency map of normal operation.

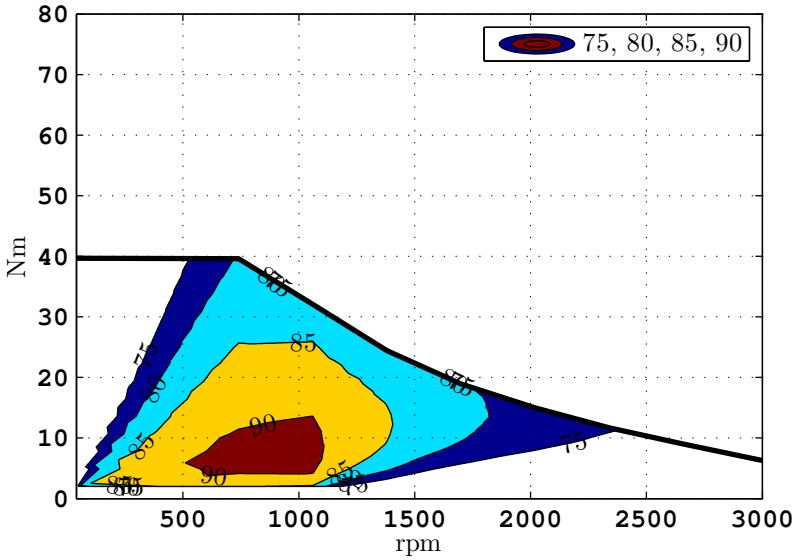

Figure 7.17: Efficiency map of single phase open circuit operation.

7.5 Measured properties of the experimental machine

In this section, base verifications of the winding resistance and the short circuit characteristics of the experimental IPM machine is carried out. The short circuit characteristics are measured both for three phase and single phase short circuits, and they are presented and compared with the corresponding FEA.

7.5.1 Winding resistance and temperature calibration

The winding resistance is measured using the power analyzer with a DC-current of approximately 1 A fed through the Y-connected phases (i_a=−2i_b=−2i_b). The measured phase resistances and their average resistance are presented in Figure 7.18a. All the resistances are fairly constant over the five minutes of measurements. The greatest difference between the highest and the lowest values (phase C and phase B) is less than 2%. When observing Figure 7.18a carefully, it can be observed that the resistance in the windings carrying the lower current (phase B and phase C) tend to decrease slightly while the resistance in the winding carrying the higher current (phase A) tends to increase slightly.

In order to measure the winding or the phase resistances with a well defined winding temperature, the measurements are carried out after the machine is left at rest overnight. The measured winding temperatures, together with the average winding temperature, are shown in Figure 7.18b. The measured winding temperatures are all within an interval of less than 0.4°C and the average temperature is fairly constant around 19.2°C, but a slight temperature increase during the measurements is present.

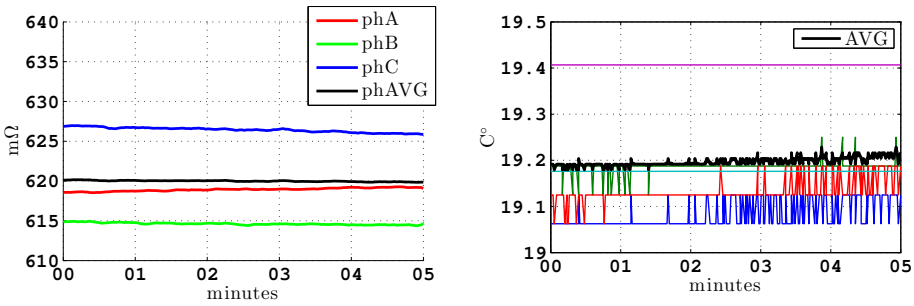

(a) Resistance.

(b) Temperature.

Figure 7.18: Measured winding resistances and measured average winding temperature.

The average of the measured winding resistances at the measured average temperature of 19.20°C are collected in Table 7.5. The individual values are used for winding temperature calculations based on resistance measurements only. In

all other cases, the phase resistance is considered to be 620 mΩ at an average winding temperature of 19.20°C in all the three phases.

Table 7.5: Measured average winding resistances during 5 minutes at an average temperature of 19.20°C

Resistance	**mΩ**
Phase A	619
Phase B	615
Phase C	626
Average	620

7.5.2 Short circuit characteristics

From (2.13) and (2.14), the currents for a balanced three phase short circuit can be found directly in the third quadrant ($i_d < 0$ & $i_q < 0$) of the $\Psi_d(i_d, i_q)$ and the $\Psi_q(i_d, i_q)$ maps, by solving

$$\begin{cases} 0 = u_d = R_s i_d - \omega \Psi_q \\ 0 = u_q = R_s i_q + \omega \Psi_d \end{cases} \tag{7.2}$$

for each mechanical speed of the machine. However, the solutions to (7.2) are very sensitive to the machine parameters and the interpolation methods used for the $\Psi_d(i_d, i_q)$ and the $\Psi_q(i_d, i_q)$ maps. Therefore, the solutions to (7.2) are used as initial conditions when a new set of transient FEA are carried out to calculate the currents at each short circuit operating point.

The measurements in the lab were started at 10 rpm and the speed was increased in steps of 10 rpm, while the phase currents and the winding temperatures were carefully observed. Both in case of single and three phase short circuit, the experiment was interrupted when the hottest monitored winding temperature exceeded 100°C, which occurred at around 160-170 rpm in both cases. In these points, the single phase short circuit current was measured to 13.8 A_{RMS} and the three phase short circuit current to 12.6 A_{RMS}. Both these current levels are marked out in Figure 7.10 in section 7.3.1 where it can be seen that steady-state temperatures of more than 100°C are to be expected. The limit of 100°C was used in order to be on the safe side regarding winding temperature, as the sensor may not be reflecting the hottest spot of the winding and there could also be a considerable thermal time constant in between the hotspot and the sensor.

In Figure 7.19, the calculated currents are represented by the dashed lines and the measured currents by the dots connected by the solid lines. Currents corresponding to speeds of 20, 50, 100 and 160 rpm are marked out by the four black

dots on each curve. It can be seen that the discrepancy between the measured and calculated curves increases as the speed and also the winding temperature increase during the measurements. The black dots furthest to the left in the figure corresponds to the last measured point, when the monitored temperature exceeded 100°C at 160 rpm. After both the measured series, the machine has then been stopped and the winding temperature is cooled down to room temperature before the last operating point at 160 rpm is remeasured with a colder winding also. The remeasured currents with the colder winding are represented by the two blue "x" symbols in Figure 7.19. It can be seen that they are located approximately in the middle between the calculated points and the points measured with the hotter winding.

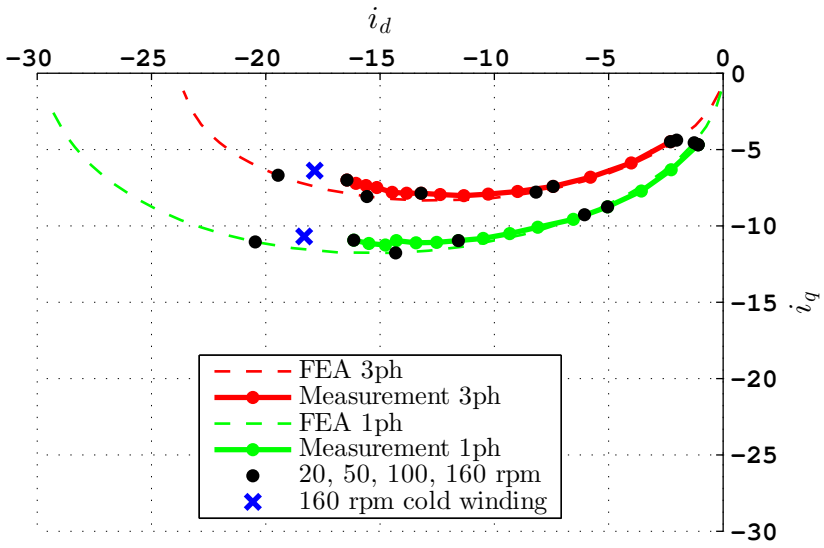

Figure 7.19: Measured and calculated 1ph and 3ph short circuits currents. The calculated currents are represented by the dashed lines and the measured currents by the dots connected by the solid lines. Currents corresponding to speeds of 20, 50, 100 and 160 rpm are marked out by the four black dots on each curve.

The torque production during three phase short circuit is shown in Figure 7.20, where the black dots are the measured values. The FEA has been carried out two times, considering average winding temperatures of 19°C and 100°C, which are represented by the solid blue and red line respectively. Regarding the measured values, it can be seen that the maximum breaking torque is achieved for a speed or frequency somewhere in between what is calculated for 19°C and 100°C, which is reasonable since the experiment starts at room temperature and ends at approximately 100°C. As in the previous figure, the remeasured torque

with the colder winding at 160 rpm is represented by the blue "x" symbols, which gives a measured torque close to the calculated value for a winding temperature of 19°C. However, there is also a 10% discrepancy regarding peak torque, following on the difference between the currents in the measurements and the calculations. One possible reason for the discrepancy is that the inductance is slightly higher in reality than in the 2D calculations, where the end-windings are not included. On the other hand, a homogeneous winding temperature of 100°C gives a 32% higher phase resistance than for a temperature of 19°C, which adds an uncertainty of the of the phase resistance value as well.

As a last step, the measured currents have been used to find the corresponding torque by means of the FEA map, which is shown by the green dots in Figure 7.20. The result indicates, as mentioned above, that the main discrepancy between the torque calculations and torque measurements is caused by the electrical part of the problem, i.e. (7.2).

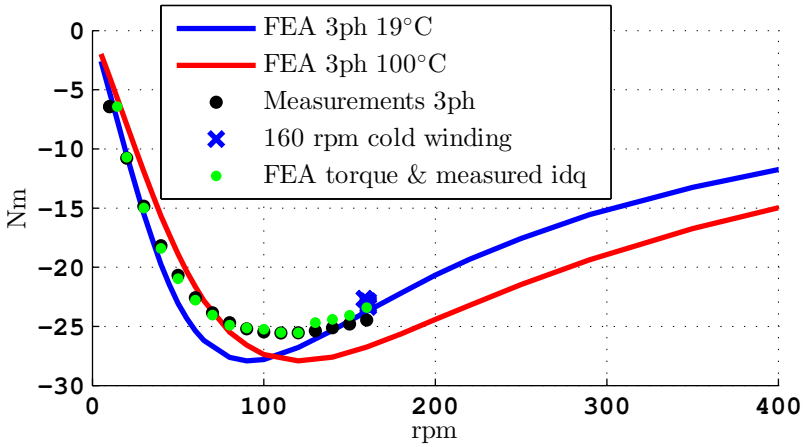

Figure 7.20: Measured and calculated 3ph short circuit torque.

The measured and the calculated torque during a single phase short circuit is shown in Figure 7.21. If only considering the first measurement series, the black dots, the maximum breaking torque is not found. The remeasured torque with the colder winding at 160 rpm, represented by the blue "x" symbols, gives a slightly lower torque than what is measured at 150 rpm. Thereby, the measurements indicate a maximum breaking torque below 160 rpm with a colder winding temperature.

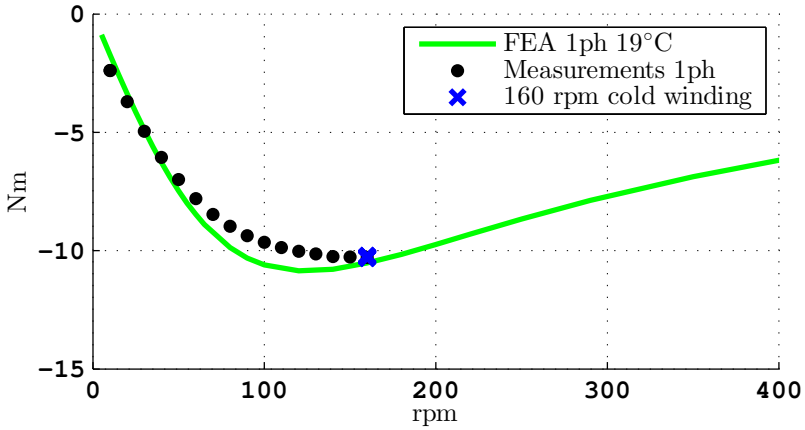

Figure 7.21: Measured and calculated 1ph short circuit torque.

Chapter 8

Theoretic performance in the $i_d i_q$ -plane

In this chapter, the fault-tolerant fractional slot machine and the two reference machines are evaluated, both during normal operation and open circuit operation in the $i_d\,i_q$-plane, where several different properties can be visualized in an efficient way at the same time. The chapter starts with an introduction of important characteristics that can be identified in the $i_d\,i_q$-plane, then follows the analysis of the three machines. The calculations are done by means of FEA, for each of the machines. For simplicity, only the fundamental frequency is considered and the phase resistance is neglected. Finally, the chapter is finished by some concluding remarks from the analysis in the $i_d\,i_q$-plane.

8.1 Characteristics in the $i_d i_q$ -plane

Considering the voltage limitation in the rotating dq reference frame, the maximum amplitude of the phase voltage can be expressed as

$$u_{max} = \sqrt{u_d^2 + u_q^2} \tag{8.1}$$

which during a steady-state, together with (2.7) and (2.8) when neglecting the phase resistance, gives the following limitation of operating points due to the maximum amplitude of the phase voltage in the $i_d\,i_q$-plane

$$\left(\frac{u_{max}}{\omega L_d}\right)^2 = \left(\frac{L_q}{L_d} i_q\right)^2 + \left(i_d + \frac{\Psi_m}{L_d}\right)^2 \tag{8.2}$$

that corresponds to the equation of an ellipse centered at $(-\Psi_m/L_d,0)$. The size of the ellipse is inversely proportional to the speed [55] and its ellipticity is defined by the ratio L_q/L_d. For a machine with surface mounted permanent magnets, where the inductance in the direct and quadrature axis are expected to be the same ($L = L_d = L_q$), (8.2) simplifies to

$$\left(\frac{u_{max}}{\omega L}\right)^2 = i_q^2 + \left(i_d + \frac{\Psi_m}{L}\right)^2 \tag{8.3}$$

which in turn corresponds to the equation of a circle centered at $(-\Psi_m/L,0)$ and with a radius, inversely proportional to the speed, defined by $u_{max}/(\omega L)$. Another interesting aspect, regarding the center-point of the circuit in the $i_d\, i_q$-plane, is that the short circuit current can be represented [56] as

$$I_{sc} = \frac{j\omega\Psi_m}{R_s + j\omega L} = \frac{\Psi_m}{R_s/(j\omega) + L} \approx \frac{\Psi_m}{L} \tag{8.4}$$

where the approximation above holds for high speeds as the phase reactance becomes much greater than the phase resistance. For a PMSM with different direct and quadrature axes inductances, the approximation above can be rewritten as

$$I_{sc} \approx \frac{\Psi_m}{L_d}, \tag{8.5}$$

see (2.7) and (2.8), where the short circuit current corresponds to the center-point of the ellipse in (8.2) as well. Observe that the short circuit currents determined by (8.4) and (8.5) in the rotating dq reference frame correspond to a balanced three phase short circuit and not a single phase short circuit, with the exception for low or null mutual inductance machine designs where a balanced three phase short circuit and a single phase short circuit result in the same phase currents.

8.2 The fault-tolerant fractional slot machine

8.2.1 Normal operation

Figure 8.1 shows the characteristics of machine B in the $i_d\,i_q$-plane during normal operation. The $i_d\,i_q$-axes represent the peak values of the currents while the colored current circles represents the RMS-values of the phase currents, why a phase current of 250 A_{RMS} gives a peak current of $250 \cdot \sqrt{2}$=354 A in the $i_d\,i_q$-plane. The dashed, black lines correspond to the voltage limiting circles calculated for speeds of 1800, 3000 and 6000 rpm respectively. It can be noticed that the voltage limit circles are centered around the point (-113.5,0), which corresponds to a phase current of $113.5/\sqrt{2} \approx 80$ A_{RMS} that is far below the $\Delta T_{max80^{\circ}C}$ phase current of 178 A_{RMS}, previously presented in Chapter 5. This means that the short circuit current is limited to an adequate level. The solid black lines represent constant torque at four different levels, where 364 Nm corresponds to the maximum torque for a phase current of 250 A_{RMS}. For a PMSM with surface mounted permanent magnets, straight lines are expected as $T_e = \Psi_m i_q$ ideally. In Figure 8.1, it is noticeable that a small negative direct axis current can give a shorter current vector, at least for high currents. Further, there are clear indications of cross-saturation between the direct and quadrature axes, as the q-axis current must be increased to maintain the same torque when operating deep into the field weakening region.

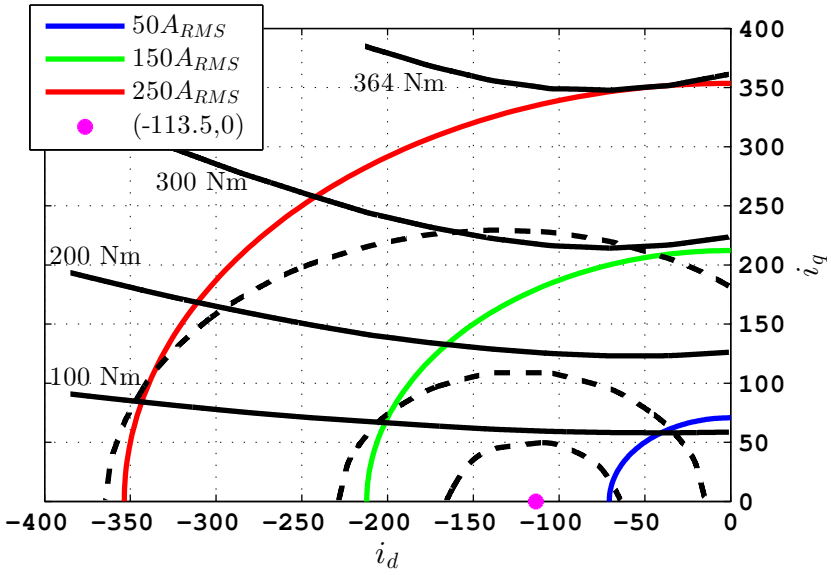

Figure 8.1: Constant torque (solid black lines) and voltage limiting circles calculated for speeds of 1800, 3000 and 6000 rpm. At high speeds, the short circuit current is limited to the point (-113.5,0).

The torque ripple, expressed as the peak to peak torque ripple over the average torque in percent, is shown in Figure 8.2. It is evident that the torque ripple of machine B is low, below 10% over the major part of the $i_d i_q$-plane. Considering the shortest current vector to reach each of the constant torque lines (MTPA), a torque ripple below 5% can be achieved for torque levels above 100 Nm. There is also a considerable area with torque ripple below 2.5% for higher currents.

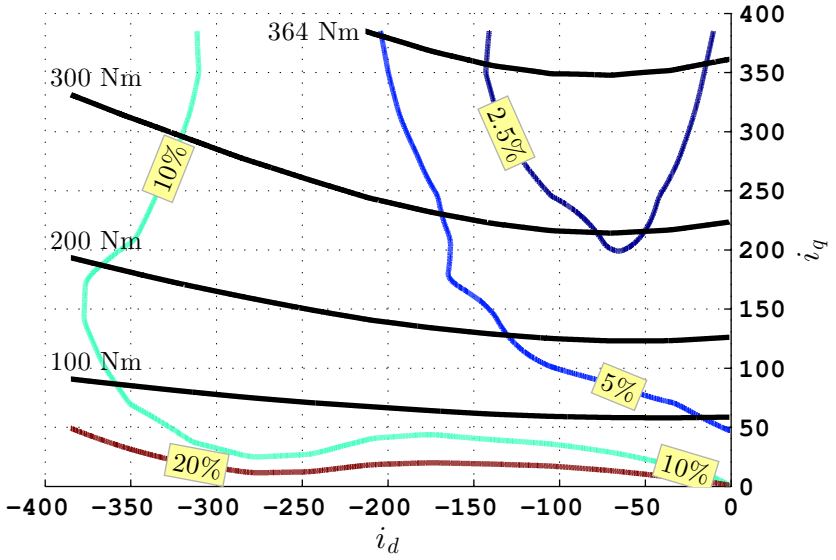

Figure 8.2: Torque ripple and constant torque lines in the $i_d\,i_q$-plane.

8.2.2 Single phase open circuit operation

In Figure 8.3, the open circuit characteristics of machine B is represented in the $i_d\,i_q$-plane. The currents in the remaining two healthy phases are rearranged according to Figure 2.5 in section 2.4 and also Figure 6.2 in section 6.1.1. Hence, phase currents of 250 A_{RMS} gives peak currents of $250\sqrt{2}/\sqrt{3} = 204$ A in the $i_d\,i_q$-plane. The four solid, black lines show constant torque levels of 100, 200, 210 and 227 Nm. To reach 200 Nm, a greater q-axis current must be applied compared to the normal operation in Figure 8.1. On the other hand, the maximum torque is expected to be reduced to $364/\sqrt{3}$=210 Nm for a phase current of 250 A_{RMS}, but 227 Nm is achieved in Figure 8.3. In the unbalanced operation, where the currents are rearranged, the phase voltages are no longer the same in the two remaining phases. An example of phase voltages for one operating point was presented in Figure 6.7 in section 6.1.1 previously. Instead, the fundamental of the phase voltage in the two remaining phases are calculated according to

$$V_{ph} = \omega\Psi_{ph} \tag{8.6}$$

where Ψ_{ph} represents the fundamental of the flux linkage in each phase. The

six dashed lines represent the voltage limiting circles corresponding to speeds of 1800, 3000 and 4000 rpm respectively, where lines of the same color belong to the same phase. If the rotational direction of the machine is changed, the voltage limiting properties is just exchanged between the two phases. There is a clear difference between the two phases in Figure 8.3; the operating point (-100,100) is limited at already 1800 rpm for one phase while it is not limited until 3000 rpm for the other phase.

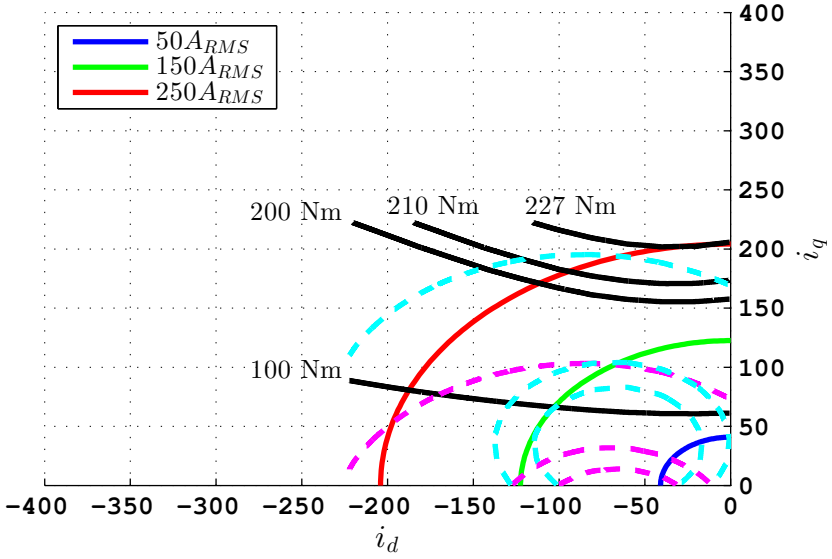

Figure 8.3: Constant torque (black solid lines) together with the different voltage limiting circles for the two remaining phases at speeds of 1800, 3000 and 4000 rpm, when the machine is operated during single phase open circuit fault.

The torque ripple during open circuit operation is shown in Figure 8.4, in the same manner as in Figure 8.2 previously. By a visual comparison between the two figures, it can be seen that the torque ripple has been increased substantially. The average torque is slightly lower than expected but the torque quality is reduced due to the reasons already discussed and shown in section 6.1.1. When the two remaining currents are rearranged to achieve constants currents in the $i_d i_q$-plane, an average torque of 200 Nm will result in a torque ripple up to 40%, corresponding to 80 Nm peak to peak. The MTPA point at the 175 Nm torque line in Figure 8.4 is located at a torque ripple of approximately 30%, which means that the torque ripple was reduced by 50% for the same torque level when introducing current harmonics in section 6.2.

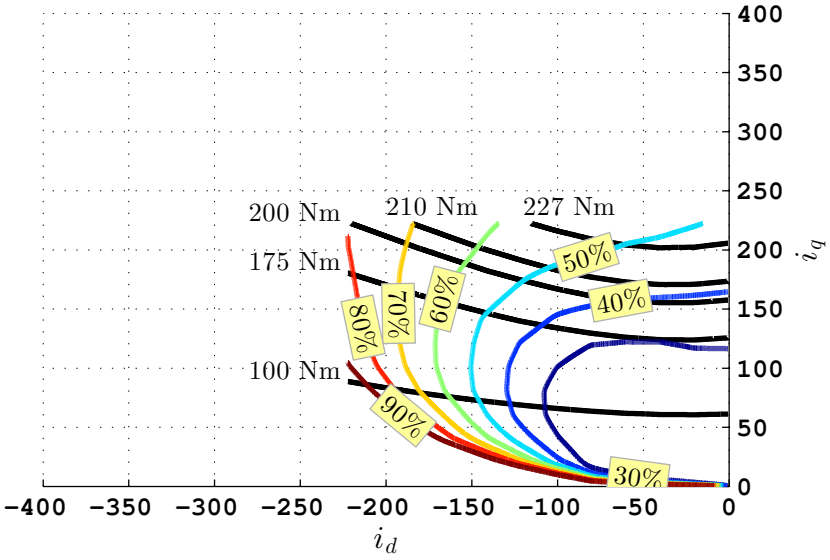

Figure 8.4: Torque ripple and constant torque lines in the $i_d i_q$-plane, when the machine is operated during single phase open circuit fault.

8.3 2004 Prius

8.3.1 Normal operation

The characteristic of the 2004 Prius machine in the $i_d\,i_q$-plane is presented in Figure 8.5. The curved shape of the constant torque lines indicates that the reluctance torque component of the IPM machine is considerable. It can also be seen that the maximum output torque at a phase current of 250 A_{RMS} from the FEA is 374 Nm, as reported in section 4.1.1. The voltage limiting ellipses are centered at (-112.2,0), which gives that the short circuit current is limited to about $112.2/\sqrt{2} \approx 79$ A_{RMS} that is lower than the calculated $\Delta T_{max80^\circ C}$ phase current of 140 A_{RMS} in Chapter 5.

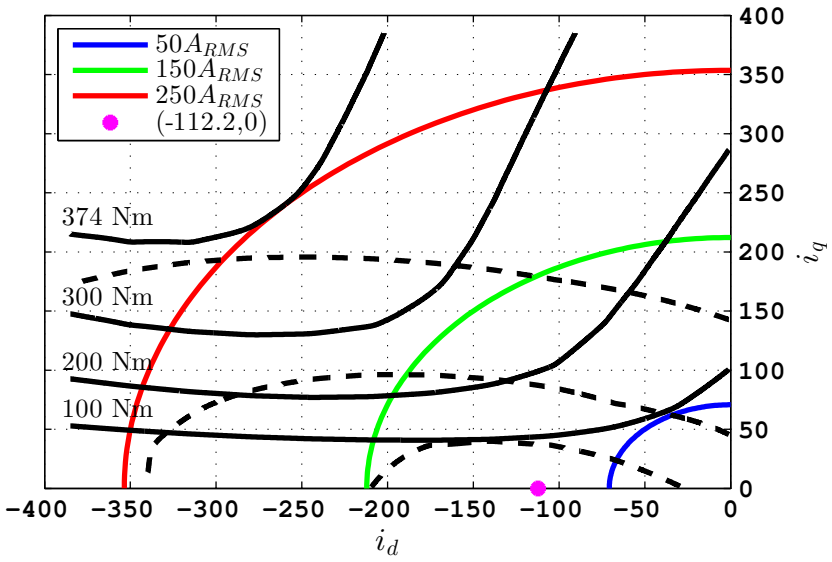

Figure 8.5: Constant torque (solid black lines) and voltage limiting circles calculated for speeds of 2300, 3000 and 6000 rpm. At high speeds, the short circuit current is limited to the point (-112.2,0).

The torque ripple of the 2004 Prius machine in the $i_d\,i_q$-plane is illustrated in Figure 8.6. For the shortest current vector to reach each of the constant torque lines (MTPA), it can be observed that a torque ripple between 20% and 30% is obtained. There are also two areas where a torque ripple below 20% can be achieved, one with high q-axis current with a small negative d-axis current and one with higher currents with a considerable negative d-axis current component.

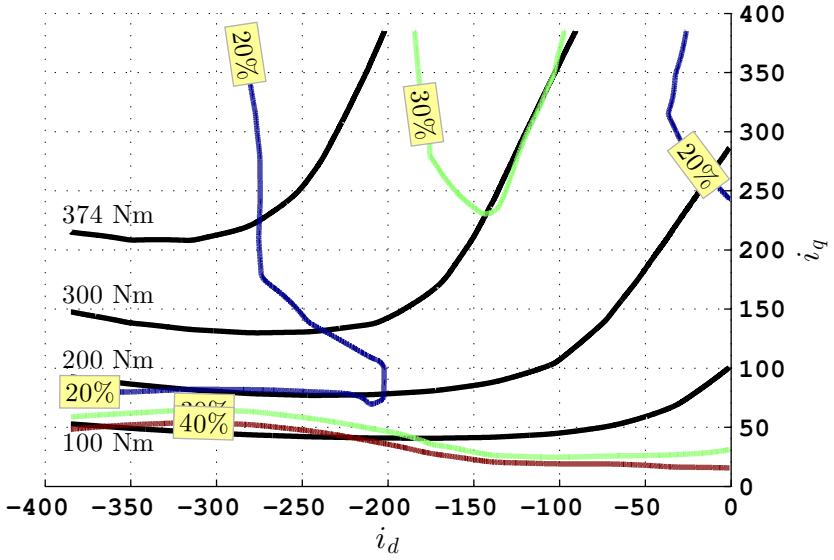

Figure 8.6: Torque ripple and constant torque lines in the $i_d\,i_q$-plane.

8.3.2 Single phase open circuit operation

The phase open circuit characteristics of the 2004 Prius machine is presented in Figure 8.7. The dashed lines, representing the voltage limits of the two remaining phases, show a pattern similar to the curves for machine B in Figure 8.3. The unbalanced operation of the two phases are clearly visible. However, it is still possible to achieve an average torque of more than 200 Nm for a phase current below 250 A_{RMS} when the machine is operated during a phase open circuit fault.

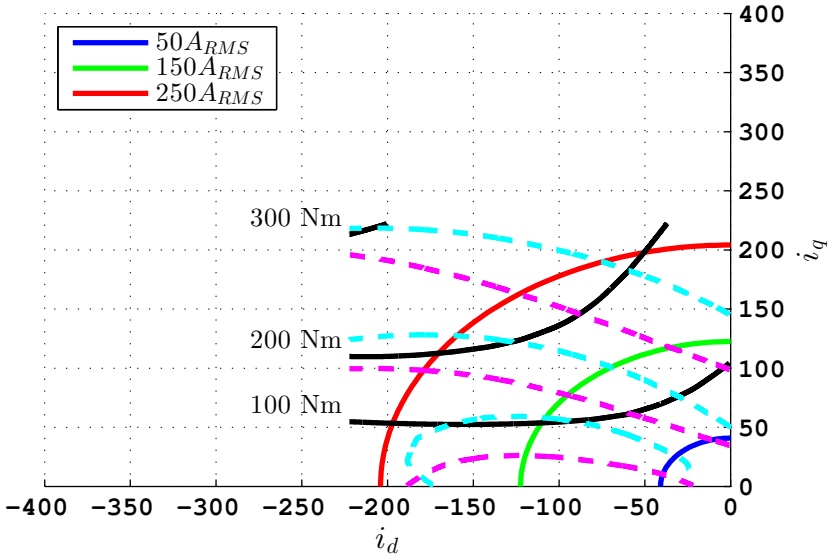

Figure 8.7: Constant torque (black solid lines) together with the different voltage limiting circles for the two remaining phases at speeds of 2300, 3000 and 6000 rpm, when the machine is operated during single phase open circuit fault.

In Figure 8.8, the torque ripple when operating during an open circuit fault is shown. It is clear that the torque ripple has been increased tremendously; there is only a small area where a torque ripple below 50% can be seen.

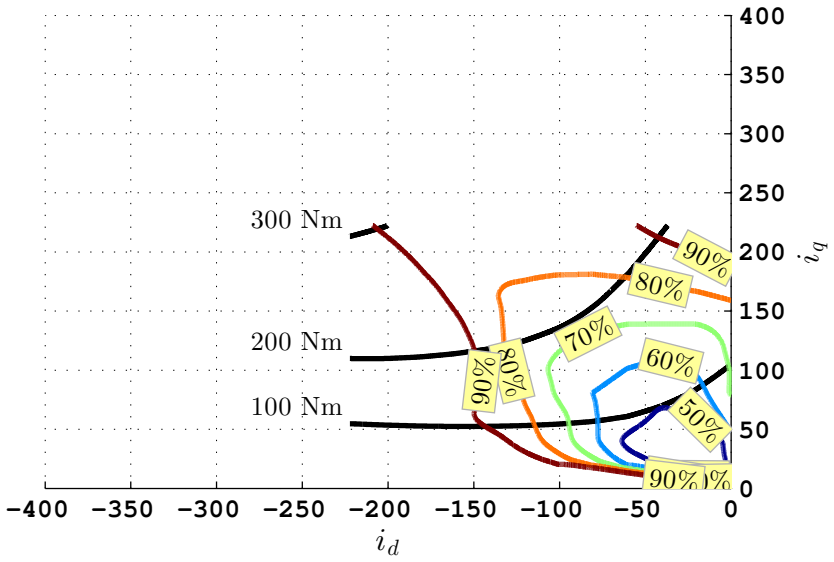

Figure 8.8: Torque ripple and constant torque lines in the $i_d i_q$-plane, when the machine is operated during single phase open circuit fault.

An average torque of 200 Nm will result in a torque ripple of more than 70% corresponding to more than 140 Nm peak to peak. This can be compared with the open circuit operation of machine B at 200 Nm, where the torque ripple is calculated to 30-40% according to Figure 8.4.

8.4 The experimental IPM machine

8.4.1 Normal operation

Constant torque, current limiting circles and voltage limiting ellipses for the experimental machine during normal operation are shown in Figure 8.9. A phase current of 10 A_{RMS} gives a peak current of $10 \cdot \sqrt{2}$=14.1 A in the $i_d i_q$-plane. The shortest current vector to reach a solid black constant torque line contains a negative d-axis current as expected. The voltage limiting ellipses are calculated for 750, 1000, 2000 and 3000 rpm and are represented by the dashed black lines. The center of the ellipses are located at (-23.4,0) which corresponds to a short circuit current of approximately 16.5 A_{RMS}, which marked out in Figure 7.10 in section 7.3.1 and results in a maximum winding temperature of above 300°C.

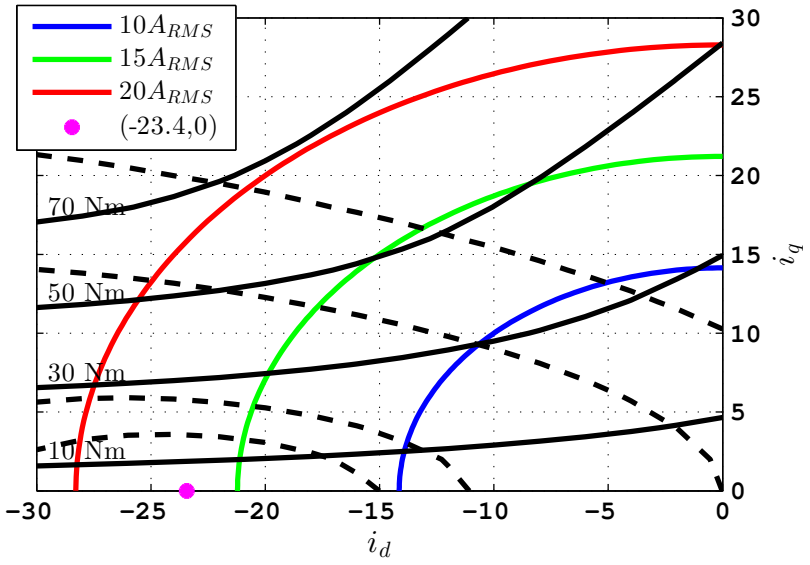

Figure 8.9: Constant torque (solid black lines) and voltage limiting circles calculated for speeds of 750, 1000, 2000 and 3000 rpm. At high speeds, the short circuit current is limited to the point (-23.4,0).

The relative torque ripple for the experimental machine during normal operation is presented in Figure 8.10. Torque quality is not considered a priority in this design and the torque ripple is high, compared to both machine B and the 2004 Prius machine.

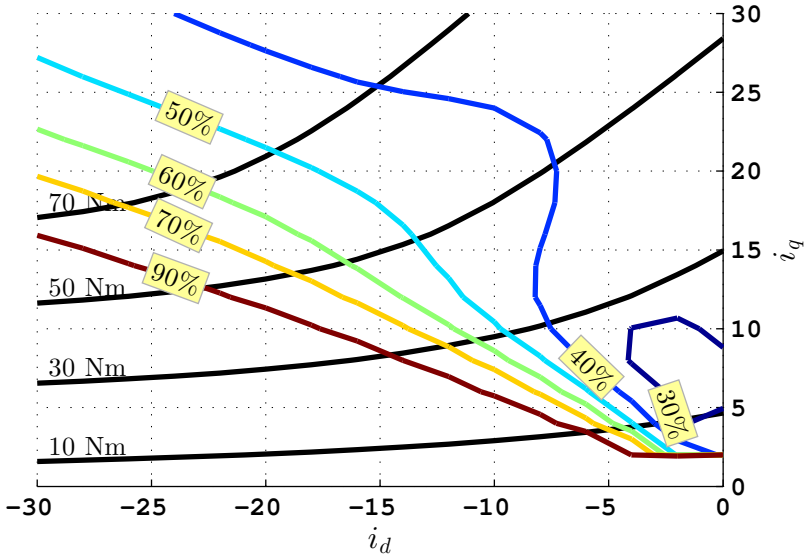

Figure 8.10: Torque ripple and constant torque lines in the $i_d\,i_q$-plane.

8.4.2 Single phase open circuit operation

The steady-state characteristics in the $i_d\,i_q$-plane of the experimental machine during phase open circuit operation is shown in Figure 8.11. A phase current of 10 A_{RMS} gives a peak current of $10 \cdot \sqrt{2}/\sqrt{3}$= 8.2 A i the $i_d\,i_q$-plane. The constant torque lines are more or less identical to the ones during normal operation, shown in Figure 8.9 previously. Also the voltage limiting ellipses are located close to their original position in Figure 8.9, with each phase on each side of their corresponding curve during normal operation. The overall picture in Figure 8.11 is that the open circuit characteristics of the experimental machine agrees well with the theory presented in section 2.4. It has approximately the same properties as during normal conditions except that the currents in the rotating dq reference frame are reduced by a factor $1/\sqrt{(3)} \approx 0.58$ for the same phase current magnitudes.

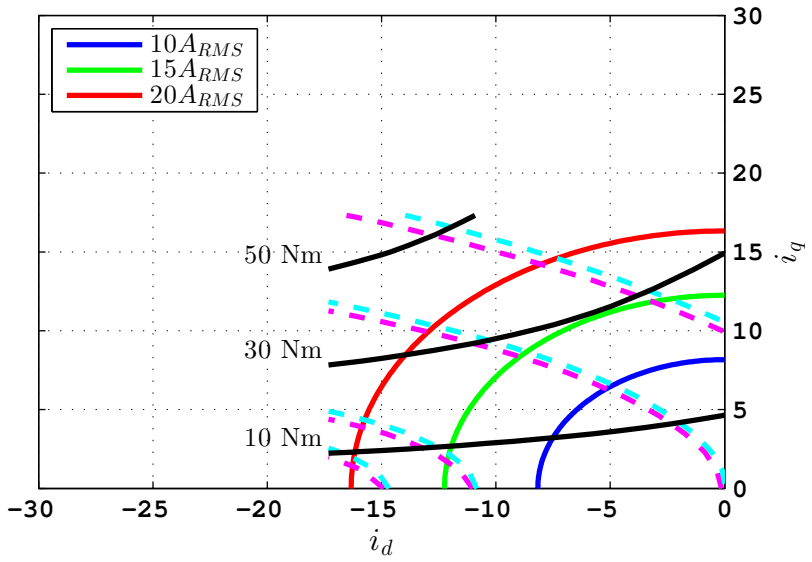

Figure 8.11: Constant torque (black solid lines) togetherwith the different voltage limiting circles for the two remaining phases at speeds of 750, 1000, 2000 and 3000 rpm, when the machine is operated during single phase open circuit fault.

The relative torque ripple during open circuit operation is presented in Figure 8.12. There is a modest difference compared to Figure 8.10, where the machine is operated during normal conditions. It is actually possible to identify some areas where the torque quality has been slightly increased during open circuit operation compared to during normal operation.

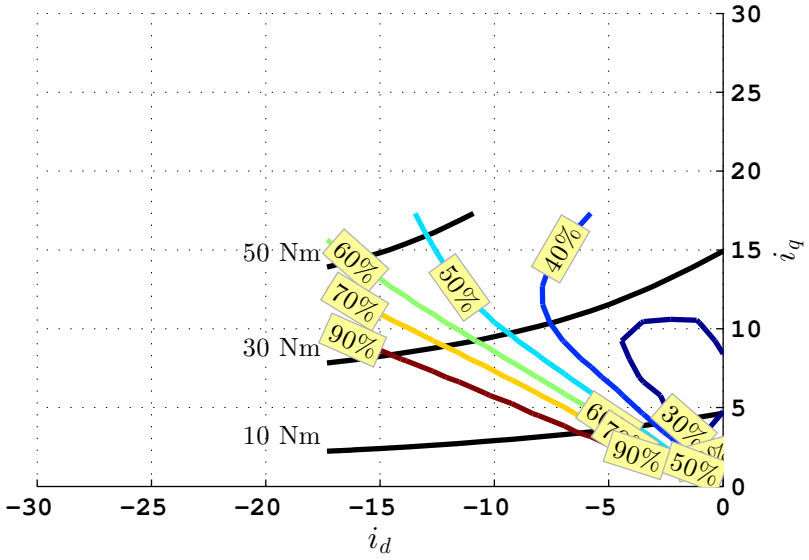

Figure 8.12: Torque ripple and constant torque lines in the $i_d\,i_q$-plane.

8.5 Concluding remarks of the analysis in the $i_d i_q$ -plane

In this chapter, the fault-tolerant fractional slot machine has been analyzed together with the two reference machines in the $i_d\,i_q$-plane during normal conditions and during phase open circuit fault. Some characteristics are very similar while others are different.

Both the "high torque density" machines, machine B and the 2004 Prius, which are designed very compact for vehicle applications are shown to handle the three phase short circuit current continuously while the experimental IPM is not. But on the same time, the different phase voltage limitations during phase open circuit operation of these machines are clear. In a simplified matter, this can be linked back to (1.1), where the product between the PM flux and induced flux has been maximized to achieve the highest torque. Together with the requirement of a reasonable field weakening capability it is likely that the inductance value is quite high in a design for a vehicle application. The high PM flux gives a machine that is relatively high up on its BH-curve already before the currents are applied during an open circuit fault. When the currents are applied (rearranged ±30°), the high inductance value gives a considerable flux difference between the two phases, see Figure 6.7 in section 6.1.1.

The difference in phase voltage limitations can also be connected back to the presented converter topologies in Figure 2.2 in section 2.4. A machine operated by the six leg converter will clearly be speed limited by the phase demanding for the highest phase voltage. In case of the four leg converter, it might be possible to improve the situation by sharing the available DC-link voltage between the two remaining phases by introducing oscillations in the "neutral point" (as for third harmonic injection to a machine operated during normal conditions). This and also the benefits of adding an inductance between the neutral point and the fourth leg have been pointed out in [17].

Further, it has also been observed that the "low torque density" machine, the experimental IPM, shows a characteristic that is much closer to the theory that is found in the literature. Both its average torque, torque ripple and phase voltages agrees very well.

Finally, it can be concluded that it is of particular importance to use models that include non-linearity when studying high torque density machines, which are likely to be found in vehicle applications. Without considering the different saturation levels of the phases in these applications, the torque quality may be reduced tremendously from what is expected when the machines are operated during a single phase open circuit fault.

Chapter 9

Transient thermal analysis

In this chapter, the fault-tolerant fractional slot machine and the experimental IPM reference machine are evaluated thermally using a transient lumped parameter circuit. The chapter starts with an introduction of the lumped parameter thermal circuit and a brief description of how the model is implemented. Thereafter follows the evaluation of the fault-tolerant fractional slot machine, operated both during normal and faulty conditions. Finally, the transient model is validated using the experimental IPM machine and data recorded in the lab. In order to treat uncertainties in the machine modeling, some of the uncertain parameters are calibrated towards measurements in this chapter.

9.1 Lumped parameter thermal circuit

The relatively simple lumped parameter thermal circuit used, includes six unique nodes per slot or tooth and is shown in Figure 9.1. The water and the rotor nodes are both connected to each of the slot symmetries and the thermal resistance of the air-gap is calculated according to section 1.8.2. The water node is chosen to be reflecting the average temperature of the inlet and outlet cooling water. Despite this approach, not taking the thermal resistance and capacitance of the aluminum jacket surrounding the stator yoke into account, a thermal resistance is added between the water and the stator nodes to represent the contact resistance between the domains when modeling the experimental IPM machine.

The thermal resistances for internal heat transfer inside the stator domain can be derived straightforward from (1.30), while the thermal capacitances of the stator are calculated based on the dotted regions marked out in Figure 9.1 and (1.31). The thermal capacitance of a winding node is calculated based on the amount of copper in a phase and a thermal resistance between the winding nodes and the stator nodes includes: a part of a stator segment, a slot-liner and an additional resistance that is found by using a calibration procedure.

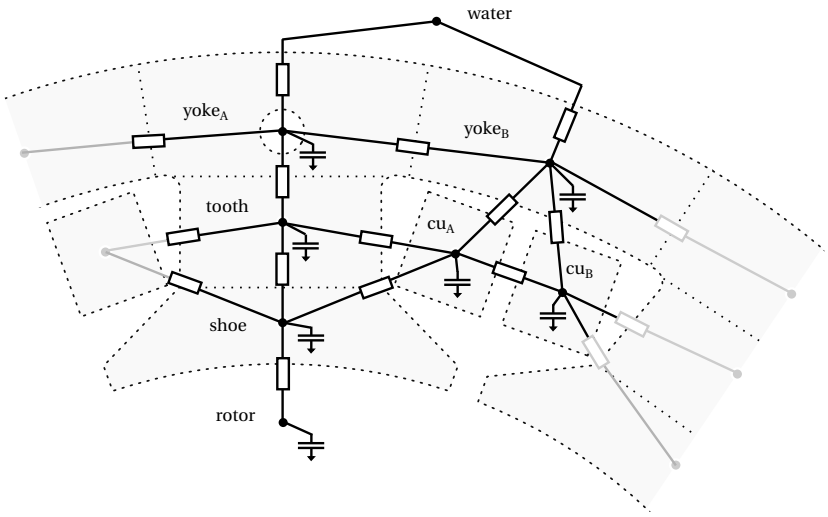

Figure 9.1: Lumped parameter thermal circuit.

The lumped parameter thermal circuit in Figure 9.1 is implemented in state space form, where the state derivative, $\dot{x_n}$, of the n^{th} node is expressed as

$$\dot{x_n} = \frac{1}{C_n} \sum_i \frac{x_i - x_n}{R_{in}} + \frac{u_n}{C_n} \tag{9.1}$$

where x_n represents the current state of the node, C_n the thermal capacitance of the node, u_n the loss injection into the node and x_i the adjacent nodes connected to the n^{th} node via the thermal resistance R_{in}. If the n^{th} node is a winding node, where the winding losses are strongly dependent on the temperature of the winding, (9.1) is replaced by

$$\dot{x_n} = \frac{1}{C_n} \sum_i \frac{x_i - x_n}{R_{in}} + \frac{u_n^2 R_s(x_n)}{6C_n} \tag{9.2}$$

where the node input, u_n, represents the winding current instead of the losses. The phase resistance, $R_s(x_n)$, is a function of the state/temperature, x_n, and is updated according to (1.38) for each step during the calculation. For the experimental machine, with three coils per phase and each coil is represented by two nodes, one sixth of the phase resistance belongs to each winding node.

9.1.1 Thermal resistance over the air-gap

According to section 1.8.2, the thermal resistance of the air-gap is determined by the rotational speed of the rotor but also by properties of the air in the air-gap. Therefore, the equivalent air-gap resistances for the fault-tolerant fractional slot machine and the experimental IPM machine are calculated for two temperatures. The air density, ρ_{air}, the thermal conductivity of the air, λ_{air}, and the dynamic viscosity of the air, μ_{air}, are modeled using the values in Table 9.1 to represent temperatures of 20°C and 120°C.

Table 9.1: Values of air properties that are used to represent air temperatures of 20°C and 120°C

Air property	**20°C**	**120°C**
ρ_{air}, kg/m^3	1.21	0.90
λ_{air}, W/(m·K)	0.026	0.033
μ_{air}, kg/(s·m)	$1.81 \cdot 10^{-5}$	$2.26 \cdot 10^{-5}$

The resulting thermal resistances as function of the rotational speed and the two temperatures are shown in Figure 9.2. The main difference, related to temperature, is in the low speed region; but the transitions between different flow types in the air-gap are also affected. The transitions are indicated by the dashed lines and it can be noticed that a fully turbulent flow is not present in the experimental IPM machine, see Figure 9.2b. This is because its Taylor number is much lower, both due to the lower air-gap radius, r_g, and due to the smaller air-gap, l_g, see (1.36). The geometrical factor, F_g in (1.37), are calculated to more or less the same values for both designs. At low speeds the thermal resistance across the air-gap, $R_{th,g}$, is determined by the ratio between cylindrical area of the air-gap, A_g, and the air-gap length, l_g, see (1.32) and (1.33). Hence, the experimental IPM machine gets a higher thermal resistance than the fault-tolerant fractional slot machine.

However, the thermal resistance across the air-gap is updated by an input of the rotational speed into the transient model only. The properties corresponding to the higher air temperature of 120°C in Table 9.1 is used, since the thermal limit of operating points is to be found.

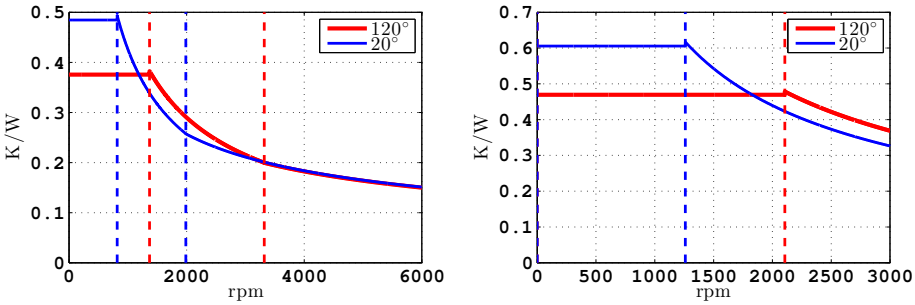

(a) The fault-tolerant fractional slot machine.

(b) The experimental IPM machine.

Figure 9.2: Thermal resistance of the air-gap as function of speed and air temperature. The dashed lines represent the transition between different flow types.

9.2 The fault-tolerant fractional slot machine

The thermal resistances are calculated using (1.30) and the thermal capacitances using (1.31). The current corresponding to the ΔT_{max}=80°C in Chapter 5, without any other losses, is used in order to tune the model to give a winding temperature of 120°C for water node temperature of 40°C. The model is tuned by a slight increase of the thermal resistance of the slot insulation film, in that way is the relative temperature increase of 80°C preserved. The final thermal resistances are presented in Table 9.2. The permanent magnet and the iron losses in section 6.4 are used as input to the thermal model. All the rotor losses are added to the rotor node while the stator losses are distributed to the different stator nodes according to the domains that are shown in Figure 9.1.

Table 9.2: Thermal resistances that were used in the transient thermal model of the fault-tolerant fractional slot machine.

Connected nodes	**Thermal resistance, K/W**
yoke_A-yoke_B	0.91
yoke-water	0.06
yoke_A-tooth	0.34
tooth-shoe	0.44
cu-shoe	7.12
cu-tooth	1.75
cu-yoke_B	4.03
cu-cu	12.0

9.2.1 Thermal limit of operating points

The calculated winding temperatures for continuous operation with a water node temperature of 40°C are shown for normal and phase open circuit operation in Figure 9.3. By a visual comparison of Figure 9.3a and Figure 9.3b, the winding temperature is higher for a given operating point when operating during single phase open circuit fault compared with normal operation, which is expected due to the difference in copper losses. One interesting aspect is the thermal limits in relation to the electrical limits, which are very similar during normal and phase open circuit operation. If considering a maximum winding temperature of 180°C, the maximum low speed torque during normal operation is reduced by 5.9% and it is reduced by 6.5% during phase open circuit operation in relation to their respective electrical limits.

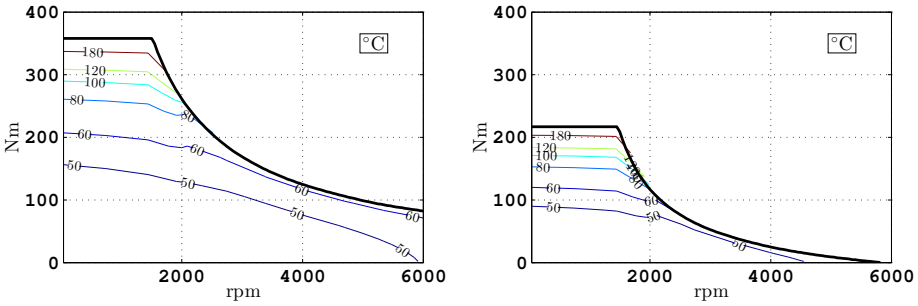

(a) Normal operation.

(b) Single phase open circuit operation.

Figure 9.3: Calculated winding temperatures for continuous operation and a constant water node temperature of 40°C.

The calculated rotor temperatures for continuous operation with a water node temperature of 40°C are shown for normal and phase open circuit operation in Figure 9.4. In both operation modes, the highest rotor temperatures are achieved at a speed just below field weakening operation. In these operating points, the phase current amplitudes are the same in both operating modes. Without a deeper analysis of the exact angles between the induced flux from the teeth and permanent magnets, there is at least an indication that phase open circuit operation is not worse than normal operation.

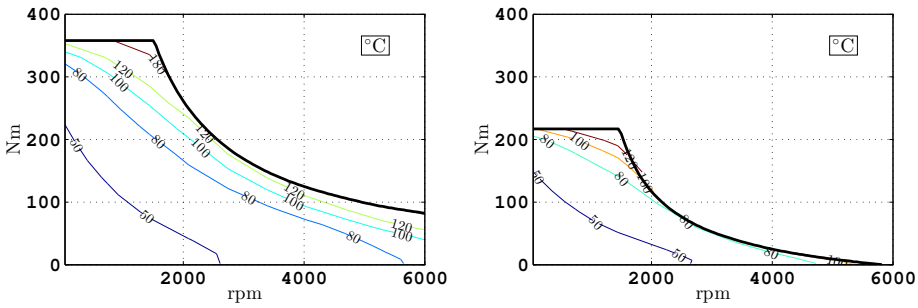

(a) Normal operation.

(b) Single phase open circuit operation.

Figure 9.4: Calculated rotor temperatures for continuous operation and a constant water node temperature of 40°C.

9.2.2 Overload capabilities

In Figure 9.3, it was observed that the 180°C thermal limits of the winding are around 6% (considering the torque) below the electrical limit in the low speed region, both for normal and open circuit operation. To investigate the overload capability, steady-state temperatures of each node when operating at 60% and 80% of the electrical limit at 1000 rpm, are first calculated for each operating mode. Starting from those thermal steady-state temperatures, it is calculated how long time the machine can be operated at 100% of the electrical limit in each operating mode. Since the steady-state temperatures are closely linked to the cooling water temperature, the possible overloading times are calculated for different water node temperatures as well.

In Figure 9.5, the calculated overloading times are presented. It can be noticed that it is generally possible to operate at 100% of the electrical limit somewhat longer in case of phase open circuit fault. This is reasonable, since the total losses during normal operation are approximately twice as high as during phase open circuit operation, see Figure 6.20b. The relatively small time differences, despite the big loss differences, indicate that a winding temperature is more related to its own winding current than the total loss levels.

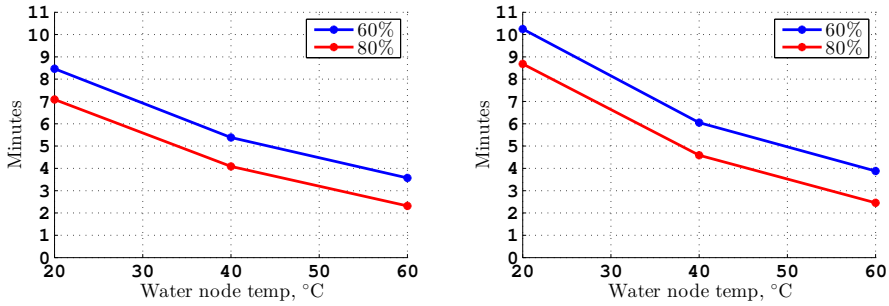

(a) Normal operation.

(b) Single phase open circuit operation.

Figure 9.5: Calculated time at the electrical limit at 1000 rpm, when starting from thermal steady-states corresponding to 60% and 80% of the electrical limit for different water node temperetures.

9.3 The experimental IPM machine

The thermal resistances are calculated using (1.30) and the thermal capacitances using (1.31), in the same way as for the fault-tolerant fractional slot machine. A final tuning of the transient model is carried out using several measurements. Starting with a machine close to a thermal steady-state at room temperature, warm and cold water were fed alternately through the cooling system while recording the thermal response. The instantaneous average temperature of the inlet and the outlet water is used as input to the transient thermal model. An example is shown in Figure 9.6.

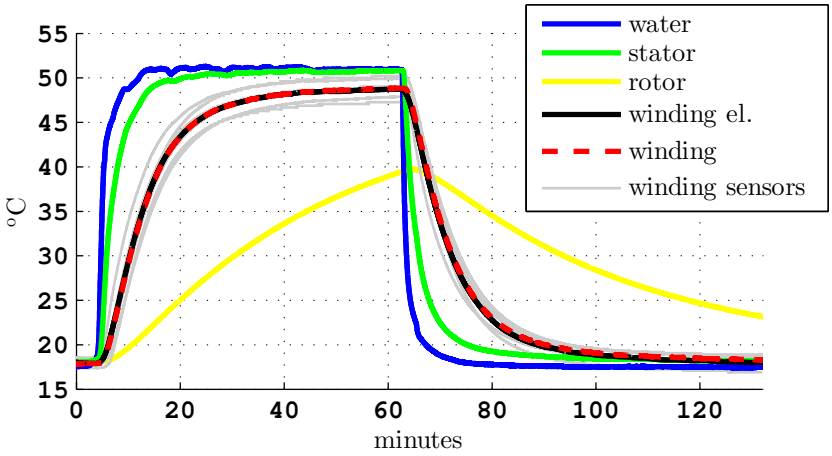

Figure 9.6: Measured average temperatures used for calibration of the lumped parameter thermal circuit. Average winding temperatures are measured both electrically (resistance) and with the sensors. The individual sensors are represented by the thin grey lines.

An additional resistance connected in series with the existing resistances between the stator yoke nodes and the water node, representing contact resistance, is calibrated relatively easy. When calibrating the resistances between the stator nodes and a winding node, it is found that the three resistances must be calibrated separately for a reasonable match. The final thermal resistances are presented in Table 9.3.

Table 9.3: Thermal resistances that were used in the transient thermal model of the experimental IPM machine.

Connected nodes	**Thermal resistance, K/W**
yoke_A-yoke_B	0.92
yoke-water	0.26
yoke_A-tooth	0.17
tooth-shoe	0.19
cu-shoe	9.79
cu-tooth	10.15
cu-yoke_B	8.75
cu-cu	42

9.3.1 Thermal limit of operating points

The thermal limit of the operating points for the experimental IPM machine is evaluated in the same manner as the fault-tolerant fractional slot machine in

section 9.2.1. The calculated winding temperatures for continuous operation with a water node temperature of 40°C are shown for normal and phase open circuit operation in Figure 9.7. The highest torque curves correspond to phase currents of 20 A_{RMS}, which is shown to be too high in section 7.3 already. However, if considering an electrical limit of 20 A_{RMS} and a thermal limit of 180°C, the torque is reduced by 23.6% during normal operation and by 25.4% during single phase open circuit operation. The relative numbers are similar, which was also shown for the fault-tolerant fractional slot machine in section 9.2.1.

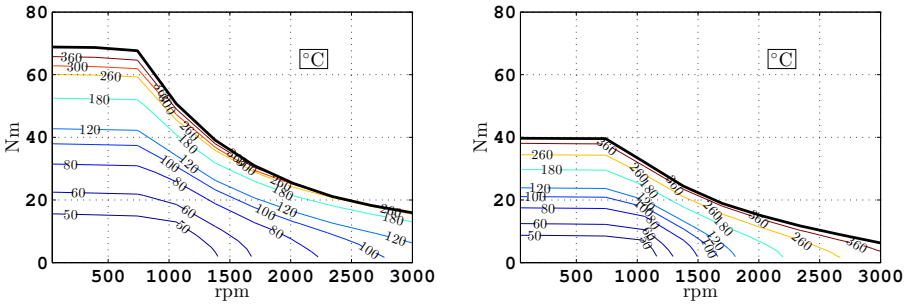

(a) Normal operation.

(b) Single phase open circuit operation.

Figure 9.7: Calculated winding temperatures for continuous operation and a constant water node temperature of 40°C.

The calculated permanent magnet temperatures for continuous operation with a water node temperature of 40°C are shown for normal and phase open circuit operation in Figure 9.8. The highest temperatures are found at the highest speeds and it is clear that normal operation will be limited by the rotor and the permanent magnet temperature rather than the winding temperature in this region. Even when considering the same operating points in this region, normal operation shows higher temperatures than open circuit operation.

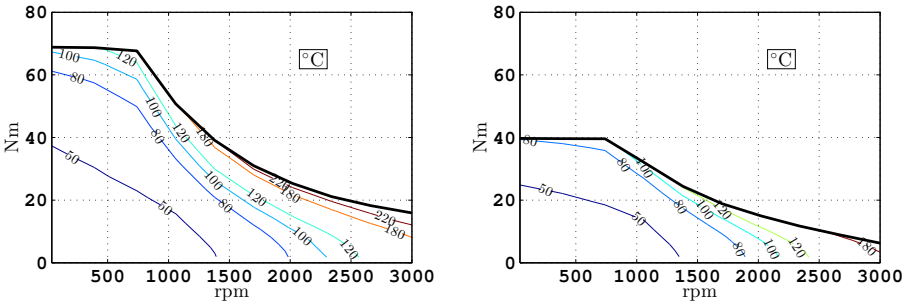

(a) Normal operation.

(b) Single phase open circuit operation.

Figure 9.8: Calculated rotor temperatures for continuous operation and a constant water node temperature of 40°C.

9.3.2 Three phase operation

The modeled machine temperatures in this section correspond to the same drive cycle that is measured and presented in section 10.3.1. When comparing several modeling results using the transient model and the measurements it is observed that the calculated rotor temperatures typically are colder than the measured rotor temperatures. In section 10.1.5, a number of thermal connections to the surroundings are identified and their equivalent thermal resistances are estimated. One of these is the thermal connection between the rotor and the surroundings via the shaft, which is estimated to 2.1 K/W. During the measurements, there is an extra temperature sensor which is mounted in the aluminum structure (close to the shaft) that houses the thermal measurement system on the rotor side. This node, connected to the rotor via 2.1 K/W resistance is added to the model presented in Figure 9.1. The measured average temperature in the "shaft node" and the average water temperature from section 10.3.1 are both used as input to the model. The loss inputs are from the FEA presented in section 7.4.2.

The winding temperatures from the transient model are shown in Figure 9.9. All the winding temperatures are the same during balanced conditions. The peak to peak value is similar to the measurements but the average is slightly lower compared to the measurements.

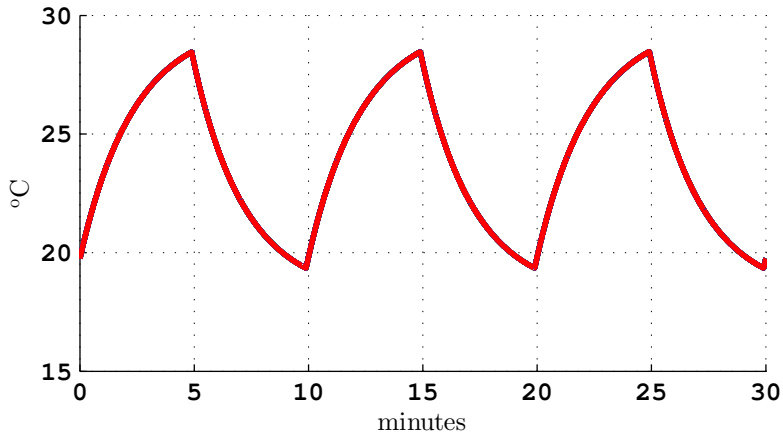

Figure 9.9: Simulated winding temperature during three phase operation.

The stator temperatures from the transient model is shown in Figure 9.10. Compared with the measured stator temperatures, shown in Figure 10.21, the agreement is quite good, although the transient model shows somewhat lower temperatures.

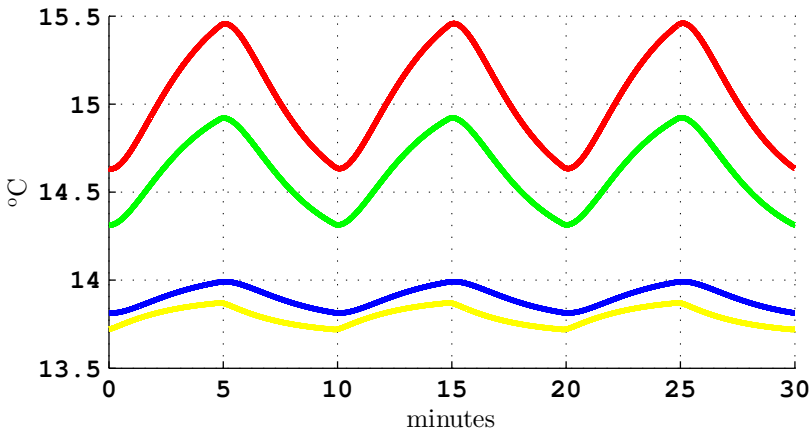

Figure 9.10: Simulated stator temperatures during three phase operation.

The rotor temperature from the transient model is shown in Figure 9.11, when running the model both with and without the shaft node. Making a comparison with Figure 10.22 it can be observed that a better agreement is achieved, when including the shaft node.

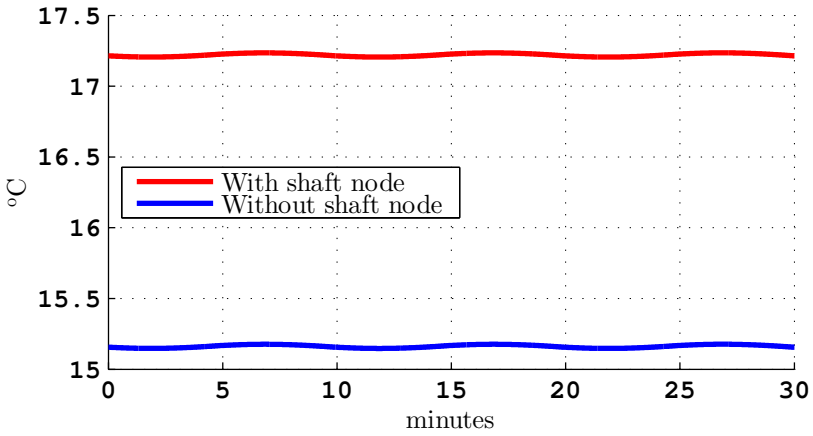

Figure 9.11: Simulated rotor temperature during three phase operation.

9.3.3 Operation during open circuit fault

In this section, the machine temperatures are modeled using the transient model in the same manner as in the previous section. The corresponding measured drive cycle is presented in section 10.3.2 later.

The winding temperatures from the transient model are shown in Figure 9.12. The temperatures in the current carrying windings agree well with the measured temperatures. The temperature in the open circuited winding is slightly lower than in the measurements, which indicates that the thermal resistance between the cu_A and cu_B nodes in Figure 9.1 is estimated too high. Two temperature levels can be seen in the current carrying windings (red and green lines), depending on if the node is sharing a slot with another node that is carrying current or not.

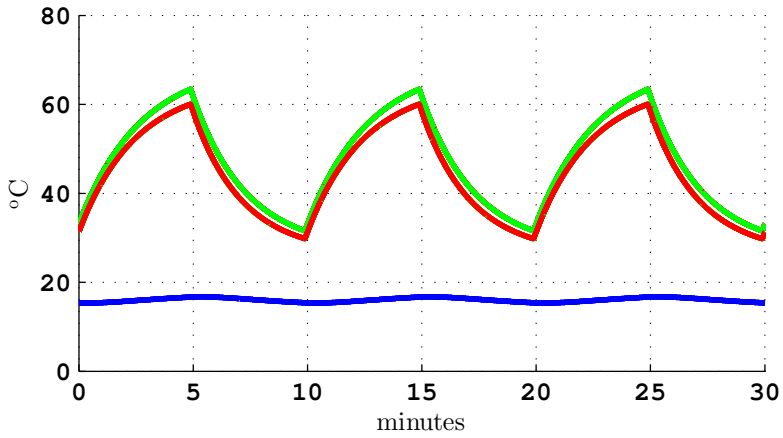

Figure 9.12: Simulated winding temperatures during single phase open circuit operation.

The stator temperatures from the transient model are shown in Figure 9.13, which shows more temperature levels than in Figure 9.10 due to the unbalanced operation during a single phase open circuit fault. The temperatures in Figure 9.13 agrees well with the measurements presented in Figure 10.29.

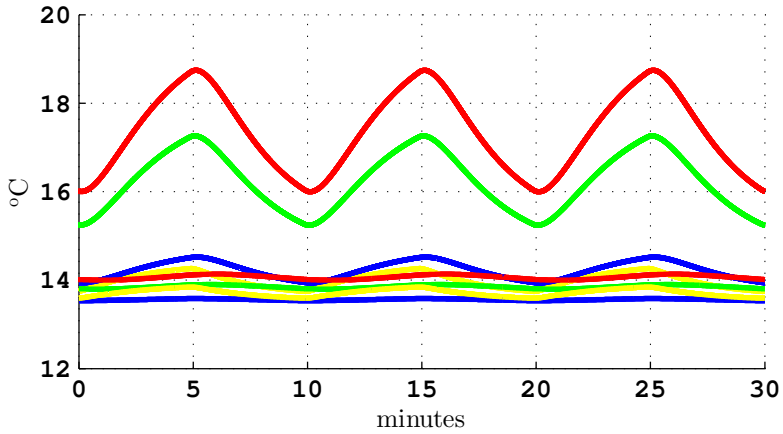

Figure 9.13: Simulated stator temperatures during single phase open circuit operation.

In Figure 9.14, the rotor temperatures are shown both when including and excluding the shaft node. Also during phase open circuit operation, the agree-

ment between the transient model and the measurements is better when the shaft node is added to the model. The corresponding measurements are shown in Figure 10.30.

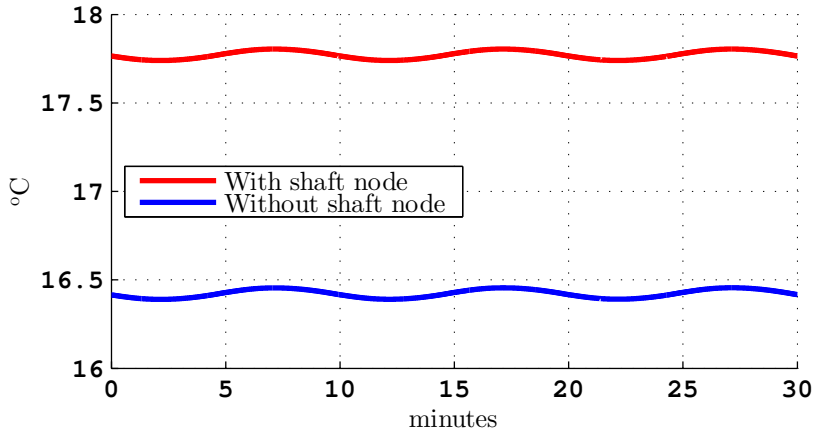

Figure 9.14: Simulated rotor temperature during single phase open circuit operation.

Overall, there is a good agreement between the transient model and the measurements presented for the same drive cycles in Chapter 10. An aspect to take into account when comparing the winding temperatures is that the each coil side is modeled as a single temperature in each slot, while each measured winding temperature represents the temperature in a single point of a winding with a temperature distribution.

Chapter 10

Experimental investigation of the IPM machine

This chapter presents some of the measurements carried out with the experimental IPM machine in the lab. The first part introduces the experimental setup and is followed by the measurement results related to the $i_d i_q$-plane analysis in Chapter 8. The chapter ends with transient measurements during the same drive cycle as was modeled in Chapter 9. Both the measurements presented in the $i_d i_q$-plane and the transient measurements during the drive cycle are performed during balanced three phase operation and during unbalanced operation corresponding to a single phase open circuit fault.

10.1 Experimental setup

This section provides information about the devices that are used in the experimental setup, together with calibration procedures used. A schematic illustration of the electrical part of the experimental setup is shown in Figure 10.1, and a list of the key devices is presented in Table 10.1. The whole system can be run automatically to execute a sequence of operating points or drive cycles, which in turn allows for extensive measurements that easily can be repeated if desired.

The digital signal processor (DSP) sends a signal to the relay box to set if the machine should be connected to the converter, the DC-source (for resistance measurements) or be disconnected (for back-EMF measurements). When the machine is connected to the converter, the DSP is controlling the machine currents via the pulse width modulation (PWM) signals to the converter using the feedback signals in terms of the current measurements and the encoder position. Moreover, it act as the master state-machine which handles the state of a predefined sequence of operating points and measurements. The connection to the PC is used to control the state of the computer's corresponding prede-

fined sequence which is running in slave mode. The PC is triggered to set the operating point of the load machine and to record data from the thermal measurement system and the power analyzer.

The phase voltages and currents together with the torque sensor signal are measured by the power analyzer and the data is passed to the PC. By utilizing the "motor evaluation" feature of the power analyzer, it is possible to synchronize all the measurements using the encoder index (Z) pulse to trig the phase lock loop (PLL) algorithm of the instrument. Thereby, the angles of the phase currents can be accurately determined both during balanced and unbalanced conditions.

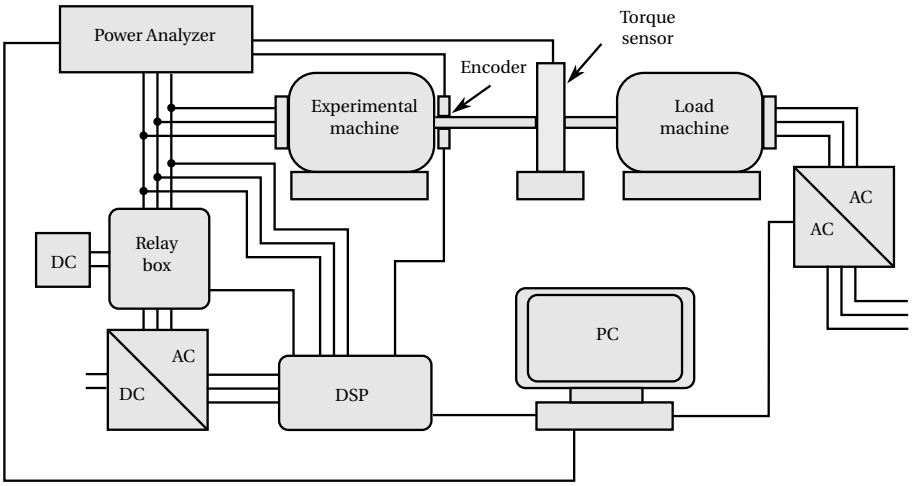

Figure 10.1: Schematic illustration of the electrical part of the experimental setup.

Table 10.1: List of devices in the experimental setup.

Device	**Model**
DSP	dSPACE DS1103
Encoder	HENGSTLER RI76TD
Load machine	Busck WE200L-4
Power analyzer	Yokogawa WT1800
Torque sensor	Lorentz DR-2012
Water flow sensor	SWISSFLOW SF800

10.1.1 Rotor angle calibration

The encoder signals are sent both to the DSP (for current control) and the power analyzer (for measurements), as is illustrated in Figure 10.1. The encoder pulses are sent through a passive optocoupler unit in order to avoid a closed loop current path between the measurement system and the control/drive system. During a number of no-load measurements, it is observed that the measured angles of the fundamental back-EMFs shifted slightly depending on the speed of the machine. This was caused by a noticeable delay from the generation of the encoder index (Z) pulse and the start of the PLL algorithm of the power analyzer. Therefore, all the current angle measurements are made with respect to a no-load back-EMF angle measurement at the same speed. The difference between the angle of the current reference and the measured current angle, corresponding to the first 49 operating points in section 10.2.1, is shown in Figure 10.2.

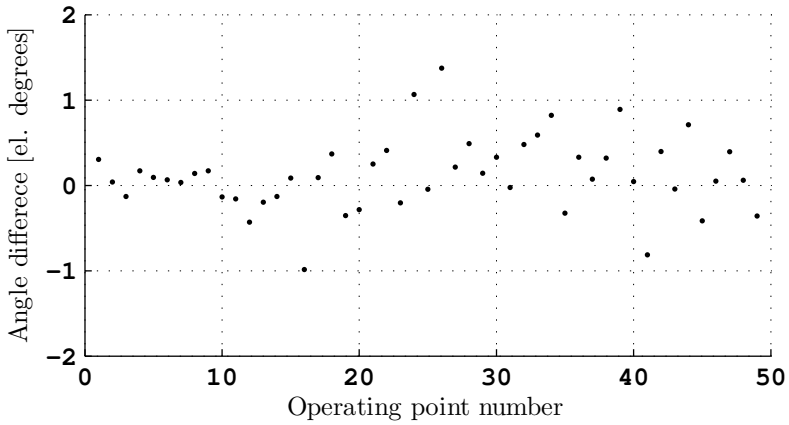

Figure 10.2: Difference between the current reference angle to the controller and the measured current angle for 49 operating points.

10.1.2 Torque sensor calibration

A relatively simple torque sensor calibration procedure is used and carried out before starting and after finishing a measurement occasion in the lab. The main purpose is to identify if a drift in the sensor signal occurs between measurement occasions and/or during measurements, not to provide the highest possible accuracy as efficiency is not the main focus of the measurements. The setup is shown in Figure 10.3, where the shaft is locked on one side of the torque sensor and a weight calibration beam is attached to the shaft on the other side of the torque sensor. The torque calibration measurements is carried out with and without a 5 kg reference weight attached on the beam 22.8 mm from the rota-

tional center of the shaft.

An example of some typical values from a calibration procedure is shown in Table 10.2. No major difference in the sensor characteristics over time (days and weeks) is recorded, but the increase of the signal when adding the calibration weight tends to be higher before the measurements than after the measurements, as can be seen in Table 10.2. An average value of the before calibration and the after calibration values is used to determine the sensor torque constant corresponding to each measurement occasion. It is possible that the discrepancy between the two calibrations could have been reduced by a preloading cycle of the torque sensor before starting the first calibration.

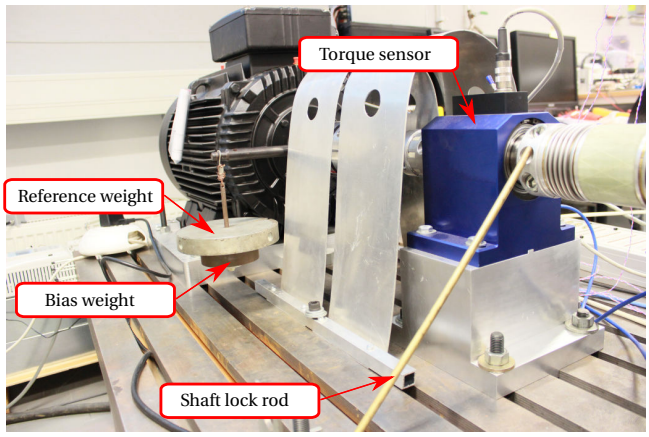

Figure 10.3: Torque sensor calibration setup.

Table 10.2: Example of torque sensor calibration measurements before and after the machine is operated.

Torque	**Value**
Bias, before	4.52
Weight, before	15.59
Bias, after	4.45
Weight, after	15.70
(Bias, before)/(Bias, after)	101.49%
(Weight, before)/(Weight, after)	99.28%
Δ_{before}=(Weight, before)-(Bias, before)	11.07
Δ_{after}=(Weight, after)-(Bias, after)	11.25
$\Delta_{\text{before}}/\Delta_{\text{after}}$	98.38%

10.1.3 Temperature sensor calibration

The temperature sensor calibration is carried out in a tank with accurately temperature controlled circulating oil. The setup is shown in Fig. 10.4. Starting from a few degrees over room temperature, the temperature is increased in steps of approximately 10°C up to 200°C (the digital sensors are removed before entering their maximal temperature of 125°C). At each temperature level, the steady-state temperature is used to create a look-up table for each analog sensor channel.

Regarding the digital sensors, it is noticed that one sensor showed a value approximately 0.25°C off compared to the rest of the digital sensors, when they were left on the office desk overnight. After replacing this discrepant sensor, the digital sensors were all within a band corresponding to two times the resolution of the sensors ($2 \cdot 0.0625$°C) during the calibration, thus no look-up tables for correction of the digital sensors are needed.

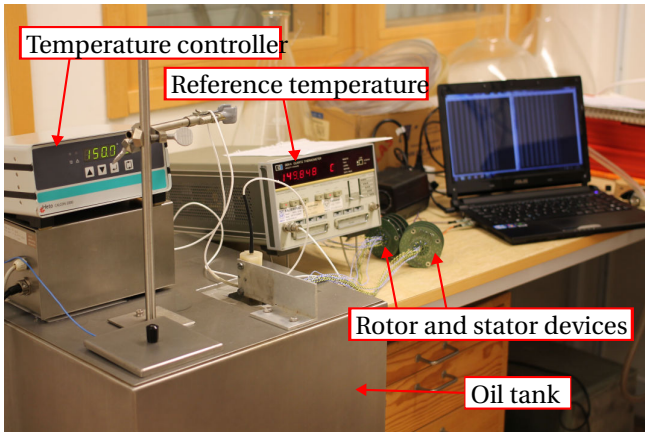

Figure 10.4: Temperature sensor calibration setup.

The pre-calibrated sensors are mounted into the stator and the rotor. The rotor during temperature sensor mounting is shown in Figure. 10.5, where the sensor wire path through the hollow shaft can also be seen. Each sensor is fitted at a specific depth in the axial direction of the rotor stack and the hole is filled with thermal epoxy glue.

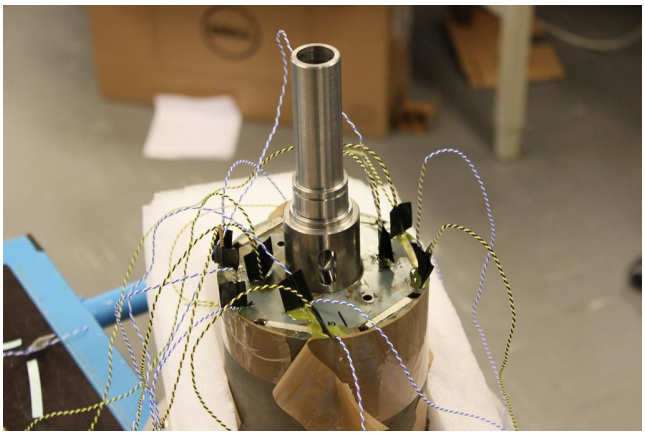

Figure 10.5: Rotor during the temperature sensor mounting.

10.1.4 Water flow sensor calibration

The water flow sensors are calibrated by recording the frequency of their pulse output signal while measuring the time to fill up a known volume of water for different levels of flows. Measured data are presented in Figure 10.6. The known volume consists of a 23 liters glass damejeanne, calibrated using a calibrated scale resulting in an accuracy of approximately 0.5% considering the weight of the water.

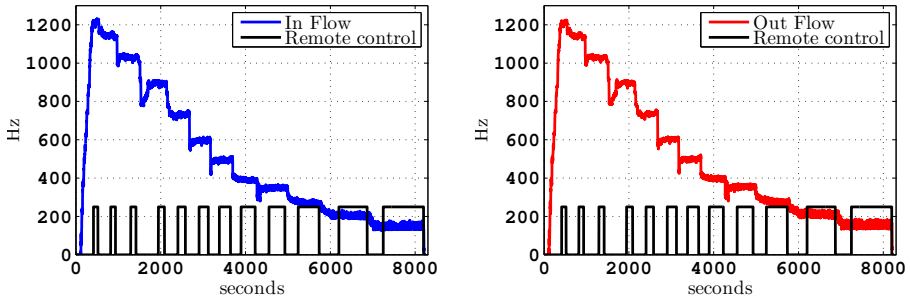

(a) In flow.

(b) Out flow.

Figure 10.6: Measured frequency during flow sensor calibration. The remote control signal is used for time measurements.

The least square error fit of a linear function to each of the sensor measurements are presented in Figure 10.7. The slope of the two lines are more or less identical, the difference will correspond to 0.1 l/min at 1000 Hz which is turn corresponds to a difference less than 1% for these flow levels. But there is a non-negligible

offset of 0.15 l/min, corresponding to 7.5% at a flow level of 2 l/min.

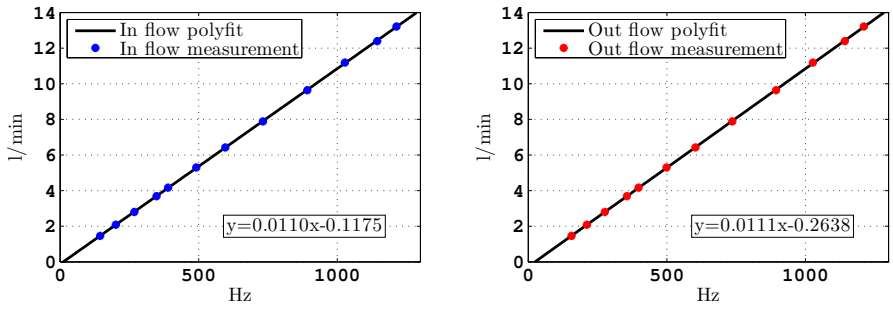

(a) In flow.

(b) Out flow.

Figure 10.7: Polyfit lines of measured water flow.

10.1.5 The thermal connection to the surroundings

In this section, the thermal connection to the surroundings is investigated in order to increase the repeatability and the control of the thermal measurements rather than calibrating for colorimetric measurements. Three main paths for heat transfer between the machine and the surroundings are identified: between the machine housing and the ambient, between the machine flange and the mounting flange, between the rotor and the ambient via the shaft. The first two are decreased by adding additional material barriers to increase their thermal resistance.

In Figure 10.8, the two positions where the water temperature and the water flow measured at the inlet and the outlet respectively are shown. The water outlet is located on the top in order to ventilate the air out of the cooling system. Both the hoses for the cooling water and the machine housing is covered by Armaflex insulation to reduce the convective coupling to the surrounding air. If only considering the 25 mm Armaflex sheet insulation that is covering the simplified machine housing geometry shown in Figure 10.9a, the resulting thermal resistance between the inner surface and the outer surface is calculated to 2.1 K/W (including both the half symmetries of a totally enclosed envelope) by means of FEA.

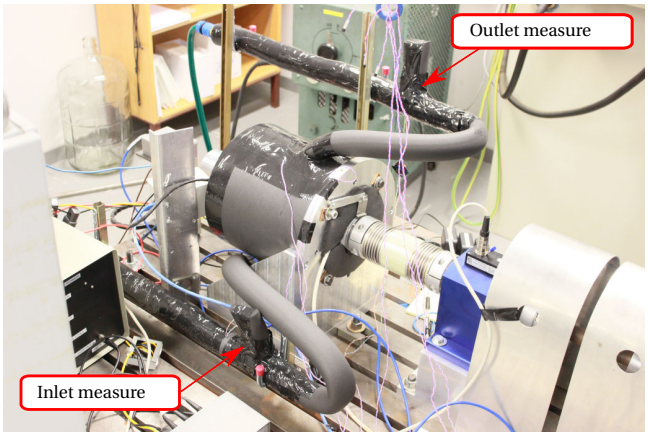

Figure 10.8: The experimental setup in the lab, where the locations of the water flow and temperature measurements are marked out.

The conductive coupling between the machine flange and the mounting flange is reduced by adding a 2 mm thick bakelite sheet between the contact surfaces of the flanges. The FEA model that is used to calculate the thermal resistance between the two flanges is shown in Figure 10.9b. Constant temperatures are put on the bakelite surface where the machine is mounted and to the bottom of the mounting flange, where it is attached to the test bench. Considering the calculated average temperature in the bolt holes, the bakelite surface temperature and the heat flow, an equivalent thermal resistance of 0.17 K/W is calculated.

The thermal resistance of the shaft is calculated by adding a constant temperature on the surface where the rotor stack is attached and to the two ends of the shaft. In this way, the thermal coupling via the bearings is not taken into account. The equivalent resistances are calculated to 7.2 K/W and 2.9 K/W for the hollow and the solid end of the shaft respectively. The two resistances in parallel result in an equivalent thermal resistance of 2.1 K/W.

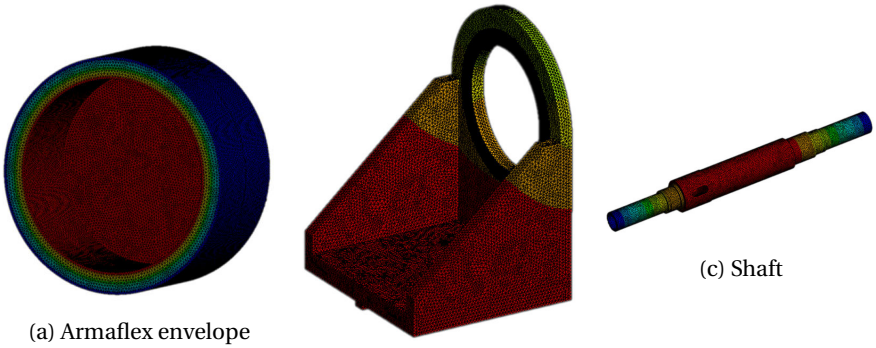

(a) Armaflex envelope

(b) Mounting flange

(c) Shaft

Figure 10.9: FEA models used to estimate the thermal resistance to the ambient.

The estimated heat transfer as function of the temperature difference over the calculated thermal resistances are shown in Figure 10.10. At a given temperature, the heat transfer via the mounting flange is significantly higher than via the shaft and the Armaflex envelope. On the other hand, the temperature gradients both between the flanges and across the Armeflex envelope are strongly related to the ambient temperature in the lab and the temperature of the cooling water. It is therefore possible to limit the heat transfer via these paths by using a cooling water temperature close to the ambient temperature in the lab.

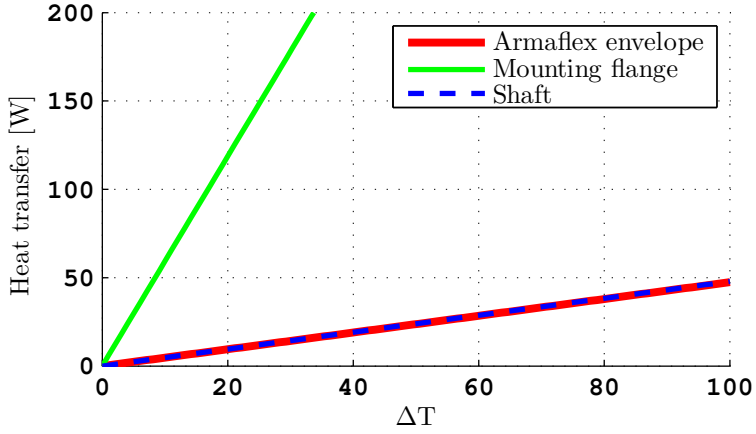

Figure 10.10: Estimated heat transfer as function of the temperature difference, ΔT.

10.2 Measured characteristics in the $i_d i_q$ -plane

In this section, the measured characteristics of the experimental machine in the $i_d i_q$-plane are presented. The measurements are carried out for a number of operating points, both for three phase operation and for phase open circuit operation, without reaching a thermal steady-state at each operating point. Instead, the machine is well cooled in order to reduce the temperature variations between operating points and the temperatures are also monitored during the measurements. The measurement of each operating point is executed in three steps:

- **Current measurement**, the machine is rotating and the current reference is put according to the present operating point while a set of AC measurements are carried out.
- **Back-EMF measurement**, the machine is rotating but the current reference is put to zero while a second set of AC measurements are performed.
- **Resistance measurement**, the machine is stopped and a DC voltage is applied and DC voltages and currents are measured.

The measurement results are compared with the results from the FEA, presented in section 8.4. Additionally, the magnetic coercivity of the permanent magnets are updated in the FEA according to the measured back-EMF.

10.2.1 Three phase operation

Measured operating points

The measured operating points during balanced three phase operation, presented in the $i_d i_q$-plane in the same manner as in Chapter 8, are shown in Figure 10.11. The reason for the discrepancy between the reference and the measured current, starting for quadrature currents of around 15 A, is that there was a mismatch between the actual DC-link voltage and the DC-link voltage value defined in the current controller. The DC-link voltage was increased during the measurements, and it was decided to use the resulting current values provided by the power analyzer instead of remeasuring the map.

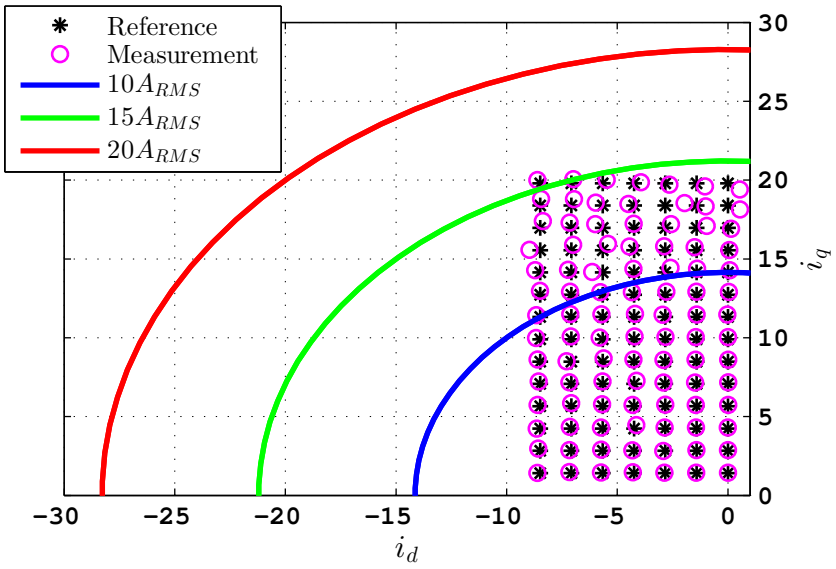

Figure 10.11: Measured operating points together with references to the controller.

Permanent magnet flux linkage calibration

It is observed that the measured torque is lower during the measurements compared to the FEA.The discrepancy increases when the current is increased, which may imply a deviation of the permanent magnet flux linkage. A calibration of the magnetic coercivity of the permanent magnets in the FEA model is therefore carried out, based on the measurements. The permanent magnet flux linkage, Ψ_m, calculated from the measured phase back-EMFs and PLL-frequencies for all the 98 operating points is shown in Figure 10.12. The reason for the step between operating point number 49 and 50 is that the measurements were carried out over two days, with a new starting temperature the second day. An average from all of the three phases is represented by the solid black line at 0.448 Wb. The highest and the lowest values are shown by the dashed black lines and are located +0.5% and -0.8% with respect to the average permanent magnet flux linkage.

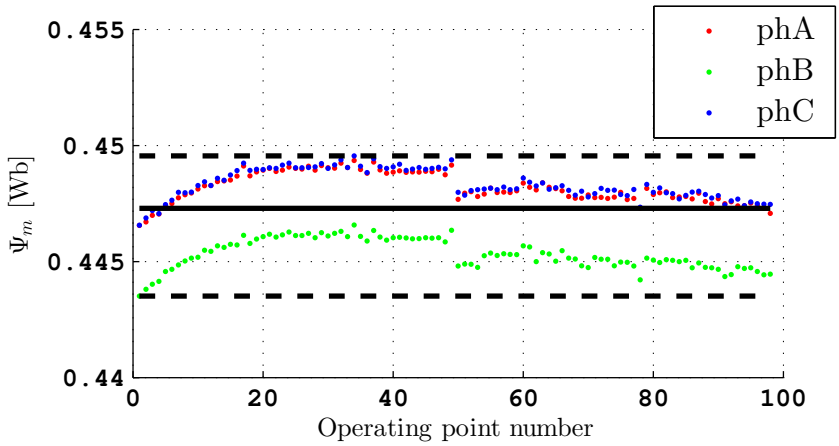

Figure 10.12: Permanent magnet flux linkage, Ψ_m, based on measured phase back-EMFs and PLL-frequencies for the 98 three phase operating points.

The magnetic coercivity of the permanent magnets in the FEA model is consequently altered, as shown in Figure 10.13. A magnetic coercivity of about 840 kA/m is found to give the best match between the FEA model and the measured average permanent magnet flux linkage. This is about 6% lower than the 890 kA/m in the data provided by the manufacturer.

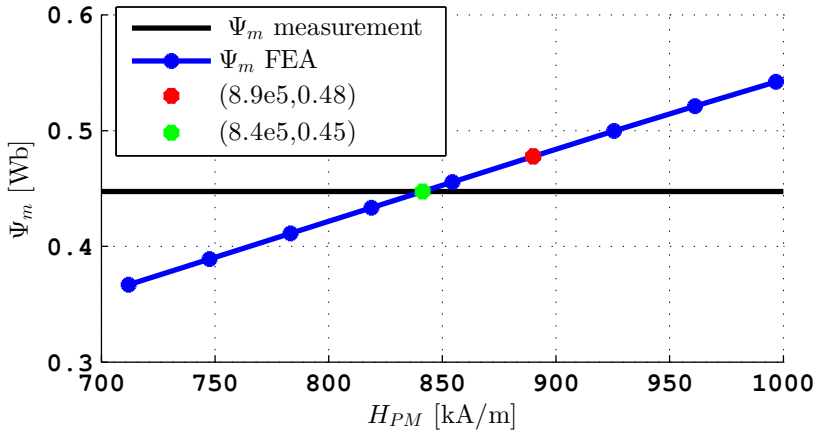

Figure 10.13: FEA permanent magnet magnetic coercivity calibrated towards the average of the measured permanent magnet flux linkage, presented in Figure 10.12.

Torque in the $i_d i_q$ -plane

The measured torque in the $i_d\,i_q$-plane is represented by the black lines in Figure 10.14, while the red lines correspond to FEA using the magnet magnetic coercivity of 890 kA/m in Figure 10.13 which is also used when producing Figure 8.9. It can be noticed that there is an offset between the measurements and the non-calibrated FEA (red lines), while this offset is reduced for the calibrated FEA (green lines) where the magnet magnetic coercivity is reduced to 840 kA/m according to the calibration towards the back-EMF measurements in Figure 10.13. Another observation is that the calibration corrects the calculation of the permanent magnet torque well but the curves tend to diverge with an increased reluctance torque, implying that the discrepancy of the non-calibrated FEA is not caused by the permanent magnet strength only.

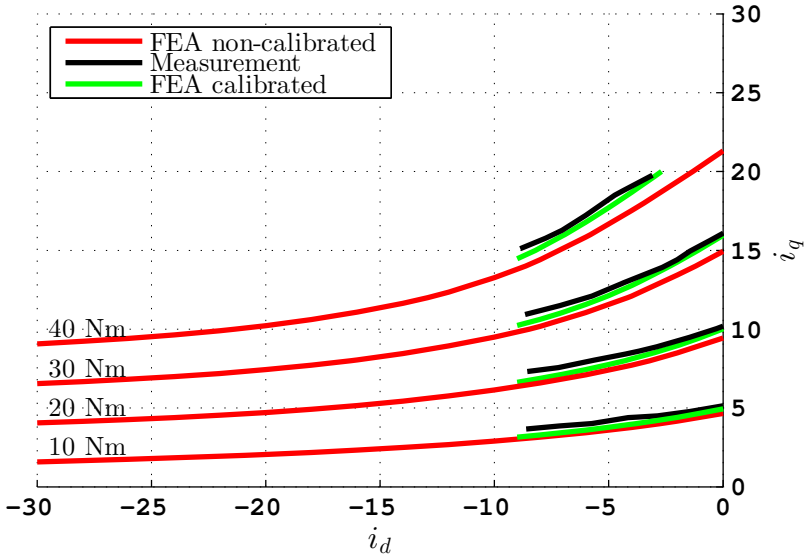

Figure 10.14: Measured and calculated torque in the $i_d\,i_q$-plane during three phase operation.

10.2.2 Operation during open circuit fault

Measured operating points

The measured operating points during phase open circuit operation, presented in the $i_d\,i_q$-plane, are shown in Figure 10.15. The references are given to the controller in the global dq-reference frame (see section 2.5.3) and the results cannot be measured directly, instead the phase currents are measured and transformed

back to the global dq-reference frame, see (2.36). The arcs of the currents mark out the phase RMS currents needed for a given operating point in the gloabal dq-reference frame. It can be noticed that phase currents of 11.8 A_{RMS} are needed to reach the measured operating point farthest out in the $i_d\,i_q$-plane.

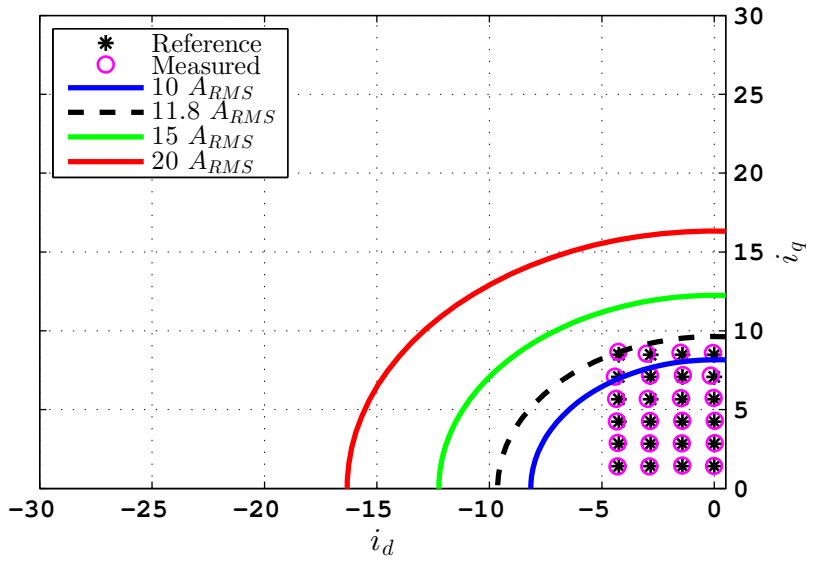

Figure 10.15: Measured operating points together with references to the controller.

The measured phase currents when using the proposed current controller in section 2.5.3 can be seen in Figure 10.16, where the current amplitudes and the current phase angles are displayed separately. It can be seen that the amplitudes of the two phase currents are more or less identical and a factor $\sqrt{3}$ greater than the reference in the global dq-reference frame. Further, it can also be confirmed that their respective phase angles are symmetrically displaced, ±30° around the reference angle in the global dq-reference frame (here 0° represents current in the direction of the quadrature axis).

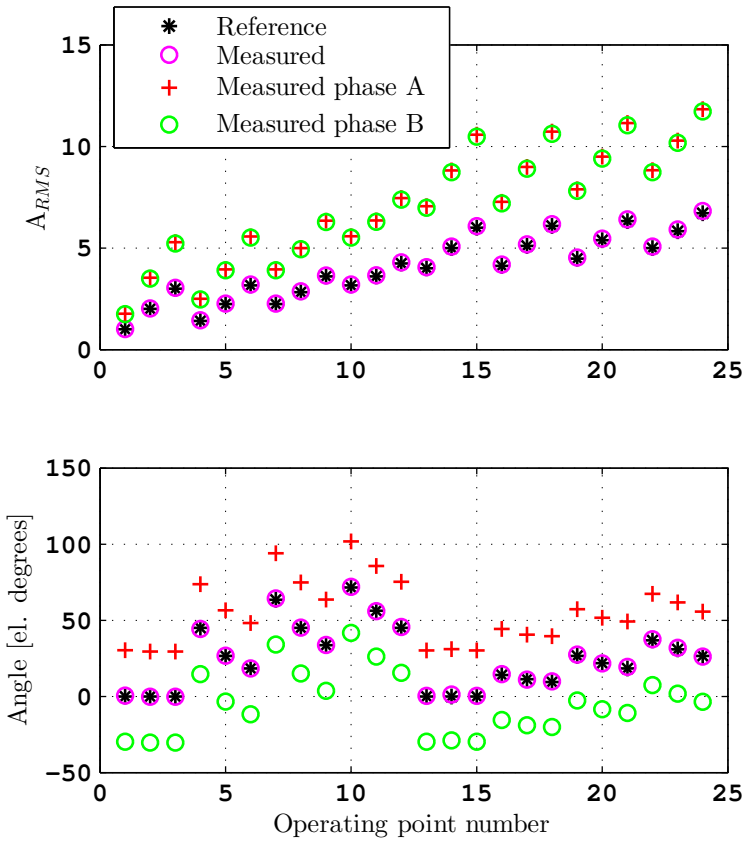

Figure 10.16: Measured operating points together with references to the controller.

Torque in the $i_d i_q$ -plane

In Figure 10.17, the measured torque during open circuit operation is shown together with the torque using FEA in the same manner as in Figure 10.14. The overall picture is similar to the three phase operation, there is an offset between the measured values and the non-calibrated FEA (red lines) and the offset is reduced in the calibrated FEA (green lines), when using the permanent magnet magnetic coercivity corresponding to the back-EMF measurements.

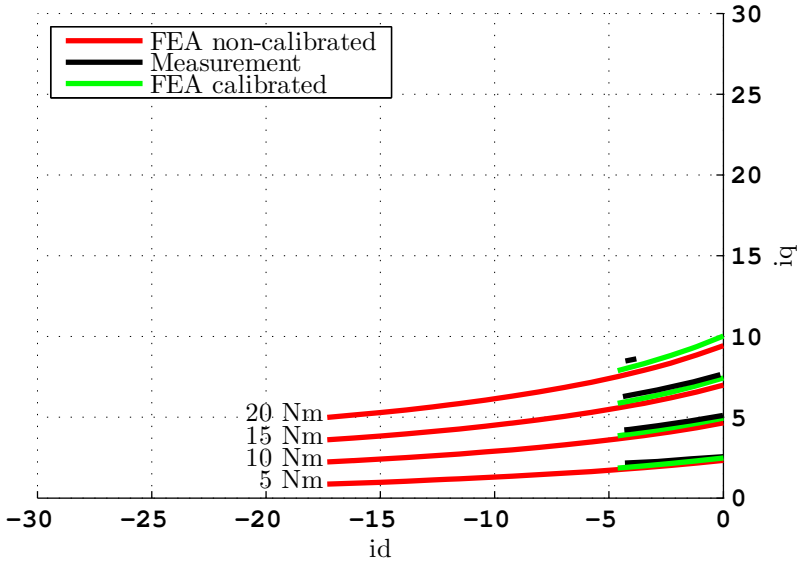

Figure 10.17: Measured 2-phase torque in the $i_d\,i_q$-plane

To sum up, the torque predicted by the FEA agrees well with the measurements, both in case of three phase operation and during open circuit fault operation. A small improvement, mainly along the i_q-axis in the $i_d\,i_q$-plane, was achieved when calibrating the magnetic coercivity of the PMs based on the back-EMF measurements. However, the discrepancy of the reluctance torque component remains and this may imply a minor deviation in the BH-curve used in the FEA.

10.3 Transient measurements

The measurements presented in this section correspond to a drive cycle where the machine is operated to alternate between two operating points at 100 rpm. In one cycle of 10 minutes, the current reference is put to a value corresponding to approximately 10 Nm for 5 min and 20 Nm for the remaining 5 min. In order to make temperature and water flow traces visible in the figures, they are all filtered by a moving average filter of 11 samples defined by

$$x_n = \frac{1}{11}\sum_{i=n-5}^{i=n+5} x_i \tag{10.1}$$

but the presented average values are calculated over the whole windows with-

out the filter.

Including preparations, post processing etc. it is possible to carry out one measurement series during one day in the lab. The reference signal to the current controller is therefore low pass filtered to make sure that no protection devices were triggered during the day. That is the reason why it takes a few seconds (≈10s) to change operating point, which can be seen in the presented measurements. This drive cycle is evaluated both during three phase operation and during two phase operation, representing a phase open circuit fault. In both cases, the machine is operated for around four hours, while the presented measurements represents the last 30 minutes only. Except for the variations in the cooling water flow and temperature, the last 30 minutes can be considered as a periodic thermal steady state.

10.3.1 Three phase operation

The measured phase currents during the 20 Nm torque level in the drive cycle are presented in Figure 10.18. The current reference is put to $i_d^* = -2.89$ A and $i_q^* = 8.89$ A, which corresponds to a peak value of 9.34 A.

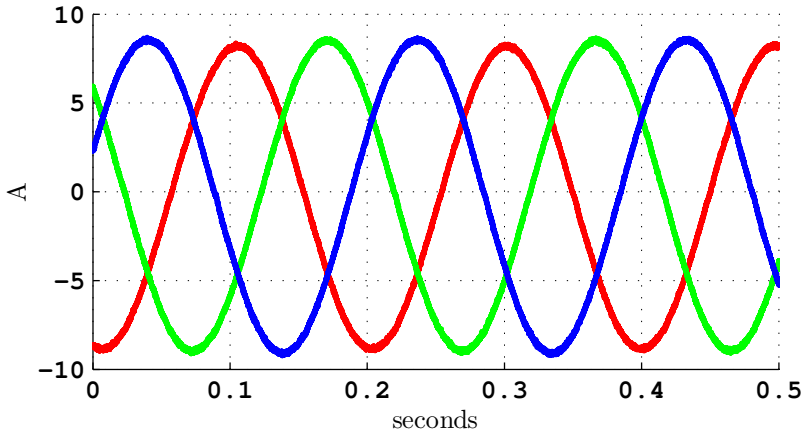

Figure 10.18: Measured phase currents for 3 phase operation at 20 Nm.

In Figure 10.19, the measured torque during the last 30 minutes is shown. The torque is measured every 15$^{\text{th}}$ second as an average over an electrical period using the PLL algorithm of the power analyzer.

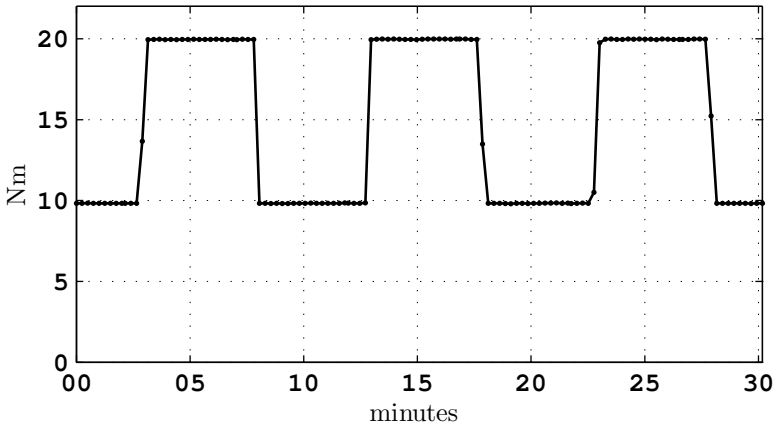

Figure 10.19: Measured torque pulsations.

Measured winding temperatures from the six sensors attached to the windings are shown in Figure 10.20. It can be noticed that the temperature difference between the sensors is greatest in the end of a 20 Nm pulse, which is reasonable as the copper loss and the transferred heat are expected to be at their maximum.

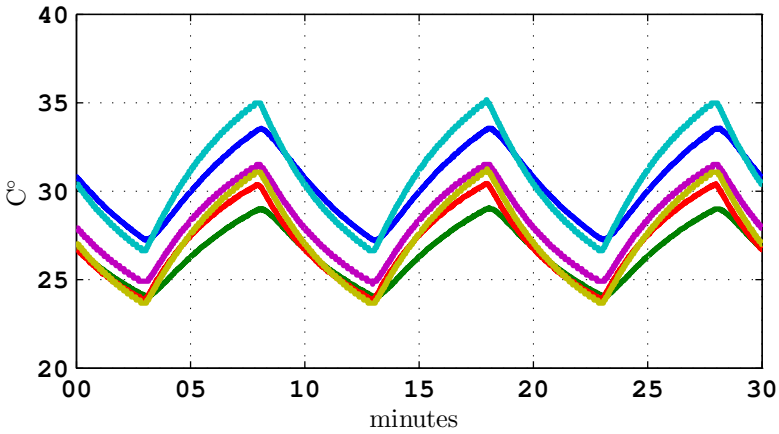

Figure 10.20: Measured winding temperatures.

The stator iron temperatures are shown in Figure 10.21. By a visual comparison of Figure 10.21 and the inlet water temperature, presented in Figure 10.23 later, it can be observed that the water temperature is more or less directly superimposed on the stator iron temperatures.

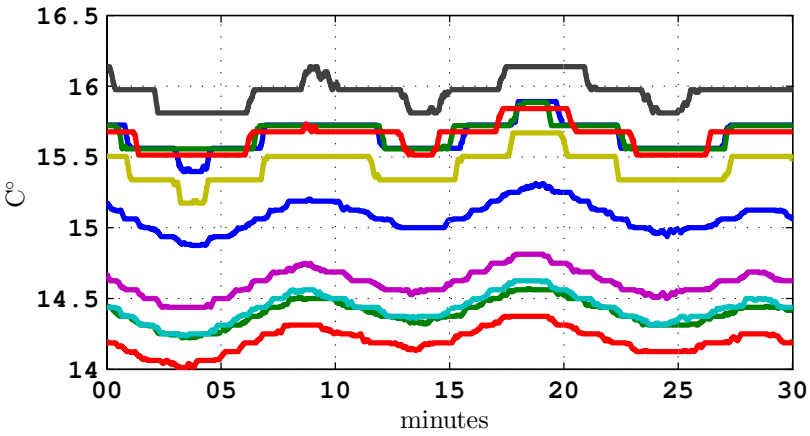

Figure 10.21: Measured temperatures in stator iron.

The measured rotor temperatures are presented in Figure 10.22, where the thermal oscillations due to the torque pulses are filtered out completely in some locations.

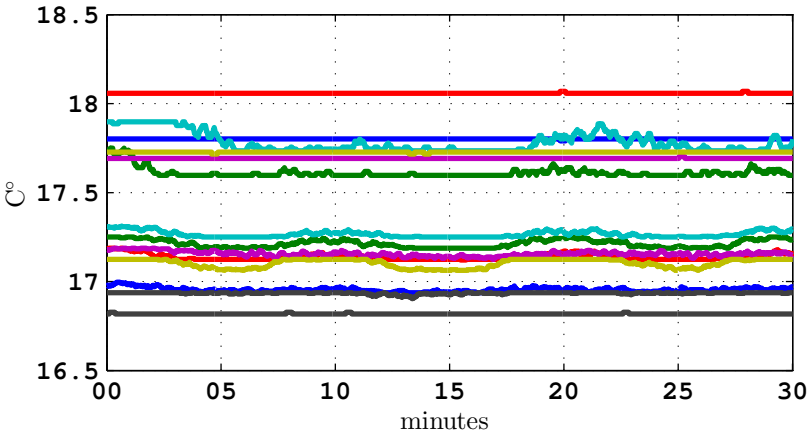

Figure 10.22: Measured rotor temperatures.

Figure 10.23 shows how the water inlet and outlet temperatures vary over the 30 minutes of measurements. The inlet temperature varies between 13.25°C and 13.50°C while the outlet temperature varies between 13.70°C and 13.94°C

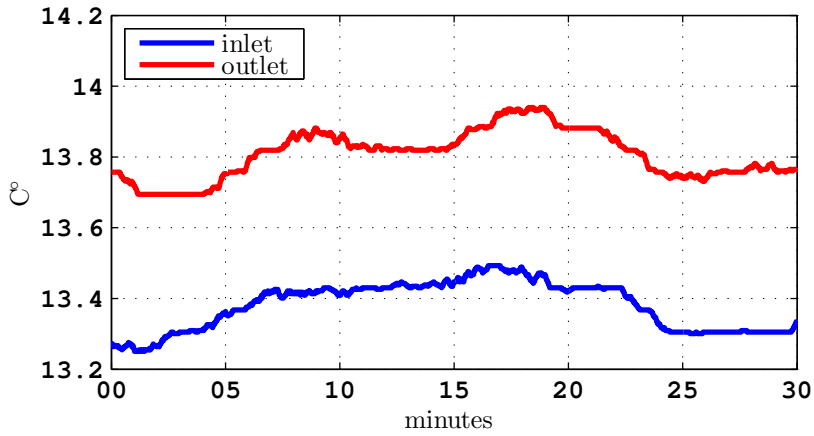

Figure 10.23: Measured water temperatures.

The water flow measured by the two flow sensors is presented in Figure 10.24. There is an offset between the two sensors, which can also be seen in the figure. The calculated difference between the average inlet flow and the average outlet flow, during the 30 minutes in Figure 10.24, is 0.0037 liters per minute. Considering the calculated average flow of both the sensors during the 30 minutes which is 1.82 l/min, the relative average difference is 0.20%.

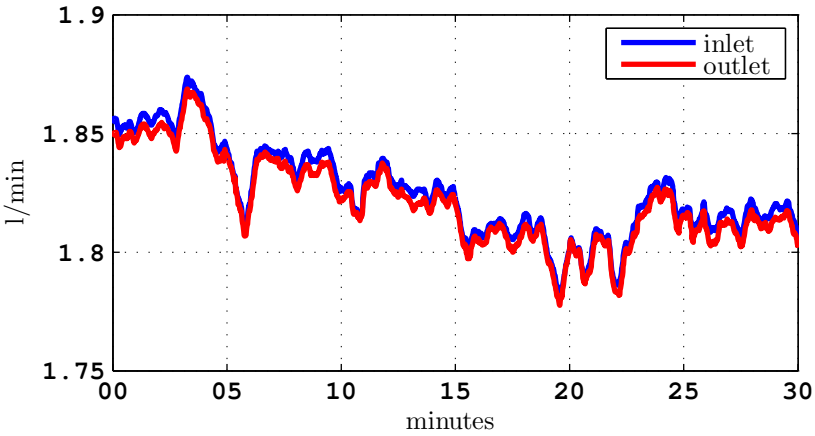

Figure 10.24: Measured water flow.

The calculated cooling power, which is based on the difference between inlet and outlet water temperatures presented in Figure 10.23 and the average of the

two water flows in Figure 10.24, is shown in Figure 10.25. In the cooling power it is possible to identify both variations due to the water temperature and water flow but also the periodic pattern due to the driving cycle. According to the measurements, the average heat transfer via the water cooling system is 54 W during the 30 minutes. This number agrees well with the calculated total loss distribution, presented in Figure 7.12a.

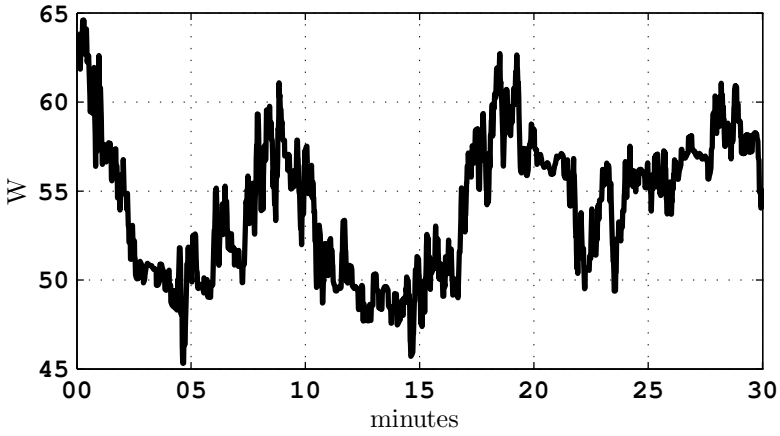

Figure 10.25: Calculated cooling power based on water inlet and outlet temperatures together with the measured water flow.

10.3.2 Operation during open circuit fault

The two measured phase currents together with the return current from the "neutral point" during open circuit operation and the 20 Nm torque level is shown in Figure 10.26. The current reference is put to i_d^*=-3.81 A and i_q^*=8.62 A, which corresponds to a peak value of 9.43 A in the global dq-reference frame. Hence, the expected peak phase currents are $9.43\sqrt{3}$=16.32 A and the peak return current $16.32\sqrt{3}$=28.27 A.

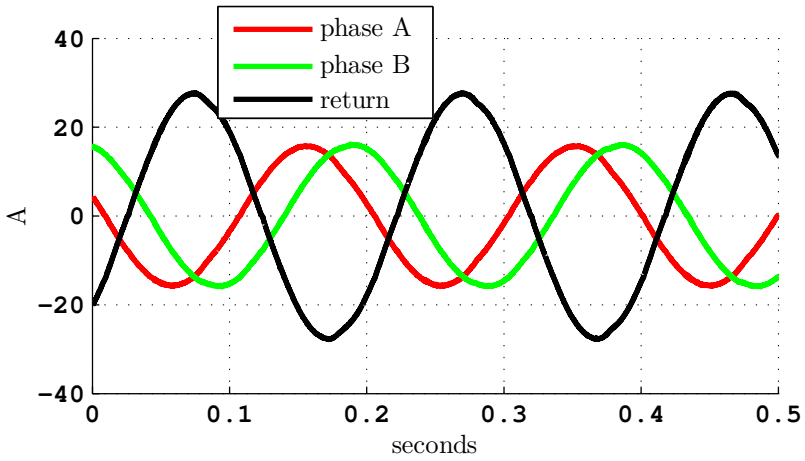

Figure 10.26: Measured phase and return current for 2 phase operation at 20Nm.

The measured torque during the last 30 minutes of open circuit operation is presented in Figure 10.27. The torque is measured every 15th second as an average over an electrical period using the PLL algorithm of the power analyzer, in the same manner as during the three phase operation earlier.

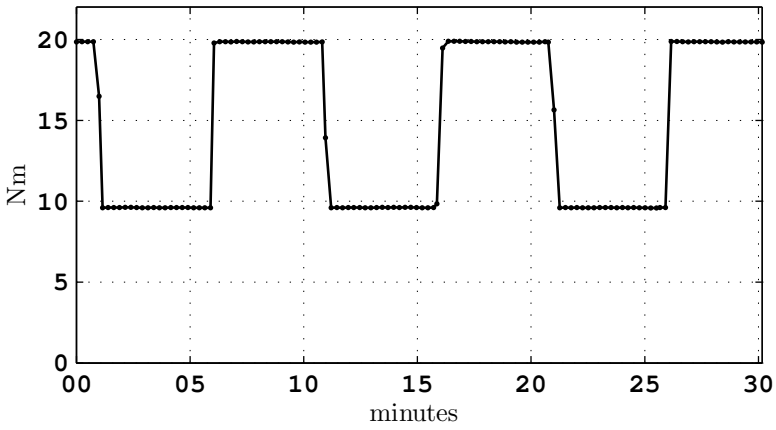

Figure 10.27: Measured torque pulsations.

The temperatures from the six monitored winding temperatures are shown in Figure 10.28. The peak temperature of the sensors spreads between 24.92°C and 61.86°C, which can be compared to 29.06°C and 35.17°C during the three phase operation in Figure 10.20 previously.

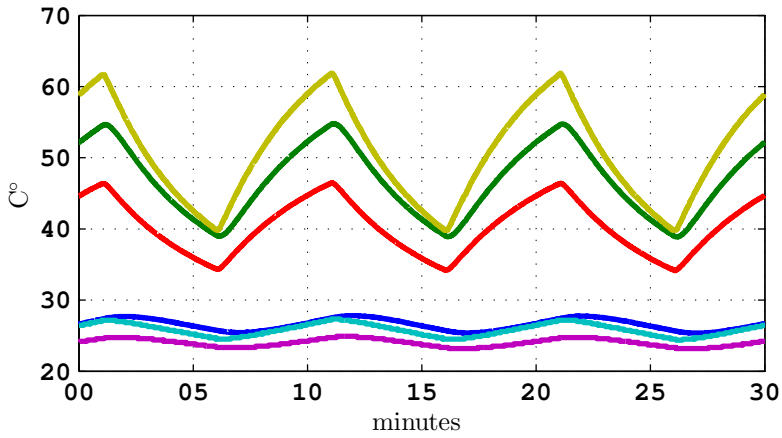

Figure 10.28: Measured winding temperatures.

The measured stator iron temperatures during open circuit operation are presented in Figure 10.29. The min and max temperatures during the 30 minutes are 14.05°C and 17.79°C respectively. The corresponding measured min and max temperatures during three phase operation, shown in Figure 10.21, are 14.01°C and 16.14°C respectively. This may imply that there is a slightly greater thermal gradient over the stator structure during two phase operation. When comparing the temperature of the inlet water (Figure 10.23 and Figure 10.31) there are on the other hand greater fluctuations during the measurements of the two phase operation. In the location of the sensor showing the lowest temperature in Figure 10.29, it is clear that the temperature is strongly coupled to the inlet water temperature, shown in Figure 10.31.

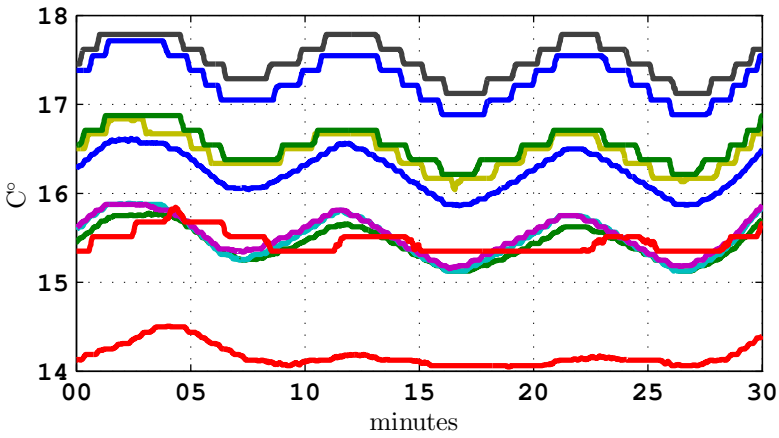

Figure 10.29: Measured temperatures in stator iron.

Measured temperatures in the rotor during open circuit operation is shown in Figure 10.30. In some sensor positions, the thermal oscillations due to the torque pulsations are filtered out completely, which is also the situation during three phase operation, shown in Figure 10.22.

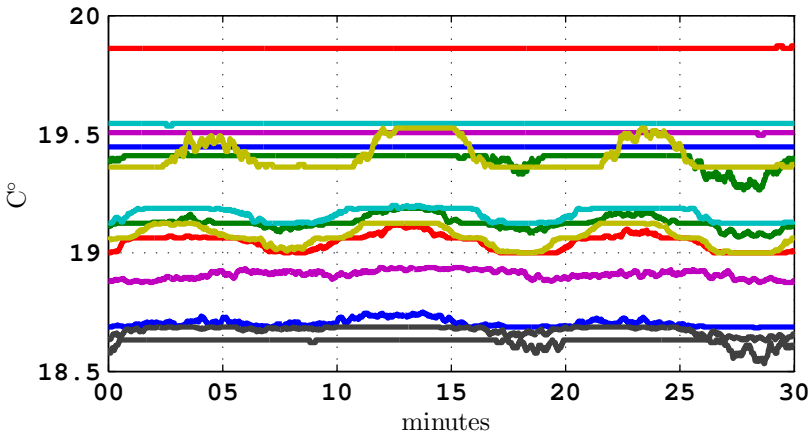

Figure 10.30: Measured rotor temperatures.

Due to the relatively long thermal time constant of the rotor, its temperature is not directly influenced by the relatively fast variations in cooling water flow and temperature, at least not to the same extent as the stator temperatures. Dur-

ing the 30 minutes of open circuit operation the min and max temperatures are 18.53°C and 19.87°C respectively. The corresponding max and min temperatures during three phase operation in Figure 10.22 are 16.82°C and 18.07°C. At the same time, the average water flow and temperature are 2.08 l/min (Figure 10.32) and 13.01°C (Figure 10.31) during open circuit operation while they are 1.82 l/min (Figure 10.24) and 13.38°C (Figure 10.23) during three phase operation. If the effect of turbulence through the water cooling system is assumed to be negligible for these small variations, the average water flow over the average water inlet temperature is 2.08/13.01=0.16 l/(min°C) during two phase operation and 1.82/13.38=0.14 l/(min°C) during three phase operation, which indicate that the machine was better cooled during the two phase operation than during the three phase operation. The higher measured rotor temperatures together with the indication of a better cooled machine confirm a higher loss level during two phase operation compared with three phase operation, as expected.

Figure 10.31 shows how the water inlet and outlet temperatures vary during the last 30 minutes of open circuit operation. The inlet varies between 12.83°C and 13.49°C while the outlet temperature varies between 13.63°C and 14.20°C.

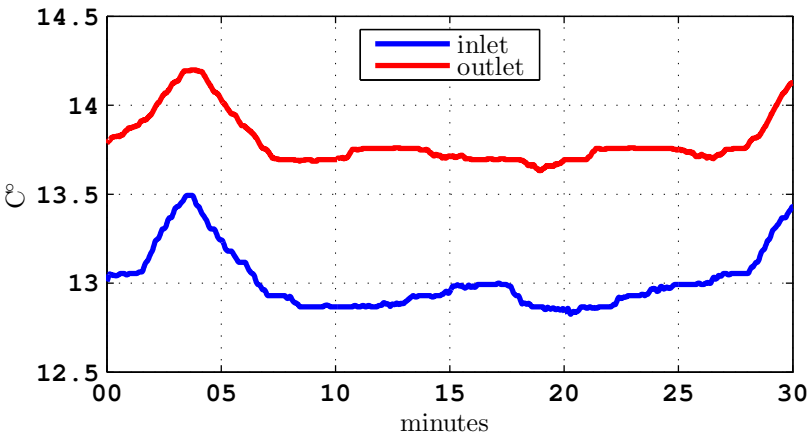

Figure 10.31: Measured water temperatures.

The measured water flow during 30 minutes of open circuit operation is shown in Figure 10.32. The difference between the average inlet and outlet flow during the 30 minutes is 0.012 l/min. The calculated average flow of both the sensors is 2.08 l/min and the calculated relative average difference is then 0.56%.

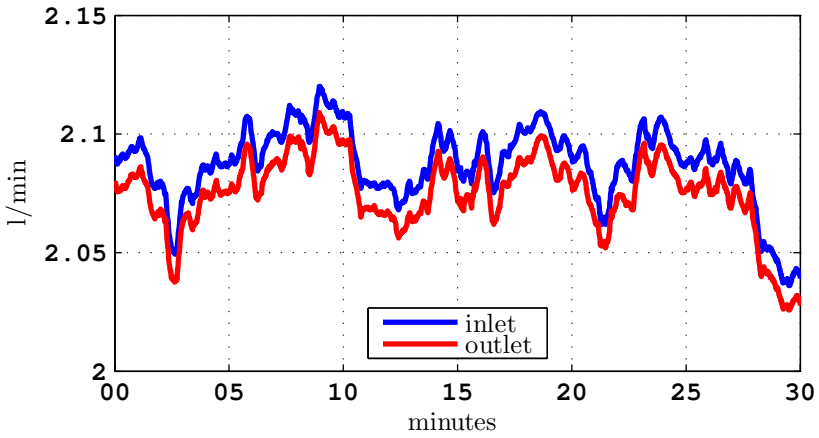

Figure 10.32: Measured water flow.

The cooling power during open circuit operation is calculated in the same manner as for three operation, shown in Figure 10.25. According to the measurements, the average heat transfer via the water cooling system is 114 W during the 30 minutes of measurements of open circuit operation. This number agrees well with the calculated total loss in Figure 7.12b and it is about twice as much as the 54 W measured for three phase operation of the same drive cycle.

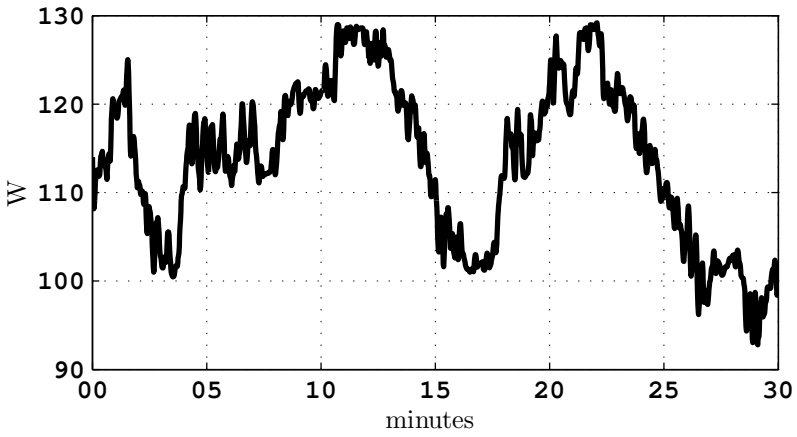

Figure 10.33: Measured cooling power.

Without an active control of the inlet water temperature and the water flow, it is not possible to reach a pure periodic steady-state. However, i the regions where

the temperatures are as most critical, i.e. rotor and windings, the fluctuations are filtered out quite well.

Chapter 11

Conclusions and future work

11.1 Conclusions

In this thesis, a fault-tolerant fractional slot machine with a similar size and performance as the Toyota Prius 2004 machine is designed. The faults investigated are single phase open circuit and single phase short circuit, and it is shown that the thesis machine design can be operated during both circumstances. The characteristics of the fault-tolerant thesis machine design are compared with the Prius 2004 and a smaller prototyped IPM machine, both during normal operation and phase open circuit fault operation. The electromagnetic design of the machines have been compared with the use of 2D finite element analysis, and also including measurements for the prototyped machine.

During normal operation, the calculated overall efficiency of the final thesis design turned out to be slightly higher than that of the 2004 Prius design, in case of segmented permanent magnets. The estimated material cost to produce a machine is included already in the design process, where four design variables are varied. In that way, the most promising designs considering both performance and cost were sorted out. The estimated material cost of the finally selected machine design is about 8% higher and the peak torque slightly lower (364 Nm) than the 2004 Prius design (374 Nm).

All the three machines are evaluated during single phase open circuit operation by controlling the phase currents in the classical vector control manner to maintain constant currents in the dq reference frame. It is found that the maximum torque is reduced (for all three machines) to approximately $1/\sqrt{3}\approx58\%$ compared to normal operation. Without a constant speed load profile, providing the torque requirement for a given vehicle speed, it is not possible to determine the reduction of the maximum vehicle speed; but in rough numbers about 1/2 of the maximum speed of 6000 rpm during normal operation is achievable for

the fault-tolerant thesis design.

It is further shown that the torque ripple of a PMSM may increase when operated under unbalanced conditions due to unbalanced saturation. It is clear that unbalanced saturation is prominent in two of the machine designs, while it is less noticeable in the the third (the smaller prototyped IPMmachine), when they are operated during a single phase open circuit fault. A greater impact of unbalanced saturation can be expected for designs with a relatively high magnetic loading (high PM flux densities), especially in combination with high phase inductance. A high magnetic loading gives a no-load flux density, high up on the BH-curve and already close to non-linearity. The difference in flux densities in the phases, due to the rearranged currents when operating during a fault, is enhanced by high phase inductances. Therefore, it is of great importance to consider the unbalanced saturation in these types of machines, as is noticed in section 8.5.

Furthermore, the thermal limits of the thesis design and the prototyped machine are evaluated during normal and single phase open circuit operation. Considering the thermal limit of the windings, when the machines are operating during current limitation in the low speed region, it is concluded that the thermal limit follows the electrical limit. This can be explained by the fact that the temperature of a winding is determined more or less only by its own current level.

Finally, a semi-analytical machine modeling approach is introduced and used to model the individual saturation levels of the phases successfully. Harmonics can be included in the phase currents to increase the torque quality but the area of possible operating points is reduced substantially. It is shown that it is possible to reduce the torque ripple by approximately 50%, when compensating for the unbalanced saturation, when the fault-tolerant fractional slot machine is operated during a phase open circuit fault at 175 Nm. The maximum torque is reduced by approximately 50% and can be maintained up to about 600 rpm in case of an open circuit fault, compared to about 1300 rpm at normal operation. In case of a short circuit fault, the maximum torque varies within the whole speed operating range, due to the braking torque produced by the short circuited phase. The starting torque, when the short circuit torque is negligible, is of course reduced to approximately 50% also in case of a short circuit fault when compensating for unbalanced operation. The higher voltage required for the current harmonics results in maximum speeds of roughly 1/3 or slightly below 1/4 of the maximum speed of 6000 rpm during normal operation, in case of an open circuit fault or a short circuit fault respectively.

11.2 Future Work

Here follow some suggestions for future work, either parts that were consciously not included in this work or as reflection over the thesis and its results.

- When the cost efficiency of the electric machine designs were evaluated, only the torque production at low speed was included. It is possible to improve the process by adding more properties in order to sort out the most promising candidates in a more effective manner. For example, the field weakening characteristics and the thermal restrictions of electric loading could be evaluated at the same time. It is also possible to reformulate the constraint instead of using a single break point of above 95% of the maximum torque output per cost.
- Investigate the effect of the DC-link current ripple in relation to both performance and comfort when operating during fault.
- Analyze the radial forces between the stator structure and the rotor, where one aspect is the higher radial forces associated with concentrated windings in comparison with distributed windings. Another interesting aspect is the impact on the radial forces during unbalanced operation, when the machines are operated during a fault.
- Fractional slot machines with concentrated windings are often regarded as suitable choices for design of fault-tolerant machines. At the same time, one of the major issues that is often raised regarding this types of machines is the rotor losses and the permanent magnet losses. The calculated lower permanent magnet losses when operating during phase open circuit fault compared to normal operation in this thesis is therefore of great interest to investigate further, both using 3D FEA and measurements.
- Complete electric drive system modeling including both machine and converter models but also the control and fault detection.
- There are commercial fractional slot concentrated winding PMSM available on the market, some of them are potentially of suitable pole/slot configurations for unbalanced operation during fault. That would be interesting to investigate and test experimentally.
- Compare the results with other fault-tolerant solutions; it could be multiphase systems with a separate converter and machine or modular systems where the winding terminals are attached directly to the power electronics.
- Combine an electric drive system model with a vehicle model in order to evaluate fault-tolerant vehicle performance more precisely.

Bibliography

[1] A. El-Refaie, "Fault-tolerant permanent magnet machines: a review," *IET Electric Power Applications*, vol. 5, no. 1, pp. 59–74, 01 2011.

[2] K. Rajashekara, "Present status and future trends in electric vehicle propulsion technologies," *Emerging and Selected Topics in Power Electronics, IEEE Journal of*, vol. 1, no. 1, pp. 3–10, March 2013.

[3] O. Wallmark, L. Harnefors, and O. Carlson, "Control algorithms for a fault-tolerant pmsm drive," *Industrial Electronics, IEEE Transactions on*, vol. 54, no. 4, pp. 1973–1980, Aug 2007.

[4] D. Diallo, M. Benbouzid, and A. Makouf, "A fault-tolerant control architecture for induction motor drives in automotive applications," *Vehicular Technology, IEEE Transactions on*, vol. 53, no. 6, pp. 1847–1855, Nov 2004.

[5] A. Jack, B. Mecrow, and J. Haylock, "A comparative study of permanent magnet and switched reluctance motors for high-performance fault-tolerant applications," *Industry Applications, IEEE Transactions on*, vol. 32, no. 4, pp. 889–895, Jul 1996.

[6] N. Bianchi and S. Bolognani, "Fault -tolerant pm motors in automotive applications," in *Vehicle Power and Propulsion, 2005 IEEE Conference*, Sept 2005, pp. 747–755.

[7] M. Abolhassani and H. Toliyat, "Fault tolerant permanent magnet motor drives for electric vehicles," in *Electric Machines and Drives Conference, 2009. IEMDC '09. IEEE International*, May 2009, pp. 1146–1152.

[8] A. EL-Refaie, "Fractional-slot concentrated-windings synchronous permanent magnet machines: Opportunities and challenges," *Industrial Electronics, IEEE Transactions on*, vol. 57, no. 1, pp. 107–121, Jan 2010.

[9] E. Fornasiero, *Advanced Design of Direct Drive PM Machines*. Ph.D. thesis, Department of Electrical Engineering, University of Padova, Padova,Italy, 2010.

[10] G. Dajaku and D. Gerling, "Low costs and high-efficiency electric machines," in *Electric Drives Production Conference (EDPC), 2012 2nd International*, Oct 2012, pp. 1–7.

[11] M. Barcaro, N. Bianchi, E. Fornasiero, and F. Magnussen, "Experimental comparison between two fault-tolerant fractional-slot multiphase pm motor drives," in *Industrial Electronics (ISIE), 2010 IEEE International Symposium on*, July 2010, pp. 2160–2165.

[12] A. Mitcham, G. Antonopoulos, and J. Cullen, "Favourable slot and pole number combinations for fault-tolerant pm machines," *Electric Power Applications, IEE Proceedings* -, vol. 151, no. 5, pp. 520–525, Sept 2004.

[13] B. Mecrow, A. Jack, J. Haylock, and J. Coles, "Fault-tolerant permanent magnet machine drives," *Electric Power Applications, IEE Proceedings* -, vol. 143, no. 6, pp. 437–442, Nov 1996.

[14] B. Welchko, T. Lipo, T. Jahns, and S. Schulz, "Fault tolerant three-phase ac motor drive topologies: a comparison of features, cost, and limitations," *Power Electronics, IEEE Transactions on*, vol. 19, no. 4, pp. 1108–1116, July 2004.

[15] Y. Crevits, X. Kestelyn, and E. Semail, "Investigation on vector control of three-phase synchronous machines under supply fault condition," in *Power Electronics, Electrical Drives, Automation and Motion, 2006. SPEEDAM 2006. International Symposium on*, May 2006, pp. 439–444.

[16] C. Gajanayake, B. Bhangu, S. Nadarajan, and G. Jayasinghe, "Fault tolerant control method to improve the torque and speed response in pmsm drive with winding faults," in *Power Electronics and Drive Systems (PEDS), 2011 IEEE Ninth International Conference on*, Dec 2011, pp. 956–961.

[17] N. Bianchi, S. Bolognani, M. Zigliotto, and M. Zordan, "Innovative remedial strategies for inverter faults in ipm synchronous motor drives," *Energy Conversion, IEEE Transactions on*, vol. 18, no. 2, pp. 306–314, June 2003.

[18] N. Bianchi, S. Bolognani, and M. Zigliotto, "Analysis of pm synchronous motor drive failures during flux weakening operation," in *Power Electronics Specialists Conference, 1996. PESC '96 Record., 27th Annual IEEE*, vol. 2, Jun 1996, pp. 1542–1548 vol.2.

[19] S. Bosga, *Asymmetrical supply of induction machines*. Ph.D. thesis, Technische Universitet Eindhoven Eindhoven, Eindhoven, The Netherlands, 1997.

[20] A. Krings and J. Soulard, "Overview and comparison of iron loss models for electrical machines," *Journal of Electrical Engineering*, vol. 10, no. 3, pp. 162–169, 2010, updated and revised version of conference paper from

the 5th International Conference and Exhibition on Ecological Vehicles and Renewable Energies (EVER 10), Monte-Carlo, MONACO, MAR 25-28, 2010QC 20120120.

[21] H. J.R. and M. T.J.E, *Design Of Brushless Permanent-Magnet Machines*. Motor Design Books LLC, Florida, 2010.

[22] J. Gieras, M. Kamper, and R.-J. Wang, *Axial Flux Permanent Magnet Brushless Machines 2nd Edition*. Springer Science & Business Media B.V., 2008.

[23] C. Liwschitz-Garik, M. assisted by Clyde and E. Whipple, *Electric Machinery, Volume 2 A-C Machines*. Van Nordstrand, New York, 1946.

[24] G. Dajaku, D. Gerling, and W. Xie, "Reduction of low space harmonics for the fractional slot concentrated windings using a novel stator design," *Magnetics, IEEE Transactions on*, vol. PP, no. 99, pp. 1–1, 2013.

[25] T. D. Strous, H. Polinder, and J. Ferreira, "Inductance calculations for pm machines with concentrated windings," in *Electric Machines Drives Conference (IEMDC), 2011 IEEE International*, May 2011, pp. 447–452.

[26] L. Svensson, M. Andersson, A. Reinap, and M. Alaküla, "Thermal properties on high fill factor electrical windings: Infiltrated vs non infiltrated," *International Conference on Electrical Machines (ICEM14), Berlin, Germany*, Sep 2014.

[27] A. Jack, B. Mecrow, P. Dickinson, D. Stephenson, J. Burdess, J. N. Fawcett, and T. Evans, "Permanent magnet machines with powdered iron cores and pre-pressed windings," in *Industry Applications Conference, 1999. Thirty-Fourth IAS Annual Meeting. Conference Record of the 1999 IEEE*, vol. 1, 1999, pp. 97–103 vol.1.

[28] R. Wrobel, P. Mellor, and D. Holliday, "Thermal modeling of a segmented stator winding design," *Industry Applications, IEEE Transactions on*, vol. 47, no. 5, pp. 2023–2030, Sept 2011.

[29] G. I. Taylor, "Distribution of velocity and temperature between concentric rotating cylinders," *Proceedings of the Royal Society of London A: Mathematical, Physical and Engineering Sciences*, vol. 151, no. 874, pp. 494–512, 1935. [Online]. Available: http://rspa.royalsocietypublishing.org/content/151/874/494

[30] K. M. Becker and J. Kaye, "Measurements of diabatic flow in an annulus with an inner rotating cylinder," *Journal of Heat Transfer*, vol. 84, no. 2, pp. 97–104, May 1962.

[31] J. Nerg, M. Rilla, and J. Pyrhonen, "Thermal analysis of radial-flux electrical machines with a high power density," *IEEE Transactions on Industrial Electronics*, vol. 55, no. 10, pp. 3543–3554, Oct 2008.

[32] R. Krishnan, *Permanent Magnet Synchronous and Brushless DC Motor Drives*. Hoboken: CRC Press, 2009. [Online]. Available: www.summon.com

[33] G. Kron, *The Application of Tensors To the Analysis of Rotating Electrical Machinery*. General Electric Review, Schenectady, N.Y., U.S.A., 1938.

[34] W. Soong and T. Miller, "Theoretical limitations to the field-weakening performance of the five classes of brushless synchronous ac motor drive," in *Electrical Machines and Drives, 1993. Sixth International Conference on (Conf. Publ. No. 376)*, Sep 1993, pp. 127–132.

[35] L. Chong, R. Dutta, N. Dai, M. Rahman, and H. Lovatt, "Comparison of concentrated and distributed windings in an ipm machine for field weakening applications," in *Universities Power Engineering Conference (AUPEC), 2010 20th Australasian*, Dec 2010, pp. 1–5.

[36] T. A. O. Burress, S. L. O. Campbell, C. O. Coomer, C. W. O. Ayers, A. A. O. Wereszczak, J. P. O. Cunningham, L. D. O. Marlino, L. E. O. Seiber, and H.-T. O. Lin, *Evaluation of the 2010 Toyota Prius Hybrid Synergy Drive System*, Mar 2011. [Online]. Available: http://www.osti.gov/scitech/servlets/purl/1007833

[37] ANSYS, "Study of a permanent magnet motor with maxwell 2d : Example of the 2004 prius ipm motor," unpublished. [Online]. Available: http://www.ansys.com

[38] R. Staunton, C. Ayers, J. U. T.-K. Chiasson, B. O. Burress, and L. Marlino, *Evaluation of 2004 Toyota Prius Hybrid Electric Drive System*, May 2006. [Online]. Available: http://www.osti.gov/scitech/servlets/purl/890029

[39] J. Hsu, *Report on Toyota Prius Motor Thermal Management*, Feb 2005. [Online]. Available: http://www.osti.gov/scitech/servlets/purl/885987

[40] N. Bianchi, M. Pré, G. Grezzani, and S. Bolognani, "Design considerations on fractional-slot fault-tolerant synchronous motors," in *Electric Machines and Drives, 2005 IEEE International Conference on*, May 2005, pp. 902–909.

[41] J. Li, D.-W. Choi, D.-H. Son, and Y.-H. Cho, "Effects of mmf harmonics on rotor eddy-current losses for inner-rotor fractional slot axial flux permanent magnet synchronous machines," *Magnetics, IEEE Transactions on*, vol. 48, no. 2, pp. 839–842, Feb 2012.

[42] (2014, Okt) Arnold Magnetic Technologies. Accessed 2014-10-13. [Online]. Available: http://www.arnoldmagnetics.com/Neodymium_Literature.aspx

[43] (2014, Aug) Metalprices.com. Accessed 2014-08-05. [Online]. Available: http://www.metalprices.com/dailysnapshots/Index

[44] (2014, Aug) Metal-pages.com. Accessed 2014-08-05. [Online]. Available: http://www.metal-pages.com/

[45] (2011, Dec) Critical materials strategy. U.S. Department of energy. Accessed 2014-08-05. [Online]. Available: http://www.arnoldmagnetics.com/Rare_Earth_Information.aspx

[46] (2012, jan) The important role of dysprosium in modern permanent magnets. Arnold Magnetic Technologies. Accessed 2014-08-05. [Online]. Available: http://www.arnoldmagnetics.com/Rare_Earth_Information.aspx

[47] J. Hsu, *Report on Toyota/Prius Motor Design and Manufacturing Assessment*, Jul 2004. [Online]. Available: http://www.osti.gov/scitech/servlets/purl/885676

[48] K. Kiyota, H. Sugimoto, and A. Chiba, "Comparing electric motors: An analysis using four standard driving schedules," *Industry Applications Magazine, IEEE*, vol. 20, no. 4, pp. 12–20, July 2014.

[49] (2015, September) Atmel Corporation. Accessed 2016-02-05. [Online]. Available: http://www.atmel.com/images/atmel-8151-8-bit-avr-atmega128a_datasheet.pdf

[50] (2008, April) Maxim Integrated. Accessed 2016-02-05. [Online]. Available: https://datasheets.maximintegrated.com/en/ds/DS18B20.pdf

[51] (2015, July) Analog Devices. Accessed 2016-02-05. [Online]. Available: http://www.analog.com/media/en/technical-documentation/data-sheets/ADUM1250_1251.pdf

[52] (2009, May) Analog Devices. Accessed 2016-02-05. [Online]. Available: http://www.analog.com/media/en/technical-documentation/data-sheets/AD8236.pdf

[53] Vishay Semiconductors. Accessed 2016-02-29. [Online]. Available: http://www.vishay.com/docs/82497/tsop753w.pdf

[54] LogView. Accessed 2016-02-05. [Online]. Available: http://www.logview.info

[55] T. M. Jahns, "Flux-weakening regime operation of an interior permanent-magnet synchronous motor drive," *IEEE Transactions on Industry Applications*, vol. IA-23, no. 4, pp. 681–689, July 1987.

[56] B. C. Mecrow, A. G. Jack, J. A. Haylock, and J. Coles, "Fault-tolerant permanent magnet machine drives," *IEE Proceedings - Electric Power Applications*, vol. 143, no. 6, pp. 437–442, Nov 1996.